

TECHNICAL UNIVERSITY of MADRID (UPM)
School of Naval Architecture and Ocean Engineering (ETSIN)



**Hydrodynamic forces on heave plates for offshore
systems oscillating close to the seabed or the free
surface**

Author:

Carlos A. GARRIDO-MENDOZA
MENG. AEROSPACE ENGINEER

Director:

Antonio SOUTO-IGLESIAS
Professor. DMFPA, ETSIN, UPM

Codirector:

Krish THIAGARAJAN
Alston D and Ada Lee Correll
Presidential Chair in Energy.
Professor. University of Maine

This dissertation is submitted for the degree of

Doctor of Philosophy
Maritime Technology

April 2015

I would like to dedicate this thesis to my loving parents...

Declaration

I hereby declare that except where specific reference is made to the work of others, the contents of this dissertation are original and have not been submitted in whole or in part for consideration for any other degree or qualification in this, or any other University. This dissertation is the result of my own work and includes nothing which is the outcome of work done in collaboration, except where specifically indicated in the text.

Carlos A. GARRIDO-MENDOZA

April 2015

Acknowledgements

I would like to acknowledge Prof. Antonio Souto-Iglesias for giving me quality supervision and his full support throughout the years. I thank him for the concern he has shown for my academic progress at the Technical University of Madrid, and his encouragement of my future research development.

I want to thank Mr. Carlos López-Pavón for providing me with the industrial motivation for my thesis, for giving me access to a substantial amount of experimental data, and for bright ideas on porosity and flaps topics.

I would also like to thank Prof. Krish Thiagarajan of Mechanical Engineering Department at the University of Maine for his valuable advice and helpful discussions.

I want to thank Prof. Andrea Colagrossi and Mr. Benjamin Bouscasse for their help with the mathematical formulation and their valuable advices.

I thank to Prof. Jesús Gómez-Góñi for helping with the PhD grant.

I would like to thank to Mr. Elkin Botia-Vera for his help during the experimental campaigns.

I also thank to Mr. José Luis Cercós for his help in many aspects of computational fluid dynamics.

I thank to CEHIPAR Ocean Basin staff led by Mr. Adolfo Marón, for conducting some of the experiments within the framework of the different projects.

I also want to thank Prof. Longbin Tao of the School of Marine Science and Technology at the Newcastle University for hosting me during a research leave in 2014.

I would like to thank Mr. José Ignacio Cardesa for his ideas regarding grid turbulence that led us to the idea of the fractal plate.

I thank all the staff members at the CEHINAV group for their help in different topics.

I acknowledge the funds received from UPM PhD grant program and UPM mobility grants.

Abstract

Offshore wind energy is one of the promising resources which can reduce the fossil fuel energy consumption and cover worldwide energy demands. Offshore wind turbine concepts are based on either a fixed structure as a jacket or a floating offshore platform like a semisubmersible, spar or tension leg platform. Floating offshore wind turbines have the potential to be an important part of the energy production profile in the coming years. In order to accomplish this wind integration, these wind turbines need to be made more reliable and cost efficient to be competitive with other sources of energy.

Floating offshore artifacts, such oil rigs and wind turbines, may experience resonant heave motions in sea states with long peak periods. These heave resonances may increase the system downtime and cause damage on the system components and as well as on risers and mooring systems. The heave resonant response may be reduced by different means: (1) increasing the damping of the system, (2) keeping the natural heave period outside the range of the wave energy, and (3) reducing the heave excitation forces. A typical example to accomplish this reduction are “Heave Plates”. Heave plates are used in the offshore industry due to their hydrodynamic characteristics, i.e., increased added mass and damping.

Conventional offshore hydrodynamic analysis considers a structure in waves, and evaluates the linear and nonlinear loads using potential theory. Viscous damping, which is expected to play a crucial role in the resonant response, is an empirical input to the analysis, and is not explicitly calculated. The present research has been mainly focused on the prediction of viscous damping and added mass of floating offshore wind turbine heave plates. In the calculations, the hydrodynamic forces have been measured in order to compute how the hydrodynamic coefficients of added mass¹ and damping vary with the KC ² number, which characterises the amplitude of heave motion relative to the diameter of the disc. In addition,

¹Added mass is the inertia added to a system because an accelerating or decelerating body must move (or deflect) some volume of surrounding fluid as it moves through.

²Keulegan-Carpenter number (KC) is a dimensionless quantity that characterises the amplitude of heave motion relative to the diameter of the disc.

the influence on the hydrodynamic coefficients when the heave plate is oscillating close to the free surface or the seabed has been investigated. In this process, a new model describing the work done by damping in terms of the flow enstrophy, is described herein. This new approach is able to provide a direct correlation between the local vortex shedding processes and the global damping force. The analysis also includes the study of different edges geometry, and examines the sensitivity of the damping and added mass coefficients to the porosity of the plate.

A novel porous heave plate based on fractal theory has also been proposed, tested experimentally and compared with experimental data obtained by other authors for plates with similar porosity.

A numerical solver of Navier Stokes equations, based on the finite volume technique has been applied. It uses the open-source libraries of OpenFOAM (Open source Field Operation And Manipulation), to solve 2 incompressible, isothermal immiscible fluids using a *VOF* (volume of fluid) phase-fraction based interface capturing approach, with optional mesh motion and mesh topology changes including adaptive re-meshing. Numerical results have been compared with experiments conducted at Technical University of Madrid (CEHINAV) and CEHIPAR model basins in Madrid and with others performed at School of Mechanical Engineering in The University of Western Australia ^{3 4}. A brief summary of main results are presented below:

1. At low KC numbers, a systematic increase in added mass and damping, corresponding to an increase in the seabed proximity, is observed. Specifically, for the cases when the heave plate is oscillating closer to the free surface, the dependence of the hydrodynamic coefficients is strongly influenced by the free surface.
2. As seen in experiments, a critical KC , where the linear trend of the hydrodynamic coefficients with KC is disrupted and that depends on the seabed or free surface distance, has been found.
3. The physical behavior of the flow around the critical KC has been explained through an analysis of the flow vorticity field.

³Wadhwa and Thiagarajan (2009). Wadhwa, H. and Thiagarajan, K. P. Experimental Assessment of Hydrodynamic Coefficients of Disks Oscillating Near a Free Surface. ASME 28th International Conference on Offshore Mechanics and Arctic Engineering, OMAE, 2009.

⁴Wadhwa et al. (2010). Wadhwa, H. and Krishnamoorthy, B. and Thiagarajan, K. P. Variation of Heave Added Mass and Damping Near Seabed. ASME 29th International Conference on Offshore Mechanics and Arctic Engineering, OMAE, 2010.

-
4. The porosity of the heave plates reduces the added mass for the studied porosity at all KC numbers, but the porous heave plates are found to increase the damping coefficient with increasing amplitude of oscillation, achieving a maximum damping coefficient for the heave plate with 10% porosity in the entire KC range.
 5. Another concept taken into account in this work has been the heave plates with flaps. Numerical and experimental results show that using discs with flaps will increase added mass when compared to the plain plate but may also significantly reduce damping.
 6. A novel heave plate design based on fractal theory has tested experimentally for different submergences and compared with experimental data obtained by other authors for porous plates. Results show an unclear behavior in the coefficients and should be studied further.

Future work is necessary in order to address a series of open questions focusing on 3D effects, optimization of the heave plates shapes, etc.

Resumen

La energía eólica marina es uno de los recursos energéticos con mayor proyección pudiendo contribuir a reducir el consumo de combustibles fósiles y a cubrir la demanda de energía en todo el mundo. El concepto de aerogenerador marino está basado en estructuras fijas como jackets o en plataformas flotantes, ya sea una semisumergible o una TLP. Se espera que la energía eólica offshore juegue un papel importante en el perfil de producción energética de los próximos años; por tanto, las turbinas eólicas deben hacerse más fiables y rentables para ser competitivas frente a otras fuentes de energía.

Las estructuras flotantes pueden experimentar movimientos resonantes en estados de la mar con largos períodos de oleaje. Estos movimientos disminuyen su operatividad y pueden causar daños en los componentes eléctricos de las turbinas y en las palas, también en los risers y moorings. La respuesta de la componente vertical del movimiento puede reducirse mediante diferentes actuaciones: (1) aumentando la amortiguación del sistema, (2) manteniendo el período del movimiento vertical fuera del rango de la energía de la ola, y (3) reduciendo las fuerzas de excitación verticales. Un ejemplo típico para llevar a cabo esta reducción son las "Heave Plates". Las heave plates son placas que se utilizan en la industria offshore debido a sus características hidrodinámicas, ya que aumentan la masa añadida y la amortiguación del sistema.

En un análisis hidrodinámico convencional, se considera una estructura sometida a un oleaje con determinadas características y se evalúan las cargas lineales usando la teoría potencial. El amortiguamiento viscoso, que juega un papel crucial en la respuesta en resonancia del sistema, es un dato de entrada para el análisis. La tesis se centra principalmente en la predicción del amortiguamiento viscoso y de la masa añadida de las heave plates usadas en las turbinas eólicas flotantes. En los cálculos, las fuerzas hidrodinámicas se han obtenido con el fin de estudiar cómo los coeficientes hidrodinámicos de masa añadida⁵ y

⁵Término utilizado para expresar la fuerza de inercia que ejerce el fluido sobre un sólido, debida a la aceleración del mismo sólido.

amortiguamiento varían con el número de KC ⁶, que caracteriza la amplitud del movimiento respecto al diámetro del disco. Por otra parte, se ha investigado la influencia de la distancia media de la ‘heave plate’ a la superficie libre o al fondo del mar, sobre los coeficientes hidrodinámicos. En este proceso, un nuevo modelo que describe el trabajo realizado por la amortiguación en función de la enstrofia, es descrito en el presente documento. Este nuevo enfoque es capaz de proporcionar una correlación directa entre el desprendimiento local de vorticidad y la fuerza de amortiguación global. El análisis también incluye el estudio de los efectos de la geometría de la heave plate, y examina la sensibilidad de los coeficientes hidrodinámicos al incluir porosidad en ésta.

Un diseño novedoso de una heave plate, basado en la teoría fractal, también fue analizado experimentalmente y comparado con datos experimentales obtenidos por otros autores.

Para la resolución de las ecuaciones de Navier Stokes se ha usado un solver basado en el método de volúmenes finitos. El solver usa las librerías de OpenFOAM (Open source Field Operation And Manipulation), para resolver un problema multifásico e incompresible, usando la técnica *VOF* (volume of fluid) que permite capturar el movimiento de la superficie libre. Los resultados numéricos han sido comparados con resultados experimentales llevados a cabo en el Canal del Ensayos Hidrodinámicos (CEHINAV) de la Universidad Politécnica de Madrid y en el Canal de Experiencias Hidrodinámicas (CEHIPAR) en Madrid, al igual que con otros experimentos realizados en la Escuela de Ingeniería Mecánica de la Universidad de Western Australia^{7 8}. Los principales resultados se presentan a continuación:

1. Para pequeños valores de KC , los coeficientes hidrodinámicos de masa añadida y amortiguamiento incrementan su valor a medida que el disco se aproxima al fondo marino. Para los casos cuando el disco oscila cerca de la superficie libre, la dependencia de los coeficientes hidrodinámicos es más fuerte por la influencia del movimiento de la superficie libre.
2. Los casos analizados muestran la existencia de un valor crítico de KC , donde la tendencia de los coeficientes hidrodinámicos se ve alterada. Dicho valor crítico depende

⁶Keulegan-Carpenter (KC), número adimensional que caracteriza la amplitud del movimiento en heave, relativo al diámetro del disco.

⁷Wadhwa and Thiagarajan (2009). Wadhwa, H. and Thiagarajan, K. P. Experimental Assessment of Hydrodynamic Coefficients of Disks Oscillating Near a Free Surface. ASME 28th International Conference on Offshore Mechanics and Arctic Engineering, OMAE, 2009.

⁸Wadhwa et al. (2010). Wadhwa, H. and Krishnamoorthy, B. and Thiagarajan, K. P. Variation of Heave Added Mass and Damping Near Seabed. ASME 29th International Conference on Offshore Mechanics and Arctic Engineering, OMAE, 2010.

de la distancia al fondo marino o a la superficie libre.

3. El comportamiento físico del flujo, para valores de KC cercanos a su valor crítico ha sido estudiado mediante el análisis del campo de vorticidad.
4. Introducir porosidad al disco, reduce la masa añadida para los valores de KC estudiados, pero se ha encontrado que la porosidad incrementa el valor del coeficiente de amortiguamiento cuando se incrementa la amplitud del movimiento, logrando un máximo de damping para un disco con 10% de porosidad.
5. Los resultados numéricos y experimentales para los discos con faldón, muestran que usar este tipo de geometrías incrementa la masa añadida cuando se compara con el disco sólido, pero reduce considerablemente el coeficiente de amortiguamiento.
6. Un diseño novedoso de heave plate basado en la teoría fractal ha sido experimentalmente estudiado a diferentes calados y comparado con datos experimentales obtenidos por otros autores. Los resultados muestran un comportamiento incierto de los coeficientes y por tanto este diseño debería ser estudiado más a fondo.

Table of contents

Declaration of Authorship	v
Acknowledgements	vii
Abstract	ix
Resumen	xiii
Table of contents	xvii
Nomenclature	xxii
1 Introduction	1
1.1 Motivation	1
1.2 Renewable energy sector in Spain	2
1.3 Overview of offshore wind technology	4
1.3.1 Introduction	4
1.3.2 Offshore wind technology in Spain	6
1.3.3 Wind turbine size and development	8
1.3.4 Classification of offshore wind turbines	9
1.4 Damping of heave motion	16
1.5 Heave plates	19
1.5.1 Experimental work	19
1.5.2 Modelling	20
2 Objectives	23
2.1 Objectives of the study	23
3 Methodology	25
3.1 Methodology of the study	25

Table of contents

4	Physical and numerical modelling	27
4.1	Introduction	27
4.2	Review	27
4.3	Theoretical formulation	30
4.3.1	Governing equations	30
4.3.2	Mechanical energy	31
4.3.3	Dissipation	33
4.4	Physical model	35
4.4.1	Numerical solution	35
4.4.2	Modelling of FOWT	37
4.4.3	Hydrodynamic Force	38
4.4.4	Numerical tests	38
4.4.5	Experimental tests	39
4.4.6	Numerical model of turbulence	41
4.4.7	Computational tool	42
4.4.8	Validation of numerical procedure	43
5	Parametric dependence of hydrodynamic coefficients of a heave plate oscillating near a seabed or a free surface	47
5.1	Heave plate moving near a seabed	47
5.1.1	Introduction	47
5.1.2	Case study description	48
5.1.3	Mesh generation	50
5.1.4	Convergence analysis	51
5.1.5	Results	56
5.2	Heave plate oscillating close to a free surface	73
5.2.1	Introduction	73
5.2.2	Case study description	73
5.2.3	Mesh generation	73
5.2.4	Results	75
5.3	Analogies Seabed - Free surface	91
6	Hydrodynamic coefficients of an oscillating semi-submersible column with a heave plate	93
6.1	General	93
6.2	Case study description	93
6.2.1	Experimental investigation	93

6.2.2	CFD calculations.	100
6.3	Results	112
6.3.1	General	112
6.3.2	Solid heave plate: influence of flow parameters KC , β and submergence of the heave plate s/r_d	113
6.3.3	Sensitivity study of scale effects	118
6.3.4	Influence of the shape of the heave plate: flaps	119
6.3.5	Influence of the heave plate porosity	125
6.3.6	Fractal plate	129
7	Conclusions	135
7.1	Conclusions	135
7.2	Future work	137
8	Thesis Publications	139
8.1	Refereed papers	139
8.2	Conference papers	139
	References	141
	List of appendices	150
A	Energy Eqn. with control Volume.	153
B	Decomposition of the dissipation term.	157
B.1	Enstrophy integral	159
B.2	Free surface dissipation integral	161
C	Useful Relations.	165
D	Pressure-Velocity Coupling Algorithm.	167
E	Volume of Fluid Method.	171
F	Fractal Plate Characteristics.	173

Nomenclature

Greek Symbols

β	Frequency parameter. Eqn. (4.30)	
μ	Dynamic viscosity of the fluid	$[Pa \cdot s]$
ν	Kinematic viscosity of the fluid	$[m^2/s]$
ρ	Density of the fluid	$[kg/m^3]$
ω	Motion angular frequency	$[rad/s]$

Acronyms / Abbreviations

A	Motion heave amplitude	$[m]$
A_{33}	Heave added mass	$[kg]$
S_w	Waterplane area	
B_{33}	Heave viscous damping	$[kg/s]$
C_a	Added mass coefficient	
C_b	Damping coefficient	
C_d	Drag coefficient	
D_c	Column diameter	$[m]$
D_d	Disc diameter	$[m]$
DNS	Direct Numerical Simulation	
DVM	Discrete Vortex Methods	

f	Motion frequency	[Hz]
$\mathbf{F}_{fluid/body}(t)$	Time history of the force that the fluid exerts on the body	
$FLOWT$	Floating Offshore Wind Turbines	
FVM	Finite Volume Method	
h	Elevation of the disc from the seabed	[m]
\mathbf{k}	Unitary vector in the z direction, pointing upwards	
K_{33}	Hydrostatic restoring coefficient	
KC	Keulegan-Carpenter number. Eqn. (4.29)	
NS	Navier-Stokes	
PIV	Particle Image Velocimetry	
Re	Reynolds number, Eqn. (4.31)	
s	Submergence of the disc from the free surface	[s]
T	Motion period	[s]
T_{33}	Heave period for a semi-submersible, Eqn. (4.32)	[s]
TLP	Tension Leg Platform	
VOF	Volume of Fluid	
z	Heave displacement	
\ddot{z}	Second order time derivative of the motion	
\dot{z}	First order time derivative of the motion	

Chapter 1

Introduction

1.1 Motivation

Offshore technology has experienced a remarkable growth since the 1940s, when offshore drilling platforms were first used in the Gulf of Mexico. At the present time, a wide variety of offshore structures are being used, even under severe environmental conditions. These are predominantly related to oil and gas recovery, but they are also used in other applications such as harbor engineering, ocean energy extraction and more recently in floating wind turbines.

Difficulties in design and construction are considerable, particularly as structures are being located at ever-increasing depths and are subjected to extremely hostile environmental conditions. New technologies and structures have to be developed to reduce the economic and ecologic risks. For hostile areas the reduction of harsh weather induced downtime and increased safety have become economic factors of increasing importance. Expensive and time consuming trial and error parameter studies are necessary to end up with a good design.

Deep water offshore structures have been considered as the most reliable and cost effective system for offshore oil and gas exploration. However, these structures are susceptible to resonant behaviour in sea states with long swell condition having peak period lying in the range of 23 to 25 seconds and these natural periods are smaller for smaller artifacts such as floating wind turbines. An efficient way to reduce the amplitude of responses is to shift the heave natural period of the proposed structure outside the range of wave spectrum. Damping elements have been used in ships and offshore structures as response reduction devices for maintaining the hydrodynamic response within acceptable limits. The use of such elements has been mainly based on past experience or using empirical based design approach.

Due to the continued growth of the world population and to the more than ever energy demand, renewable energy plays an important role in the development of society, resulting

in significant energy security, climate change mitigation, and economic benefits. Renewable energy resources exist over wide geographical areas, in contrast to other energy sources, which are concentrated in a limited number of countries. A well known renewable energy source is the wind and traditional wind generators have been installed inland for many years. Wind turbines have also been successfully installed at relatively shallow water depths. This has typically been done by piled cylinders or gravity based foundations. Offshore wind turbines are one of the most promising technologies to provide an adequate response to our current energy demand. Based mainly on technology from the oil and gas industry, there are currently different support structure concepts in the market, which intend to achieve a satisfactory outcome to the changeable operational conditions and to help making wind energy more cost effective.

The vision for large-scale floating offshore wind turbines (FOWT) was introduced by Professor William E. Heronemus at the University of Massachusetts in 1972 (Heronemus, 1972), but it was not until the mid 1990's, after the commercial wind industry was well established, that the topic was taken up again by the mainstream research community. Current fixed-bottom technology has seen limited deployment to water depths of nearly 30 m (shallow waters) (Musial et al., 2004), but the continental shelf is narrow in many countries which means that the offshore wind energy sector must focus, in such countries, on the floating structures foundations.

1.2 Renewable energy sector in Spain

Spanish renewable energy potential is wide, and well above the domestic energy demand. It could even be said that renewable energies are Spain's main energy asset. Expressed in terms of installable electrical power, Spain has the potential for several terawatts (TW) of solar energy. Wind power takes second place, with a potential estimated at approximately 340 GW. The country's hydroelectric potential, estimated at approximately 33 GW, is also very high, but the greater part of this potential has already been developed. The remaining technologies have a potential near 50 GW with the potential for wave and geothermal energy being approximately 20 GW each (IDAE, 2011).

Renewable energy sector in Spain represented 42.8% of total energy production in 2014 (42.2% in 2013). Overall 27.4% of Spain's electricity was generated from wind and solar in 2014 (REE, 2014). In absolute terms, renewable generation fell by 1.0% regarding the previous year, mainly due to the 6.1% drop in wind production. Despite this decline, it should be noted that wind power was the technology that made the largest contribution towards the total energy production in the Iberian Peninsula electricity system with more

than 20%, more than nuclear and any other energy resource. This is really a remarkable milestone, which should be highlighted. However, Spain is experiencing a negative trend in the fulfilment of the 2020 renewable energy objectives. Recent reports have shown that the best-case scenario projection is within the range of 12.6 – 17.1%, far from the forecasted goal of 20%. The projection also represents a clear breach of the objectives in the National Action Plan for Renewable Energy (Spanish initials PANER) (PANER, 2010), which gives a goal of 22.7%, and the plan drawn up by the Spanish government through the Plan for Renewable Energies (PER), which forecasts 20.8% over 2011 – 2020 (IDAE, 2011).

In addition, the situation for renewable energy and especially for wind energy has become extremely difficult in Spain during the period in which this PhD was carried out, from early 2011 till 2015. In early 2011, a feed-in-tariff was in place and substantial *R&D* efforts funded by the government and by private companies (IBERDROLA, ACCIONA, ABENGOA, etc) were ongoing, such as CENIT project AZIMUT, within which part of the experimental activities of this PhD work were funded. However, on July 12, 2013, the Spanish Government approved measures to overhaul electricity sector regulations and composed a set of new rules (Real decreto ley 1/2012, 2012). This regulation removed economic incentives for new production of electricity from cogeneration, renewable energy and waste. It also removed incentives for constructing these facilities, in order to avoid adding new costs to the electrical system. As a consequence, the Spanish renewable energy market has fallen down drastically and wind energy industry, in which Spain was one of the worldwide leading countries, with very promising forecast, has now also broken down into extreme crisis (IREC, 2014). The uncertainty of premiums in Spain means that no one will invest in Spain's renewable energy market, and the share prices of the corporations most affected by the suppression of feed-in tariff for new installations have been Iberdrola, EDP Renewables and Acciona. Fortunately Europe is still supporting wind energy and its research with the tendency moving towards offshore.

The road to the Spanish offshore wind energy began in 2007 when the Ministry of Industry and Environment started to work to define areas suitable for the installation of windmills at sea, concluding that Spain with more than 4800 kilometers of coastline, had many opportunities in this field. However, the current technology limited to a few locations the placement of offshore wind farms. As the technology has advanced into deeper water, floating wind turbine platforms may be the most economical means for deploying offshore wind turbines at some sites. Technically, the long-term survivability of floating structures has already been successfully demonstrated by the marine and offshore oil industries over many decades. However, the economics that allowed the deployment of thousands of offshore oil rigs have yet to be demonstrated for floating wind turbine platforms. Due to the 2012 changes in the

regulatory framework, the prospects are not good, in any case, for the development, at the moment, of the floating offshore wind turbines in Spain.

1.3 Overview of offshore wind technology

1.3.1 Introduction

According to [Intergovernmental Panel on Climate Change \(2012\)](#) (IPCC) report, 80% of the world's energy supply could come from renewable sources by 2050 and wind energy will play a major role in electricity generation in 2050. In the growing market for wind energy and due to the limited available onshore locations, the development of offshore wind farms becomes more and more important. With a rapid development of technology, the offshore wind power projects have become a trend in many countries. Without doubt, offshore wind will lead technology advances in the wind sector in a near future as it seeks to exploit resources further offshore.

More than 35 GW of new wind power capacity was brought online in 2013, but this was a sharp decline in comparison to 2012, when global installations were in excess of 45 GW. The new global total at the end of 2013 was 318.105 GW, representing cumulative market growth of more than 12.5 percent (see Fig. 1.1). For the sixth year in a row, Asia was the world's largest regional market for wind energy, with capacity additions totaling just over 18.2 GW. In terms of annual installations China regained its leadership position, adding 16.1 GW of new capacity in 2013, a significant gain over 2012 when it installed 12.96 GW of new capacity ([Global Wind Energy Council, 2013](#)).

Since the first offshore wind farm built in Denmark (Vindeby 5 MW in 1991), offshore wind energy development in Europe has experienced three stages: initial research stage in 1980 – 1990; an experimental testing stage in 1991 – 2000; and commercialization stage since 2001. Today, more than 7 GW of offshore wind power has been installed globally, representing about 2% of total installed wind power capacity. Most of them, 90%, reside in 74 wind farms spread over 11 European countries, in which the United Kingdom (UK), Belgium and Germany are the top countries in offshore installed capacity (see Table 1.1 and Fig. 1.2). 78.8% of substructures are monopiles, 10.4% are gravity based foundations, jackets account for 4.7%, tripods account for 4.1% and tripiles account for 1.9%. There are also two full scale grid connected floating turbines, and two down-scaled prototypes ([EWEA, 2015](#)). According to the more ambitious projections, a total of 80 GW could be installed by 2020 worldwide, with three quarters of this in Europe.

Thus, if the strong expansion of offshore wind farms continues, it is expected that 40 GW

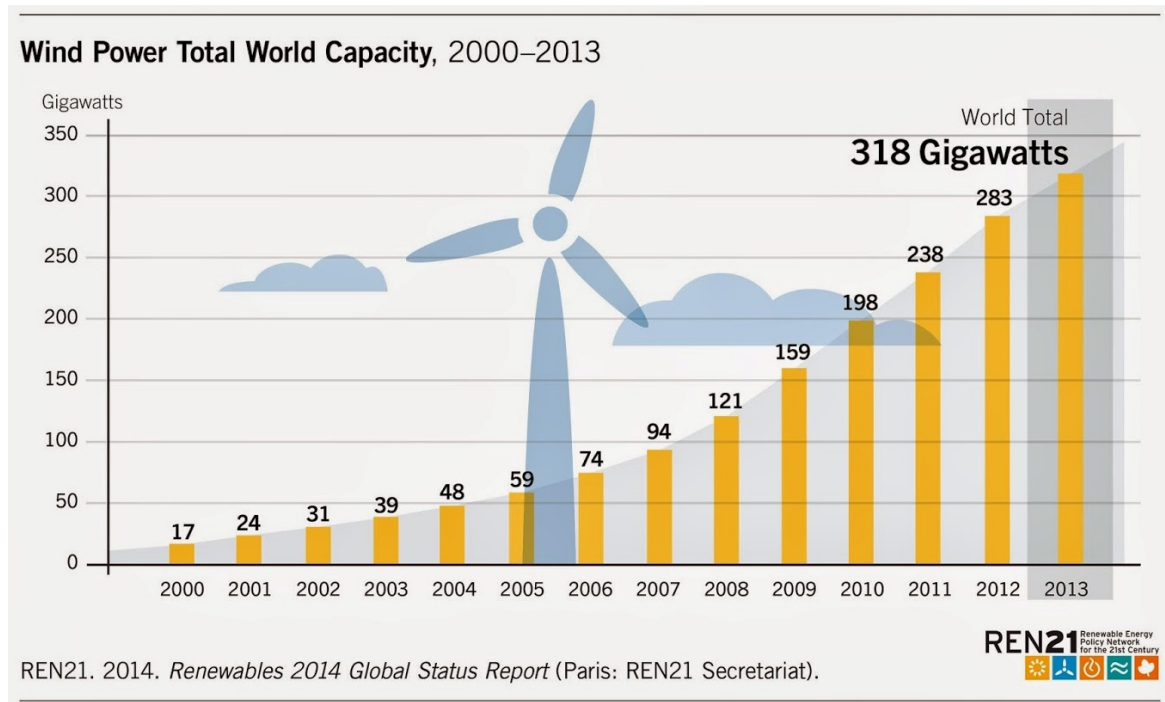


Fig. 1.1 Global cumulative installed wind capacity 2000 – 2013. Source: REN21, 2014

Table 1.1 The latest largest operational offshore wind farms in the world. Source:

Wind farm	Capacity (MW)	Country	Number of turbines	Commissioned
London Array	630	UK	175	2012
Greater Gabbard	504	UK	140	2012
Anholt	400	Denmark	111	2013
BARD Offshore 1	400	Germany	80	2013
West Duddon Sands	389	UK	102	2014
Walney	367	UK	102	2012
Thorntonbank	325	Belgium	54	2013
Sheringham Shoal	315	UK	88	2012
Thanet	300	UK	100	2010
DanTysk	288	Germany	80	2014
Meerwind Süd / Ost	288	Germany	80	2014
Lincs	270	UK	75	2013
Northwind	216	Belgium	72	2014

of offshore wind farms will be integrated into the grid and provide between 148 TWh of electricity to Europe by 2020 which can meet 10% of Europe's electricity demand. This figure could be boosted to 17% in 2030, according to the European Wind Energy Association (EWEA, 2015). Some European countries such as Germany and the UK, with ambitious

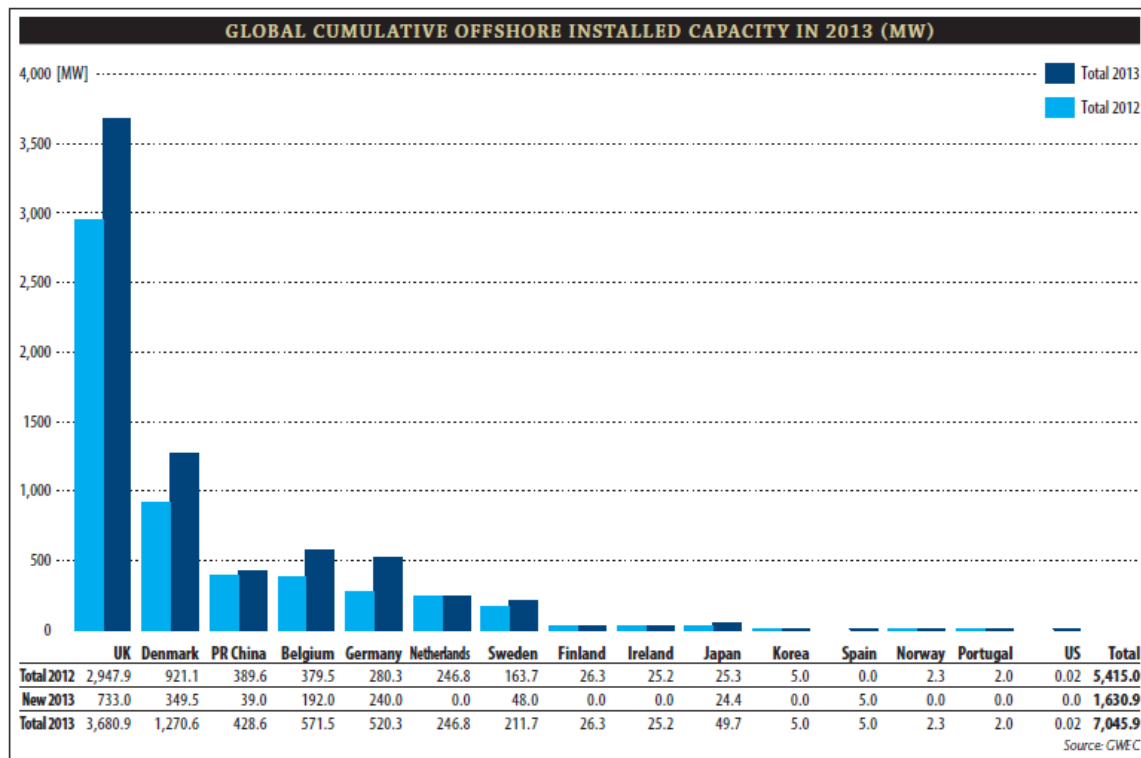


Fig. 1.2 Global cumulative offshore installed capacity in 2013. Source: GWEC, 2013

offshore wind plans, have already become the world's leading offshore wind market.

The new projects that were being carried out are for deeper water depths and the cost of the support structure and foundation will be proportionally higher than for turbines in shallow waters. This means that finding an economically feasible design is vital for overall project viability. Recently, in Portugal a 2 MW prototype offshore wind turbine was installed in the north of the country placed on the floating device WindFloat developed by Principle Power (see Fig. 1.3). In the next phase an additional 5 MW turbine will follow. The project is undertaken by EDP Portugal and it expects to achieve a total capacity of 150 MW.

1.3.2 Offshore wind technology in Spain

Spain is endowed with significant wind power resources. According to estimates by the Institute for Energy Diversification and Saving (IDAE), published in the National Renewable Energy Plan for 2011 – 2020 (IDAE, 2011), the technical economical potential for onshore wind power is more than 100 GW by 2020, and more than 150 GW by 2030. The objective set for 2020 stands at 35 GW of installed wind capacity. For offshore wind power the current potential is estimated at 85 GW with a target of 750 MW by 2020. Up until 2010 the Span-

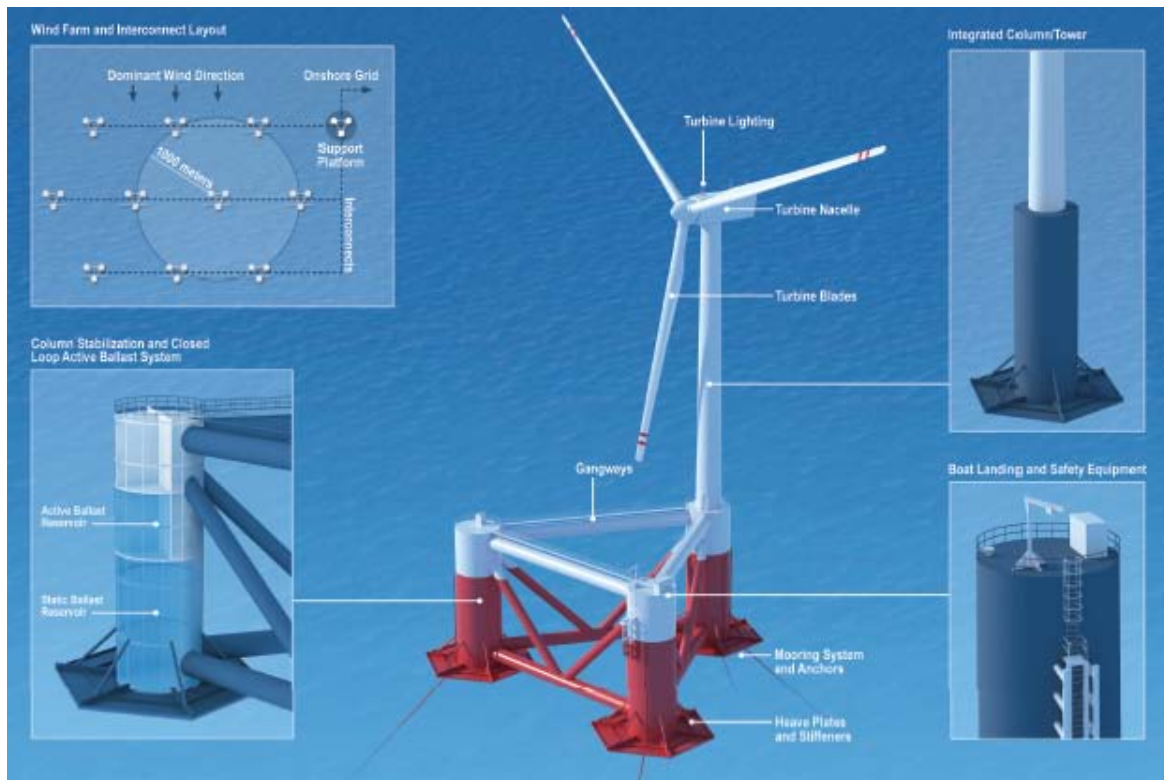


Fig. 1.3 The WindFloat design. Semisubmersible platform of three columns connected by trusses.
Source: Principle Power Inc.

ish wind energy market has seen tremendous growth, and the country led Europe in 2009 with 2.46 GW of new installations, taking total wind capacity up to 19.1 GW. This made wind power Spain's third-largest power generation technology behind combined cycle gas and nuclear power. Spain is home to some leading international wind power companies.

Spain has more than 4,800 kilometers of coastline presenting many opportunities in offshore wind energy field, but with technology available today, the bathymetric limit of the existing offshore wind farms in the world is less than 50 m, being about 60 % in bathymetric levels less than 20 m, depth at which the windmills can be installed in order to be economically viable (IDAE, 2011). This factor limited to a few locations the placement of offshore wind farms. The Spanish coastal continental shelf is characterized by its narrowness: only to four kilometers from the coast there are waters less than 50 meters deep. The road to the Spanish offshore wind energy began in 2007 when the Ministries of Industry and Environment started to work to define areas suitable for the installation of windmills at sea (Figs. 1.4 and 1.5).

In the Canary Islands is where more power could be installed, up to 20,000 MW. The downside is its very deep seabed. In the Gulf of Cadiz's the shelf extends several miles

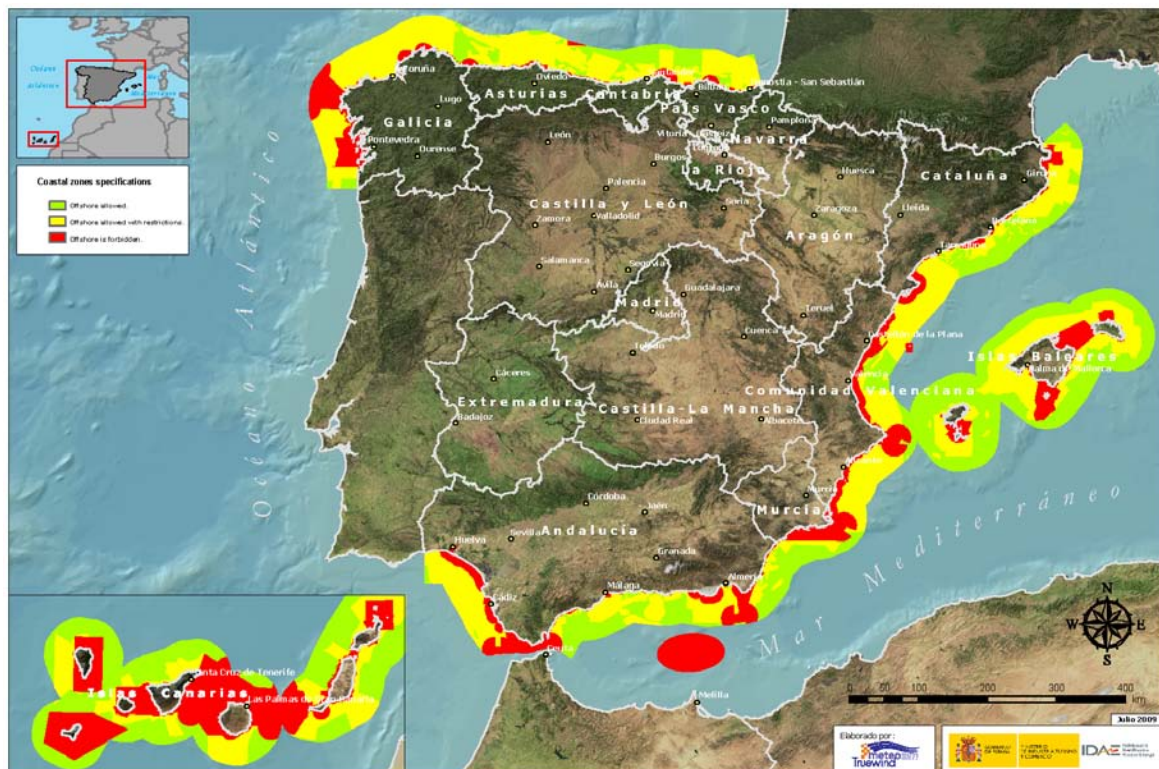


Fig. 1.4 Classification of coastal zones for the development of offshore wind projects; Source: Spanish Ministry for Environment, 2009.

from the coast at a depth around 50 meters. Even on the Galician coast, where the water depth is greater, the installation of smaller wind farms would be viable.

1.3.3 Wind turbine size and development

Wind turbine sizes have been changing dramatically over the past 40 years. Figure 1.6 (Herbert et al., 2007) from the US Department of Energy shows the increase in the size of the diameters of installed wind turbines. Figure 1.6 covers both inland and offshore wind turbines, and the trend toward large turbines is more pronounced for offshore turbines. This is due to the costs associated with constructing and installing the foundations or platforms for offshore turbines. In the early and mid 1980s, the typical wind turbine size was less than 100 kW. By the late 1980s and early 1990s, the turbine sizes had increased from 100 to 500 kW. Further, in the mid-1990s, the typical size ranged from 750 to 1000 kW. And by the late 1990s, the turbine size had gone up to 2.5 MW. Now turbines are available with capacities above 5 MW.

So, nowadays, the research is on a full swing to develop floating wind turbines of high power. for this reason, in recent years, the studies on the performances of the floating wind



Fig. 1.5 Wind map of Spain. Annual average speed at 80 m height; Source: Spanish Ministry for Environment, 2009.

turbine for various floater concepts have been carried out by various researchers in order to improve the energy production capacity of the system.

1.3.4 Classification of offshore wind turbines

1.3.4.1 General

Apart from a few experimental installation, all offshore wind turbines installed to date are on bottom-mounted substructures. Nearly all have been installed in waters shallower than 20 m and these structures are highly dependent on ocean floor conditions. In contrast, much of the vast offshore wind resource potential in the USA, China, Japan, Norway and many other countries, in particular Spain, is available in deeper water. At some water depth, floating support platforms will be the most economical type of support structure.

Recently, some offshore wind power projects are proposed in deeper water, where the winds are of higher velocities. For this reason, wind turbines on floating supports are the best solution to utilize the wind resources in those areas. To extend wind turbine systems to deeper water, practical research of offshore floating wind turbine systems is required. Also,

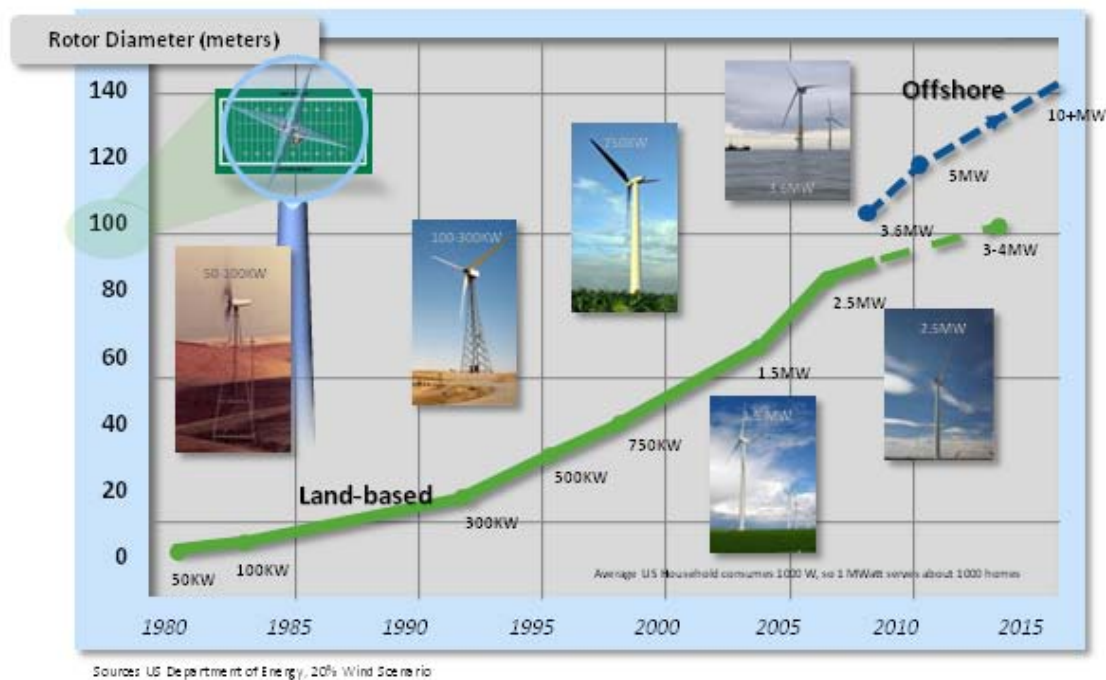


Fig. 1.6 Trends of the wind turbine sizes and capacity (US Dept. of Energy).

developing offshore floating wind farms is important because it can minimize the scenery disturbance, avoid the noise problems generated by wind-driven blades and make use of extremely abundant deep water wind resources.

As afore mentioned wind surrounding the globe has enormous potential to provide alternative source of energy in changing scenarios where global energy demands are increasing. Wind turbines can be placed offshore or onshore but, due to relatively low surface roughness of sea surface, offshore locations provide higher wind speed which places offshore wind turbine concept ahead of onshore wind turbine as per the volume of energy production is concerned. In the process of energy conversion, wind energy from offshore wind turbine can be converted to electrical power which can be used as power supply. Offshore wind turbines are classified into three major types depending upon the water depths such as, Fig. 1.7:

1. *Shallow water foundation (5-30 meter).*
2. *Transitional water foundation (30-60 meter).*
3. *Deep water wind turbine structure (more than 60 meter water depth).*

The shallow water wind turbines are generally placed in between 5m – 30m water depth and are in general classified as, (Figure 1.8):

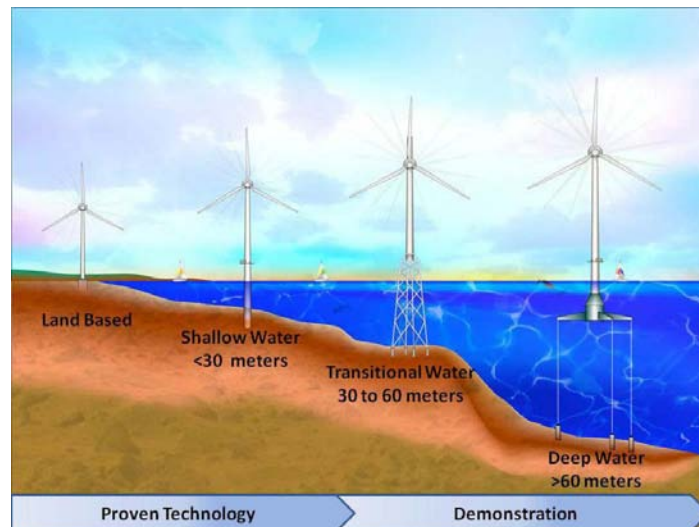


Fig. 1.7 Depth ranges for proposed and existing offshore wind turbine foundation designs. Source: NREL.

- Monopile structure.
- Gravity base structure.
- Suction bucket structure.

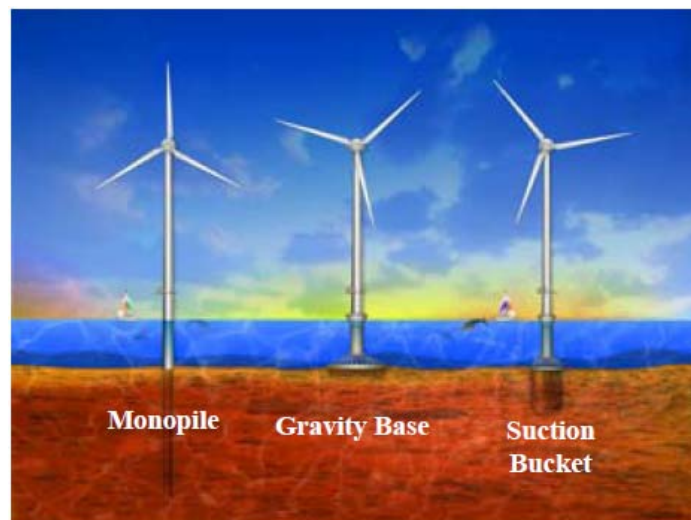


Fig. 1.8 Three shallow water wind turbine foundations; the monopile, the gravity base, and the suction bucket from right to left. Source: NREL.

The transitional offshore wind turbine are placed between 30m – 60m water depth and are classified as, Figure 1.9:

- Tripod tower.
- Guyed monopole.
- Full-height jacket.
- Submerged jacket with transition to tube tower.
- Enhanced suction bucket or gravity base.



Fig. 1.9 Transitional Substructure Technology. Source: NREL.

The deep water offshore wind turbines are generally floating structures and are placed in more than 60m water depth. They are the main focus of our research as heave plates are installed in these floating devices to damp heave motions.

1.3.4.2 Floating offshore wind turbines (FOWT)

Floating support structures have appeared in the offshore wind market as a consequence of the tendency within this industry to move into deeper waters. Since the first gravity base was installed, and afterwards monopiles, jackets or tripods, offshore wind parks have gone, step by step, into deeper and deeper waters. The main reason behind this transition lies on the better quality that wind presents at those locations.

Floating wind turbines have the potential to be placed anywhere in the ocean from 60 meters upwards to 900 m or beyond. This is a great benefit, because floating platforms allow offshore wind penetration into places where it may be prohibitive for fixed bottom offshore turbines. Floating platforms are also much less dependent on seabed conditions than fixed

bottom structures because they do not rely on the ocean floor for support, with mooring line anchors being a notable exception. Many of the floating platform designs are able to be towed by boats in order to be moved relatively easily. This may reduce costs associated with construction and maintenance. Countries like Japan, Norway or Spain present the majority of their offshore wind resource over deep waters. On the other hand, in some European countries, such as the United Kingdom, Germany, Denmark and the Netherlands, where shallow water sites appear to be abundant, the installation of wind parks at those water depth levels should still proliferate.

Floating offshore wind has been in the works for a while. Consortiums of companies, academic institutions and research organizations have developed different projects of offshore wind floating foundations. However, three main types of floating foundations for offshore wind turbine have been developed so far: Spar foundation, Semi-submersible foundation, and TLP (tension leg platform) foundation (see Fig. 1.10). Roddier et al. (2009) reviewed typical floating foundations of offshore wind turbines, such as Spars, TLP's and Semi-submersible/hybrid systems, and the pro-cons of these foundations, design basis and rules were listed in detail.

In 2008 Blue H Technologies operated the first floating wind turbine using a TLP with an 80 kW turbine installed 21 km off the southeast Italy coast in waters 113 metres deep. In September 2009, a 2.3 MW offshore wind turbine which was based on spar structure was installed in Norway to 10 km offshore into 220 metre-deep water (Nielsen et al., 2006) and in late 2012 a semi-submersible type one with 2.0 MW turbine was installed 5 km offshore of Aguçadoura, north of Porto in Portugal (Roddier et al., 2010).

The actual interest of the industry on floating offshore wind turbines is increasing since the last successful launch and test of real scale prototypes: Hywind in Norway (Hanson et al., 2011), Windfloat in Portugal (Roddier et al., 2010), Mitsui in Japan (Nicholls-Lee et al., 2014) and VoltornUS, the 1 : 8 large scale unit of University of Maine (Marsh, 2014; Viselli et al., 2014). A review on floating offshore wind technology may be found in LLC. (2012), where the status and challenges of this technology are summarized as follows:

- 61% of the US offshore wind resources are in water depths of more than 100 meters;
- Nearly all of Japan's offshore wind resources are in deep water;
- Various European locations such as off the coast of Norway and in the Mediterranean require floating foundation technology due to water depths;
- UK Round 3 contains some lease areas in water depths which may require floating technology.

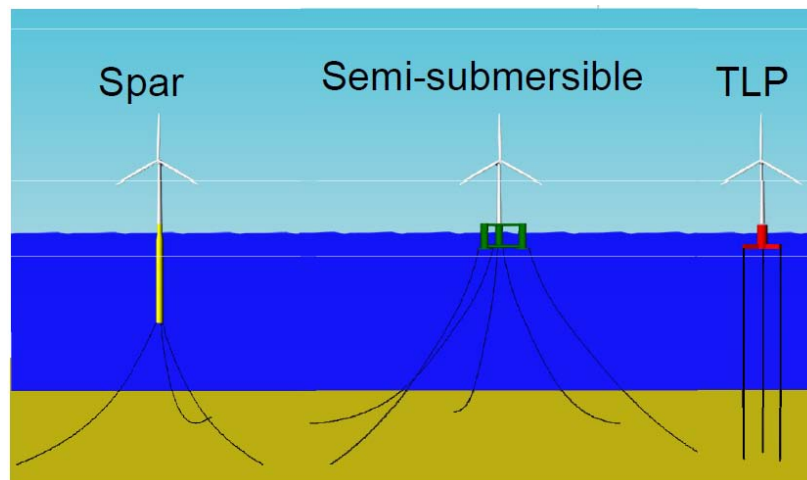


Fig. 1.10 Floating Offshore Wind Turbine Concepts. Source: Centre for Ships and Ocean Structures NTNU.

In general terms, the Spar-type has better heave performance than semi-submersibles due to their deep draft and reduced vertical wave exciting forces, but has larger pitch and roll motions, since the water plane area contribution to stability is reduced. TLPs have small heave and angular motions, but the complexity and cost of the mooring installation, the change in tendon tension due to tidal variations, and the structural frequency coupling between the mast and the mooring system, are three major hurdles for such systems. Semi-submersible concepts with a shallow draft and good stability in operational and transit conditions are significantly cheaper to tow out, install and commission than spar-buoy, due to their draft.

All these solutions have their origin in the oil & gas industry, but modifications and hybrids are beginning to emerge in their use for wind turbines.

1.3.4.2.1 Spar-type floating wind turbine. The spar buoy is typically a steel or concrete cylinder with low water plane area, ballasted with water and/or solid ballast which results in a weight-buoyancy stabilized structure with a large draft. The concept uses simple (few active components), well-proven technology with inherently stable design and few weaknesses. Based on the large draft, the spar may however require towing to the deep-water site in a horizontal position. In such cases the structure needs to be up-ended, stabilized and the turbine is then installed using a crane barge. A spar is generally moored using catenary or taut spread mooring systems. Statoil's Hywind is a 2.3 MW prototype that was deployed outside the west coast of Norway in 2009 was the first floating wind turbine structure installed and is still in operation (see Fig. 1.11).



Fig. 1.11 Spar-type floating wind turbine. Source: Statoil's Hywind project

1.3.4.2.2 Tension leg platform (TLP) type floating wind turbine. The TLP type comprises a floating platform structure to carry the wind turbine. In the offshore oil and gas industry, the conventional TLP platform comprises a square pontoon with columns on which the topside deck rests. A smaller version of this conventional hull form is the mini-TLP which has been adopted by the TLP-type floating wind turbine. Unlike the spar-type floating wind turbine which needs to be assembled in water, the TLP wind turbine may be assembled and commissioned onshore thereby avoiding the logistic difficulties of offshore assembly. The fully fitted up platform is towed to the deployment site thus precluding the need to charter and mobilize expensive heavy-lift vessels or derrick crane barge-types for offshore construction. TLPs have high buoyancy and are held back by tendon arms connected to the anchors. The pretensioned tethers provide the righting stability.

No TLP has yet been deployed as a large scale prototype, but there are some developments going on like the one led by IBERDROLA in whose experimental campaigns, the research group, which the author belongs to, has been involved (Fig. 1.12).

1.3.4.2.3 Semi-submersible type floating wind turbine. A semi-submersible is a free-surface stabilized structure with relatively small draft. It is a very adaptable structure thanks to its relatively low draft and high flexibility related to soil conditions. It is a heavy weighted structure with a considerable amount of steel and a relatively high manufacturing complexity



Fig. 1.12 TLP floating wind turbine. Source: Iberdrola-CEHINAV

due to the many welded connections. A semi-submersible structure is kept in position by the mooring lines, which typically are taut or catenary. This type of floating wind turbine may be constructed onshore. In 2011 the first large scale semi-sub prototype, Principle Power's WindFloat structure which consists of three column tubes with patented horizontal water entrapment heave plates at the bases, was installed outside Portugal (see Figure 1.13). The heave plates primarily serve to reduce heave and pitch motion without increasing floating platform size.

The main objective of this work is to model numerically the hydrodynamic performance of these heave plates.

1.4 Damping of heave motion

The context to which heave plates belong is that of oscillating structures under water, more specifically, those with a shape characterized by sharp edges. Application areas of these structures are numerous, such as damping plates in spar platforms (Nallayarasu and Bairathi, 2014; Sudhakar and Nallayarasu, 2011; Tao et al., 1999), heave plates for offshore wind turbine structures, bilge keels on ships and seabed templates (Molin, 2011), and heave plates added to the base of each column of a semisubmersible platform to enhance the stability of structure (Aubault et al., 2007).

In the case of floating spar platforms, resonant heave motions in sea states with long peak



Fig. 1.13 WindFloat semi-submersible type floating wind turbine. Source: Principle Power Inc.

periods may be experienced. Hydrodynamic damping then becomes a critical factor in keeping the response amplitude of the structures under acceptable limits. Usually, these offshore structures are lightly damped and therefore, although the magnitude of the exciting force may be small, the response of the system can be large. Haslum and Faltinsen (1999) proposed that the response might be reduced by 3 ways: (1) increasing the damping of the system, (2) keeping the natural heave period outside the range of the wave energy, and (3) further reducing the linear heave excitation forces.

Regarding technique number 1, a commonly used device to enhance the damping mechanisms in the vertical (heave) direction, is a heave plate, which is usually added at the base of the structure. This arrangement enhances the vortex shedding process due to isolated sharp edges, as well as increases the effective vertical mass of the structure, consequently changing the hydrodynamic properties of the body in question by introducing extra damping and increasing its natural period. In Fig. 1.14 the heave plate arrangement for WindFloat (Roddier et al., 2010) semi-submersible design is included (left). In the center, ACCIONA HYPERWIND Project design is included and an image of its column and heave plate is presented (right). Our research pays significantly attention to ACCIONA design because experimental data is available due to the involvement of the candidate in the experimental

and numerical analysis.



Fig. 1.14 Heave plate arrangement for WindFloat (Roddier et al., 2010) semi-submersible design (left). ACCIONA design (center) and one of its columns and heave plate (right).

Relative to technique 2, increasing the mass of the system is expensive and increasing added mass is also achieved with the use of heave plates. Reducing the water plane area is another option which is usually not viable due to structural reasons.

The technique 3, increasing the draft for slender designs reduces waves excitations. Nonetheless draft is subjected to other considerations like construction, transportation, etc.

It is well-known that flow properties get significantly altered in the presence of a close material boundary or a free surface. However, there are a few researchers that have focused their works on the influence on the hydrodynamic characteristics of a structure when moving close to the seabed or free surface. Lamb (1945, § 137) showed that a sphere constrained to move in a fluid along a line parallel to a wall experiences an “attraction” towards the wall. Greenhow and Lin (1983) and Faltinsen (1990, §Ch. 9) discussed flow phenomena associated with a cylinder entering and exiting a free surface. The re-alignment of the flow, due to boundary proximity, results in modified pressure and vorticity fields, in turn influencing the forces experienced by the body motion. In some offshore applications such as deployment of foundation templates and subsea structures, the penetration of a structure through the water surface and through the water column are important stages. An application mentioned in recommended practices, such as DNV-RP-H103 (2010), but not researched extensively, is the retrieval of installed equipment. Notwithstanding pull-out forces, that are felt during contact with the seabed, it is possible that the structure may vibrate after severing from the foundation but within proximity of the seabed. In such cases, hydrodynamic properties are modified, thus emphasizing the importance of having an accurate knowledge of hydrody-

dynamic loads in these conditions (Morrison and Cermelli, 2003).

Also within this context, the footings of jack-up wind turbine installation vessels may experience, when close to seabed during their touchdown, significant variations in damping and added mass, influencing in turn the dynamics of the whole vessel. Designers of such systems have to specify limiting environmental installation conditions, which requires modelling the motions of a jack-up platform with footings close to the seabed and predicting the resulting impact loads when the footings eventually hit the ground (Wind Jack MARIN JIP looks at these matters).

1.5 Heave plates

1.5.1 Experimental work

The underwater hydrodynamic performance of oscillating structures incorporating discs of various characteristics has been studied in past research. The hydrodynamic forces represented by suitably non-dimensionalized (added mass and damping) coefficients are normally found to be functions of the Keulegan-Carpenter (KC) number and the frequency parameter (β). Forced oscillation experiments on cylinders and discs (Thiagarajan and Troesch, 1998) show that the added mass and damping coefficients are linearly dependent on the oscillating amplitude, or KC number, and weakly dependent on the frequency parameter. Prislin et al. (1998) and Lake et al. (2000) focused their research on the added mass and damping of submerged horizontal plates. They were interested in the applicability of their research to spar type platforms, and hence assumed that the plates were deeply submerged.

Thiagarajan and Troesch (1998) observed the flow of cylinder+disc configuration using the Particle Image Velocimetry (PIV) technique. The vortex shedding pattern was found to be dependent on both flow parameters Keulegan-Carpenter and frequency parameter (KC , β) and on the geometry of the structure. For a disc with two edges oscillating at small amplitude, the flow was found to be symmetric about the mean position of oscillation. Vorticity shed from the edges rolls up into vortex rings, which do not convect away from the disc. They remain in the proximity of the disc due to low KC , until flow reversal causes a rapid cancellation of vorticity. The measurements showed that the disc was found to increase the pressure drag coefficients (C_d) two-fold. In the case that the thickness of the disc is very small, the two edges of the disc become virtually one single sharp edge, a well-established and reasonably stable vortex shedding pattern was generated by the single sharp edge. Vortex shedding occurred at a large angle of either positive or negative direction depending on starting condition.

Later, [Tao and Dray \(2008\)](#) performed experiments on solid and porous discs. They found that the damping coefficient was linearly dependent on the Keulegan-Carpenter number (KC) and that the influence of frequency on damping was weak. They confirmed [Pistani and Thiagarajan \(2006\)](#) research, who found the added mass to also be dependent on the amplitude of oscillation. [Vu et al. \(2008\)](#) also observed similar trends for added mass and damping coefficients of a solid disc with a varying KC number.

In order to examine the free-surface effects, [Molin et al. \(2008\)](#) performed forced harmonic model tests in heave of a horizontal circular thin disk (diameter 600 mm thickness 1 mm) with the two perforation ratios 10% and 20%. The submergences were 50 mm, 100 mm and 250 mm and the constant water depth was 500 mm. They emphasized, based both on numerical and experimental results, that the vortex shedding from the outer edges of the disk is important for both the heave added mass and damping for the largest amplitudes of oscillation. [Wadhwa and Thiagarajan \(2009\)](#) found that the hydrodynamic forces vary in the splash zone as the structure passes through the free surface, and can have significant effects on the life and performance of the module. [Wadhwa et al. \(2010\)](#) conducted forced oscillation experiments on a circular solid disk oscillating at varying elevations from a sandy seabed. Their study suggests that as a structure moves closer to the mean seabed the added mass and damping coefficients increase monotonically and the slope of the added mass curve decreases with increasing proximity to seabed. This perhaps gives an idea of what can happen near the seabed, i.e. continuous variation of hydrodynamic forces due to proximity with a surface.

Recently, [Li et al. \(2013\)](#) conducted a series of experiments in order to examine the influence of the edge shape on the hydrodynamics of heave plates. They found that the plate with a rectangular edge yielded the largest added mass value. The results also showed that damping did not seem to be significantly affected by the shape of the edge.

Although considerations of added mass and damping coefficients as a fundamental part of seakeeping dynamic models is well established since the early works to [Sarpkaya and Isaacson \(1981\)](#), their links to flow properties (vorticity, mechanical energy dissipation, pressure field, etc) are not well formulated. In addition, the scale effects to be accounted for when extrapolating model scale experiments have been hardly investigated.

1.5.2 Modelling

[Thiagarajan \(1993\)](#) noticed a difference in strengths of two consecutive vortices forming a pair, and interpreted that as due to a longer time period available for one of the vortices to develop depending on the starting direction of the oscillation. Some publications (e.g. [Roveri et al. \(1996\)](#) and [Cermelli et al. \(2003\)](#)) discuss the loads on the crane wire during

deployment of a subsea equipment. [Tao et al. \(1999\)](#) used a finite difference method based on boundary fitted coordinates to examine the axisymmetric flow generated by a surface piercing cylinder oscillating axially. Their study revealed that appendages such as discs could be added to the keel of a spar structure to effectively increase damping, also limiting the viscous excitation from waves due to the exponential decay with depth. Other numerical investigations ([Tao et al., 2000](#)) have shown that for a vertical cylinder with sharp bottom edge in heave, the flow separates at the sharp edge immediately and vortices are found at even very small KC . [Tao and Thiagarajan \(2000\)](#) extended the previous research, investigating numerically the effects of the corner radius of a TLP column on the springing damping forces, showing the influence of the corner radius on ambient flow pattern.

[Molin \(2001\)](#) studied arrays of porous discs in oscillatory flow perpendicular to their planes using potential flow theory. He concluded that no extra damping can be gained by making the disc porous when the KC number is larger than 1.0, but as the KC number becomes smaller, the heave damping of a porous disc is obviously larger than that of a solid disc. In addition, the added mass is sensitive to the amplitude of the motion. That is important in the vertical resonance of a spar platform. But the effects of the shape of the edge of the discs were not included in the potential flow approach used by [Molin \(2001\)](#). [Molin and Nielsen \(2004\)](#) analyzed a horizontally submerged and perforated disk heaving below the free-surface, and the water entry of a perforated wedge ([Molin and Korobkin, 2001](#)). When the KC number was relatively small, all the experimental and theoretical results for the perforated body studied in the above-mentioned papers were in good agreement.

[Tao and Thiagarajan \(2003a,b\)](#), using direct numerical simulation (DNS) based on finite difference method, investigated the flow structure and damping effects of discs attached to cylinders, finding different regimes of the flow where the damping showed different characteristics, and determining that thinner discs had higher form drag than thicker ones. [Tao and Cai \(2004\)](#) investigated the vortex shedding flow and the associated hydrodynamic behaviour of the cylinder+disc configuration at low KC numbers using an axisymmetric finite difference method. [Tao et al. \(2007\)](#) studied the nonlinear viscous flow problem associated with a heaving vertical cylinder with two heave plates in the form of two circular discs attached which is solved using a finite difference method.

More recently, [An and Faltinsen \(2013\)](#) studied forced harmonic heave motions of horizontally submerged perforated rectangular plates for both deep and shallow submergences. Their numerical results were partly obtained by combining the potential flow with linear free-surface conditions and a nonlinear viscous pressure loss condition at the mean oscillatory plate position. A domain decomposition technique was applied with a boundary element method in the inner domain and an analytical representation of the velocity poten-

tial in the outer domain. A drag term accounted for the vortex shedding at the outer plate edges. The numerically predicted KC dependent heave added mass and damping coefficients agreed reasonably with experimental values, in particular for deeper submergences. The hydrodynamic load is strongly dependent on the hydrodynamic coefficients of the structure being deployed, but as it was mentioned before, the works developed up to now are focused on the geometrical features and motion features, however there are a few researchers that focused their works in the influence on the hydrodynamic characteristics when the structures are moving close to the free surface or near the seabed. Therefore, the present work addresses the hydrodynamic problem to analyze the behaviour of a FOWT heave plates as one method to effectively improve the heave response of the platform system by providing additional damping and added mass. So, the aim of the present work is two-fold: theoretical formulations from first principles linking local flow physics with global force coefficients are presented. A numerical solver based on the open-source libraries of OpenFOAM (OpenCFD Ltd., 2013) is used to compute the hydrodynamic coefficients in the case of an oscillating body in an unbounded domain. Then, the numerical method is extended in order to study the effect of seabed and free surface proximity on the force coefficients. The analysis also includes the study of different edge geometries, and examines the sensitivities of the damping and added mass coefficients to the porosity of the plate. Numerical results are compared with experiments conducted at Technical University of Madrid (CEHINAV) and CEHIPAR model basins in Madrid and with others performed at School of Mechanical Engineering in The University of Western Australia (Wadhwa et al., 2010; Wadhwa and Thiagarajan, 2009).

Chapter 2

Objectives

2.1 Objectives of the study

Taking into account the review of the topic undertaken in Chapter 1, the following objectives for this PhD research are set:

1. Investigate the hydrodynamic force coefficients dependence with KC number using a Volume of Fraction (VOF) method in a finite volume open source solver OpenFOAM.
2. Investigate, with numerical analysis, the effect of the plate submergence and elevation from the seabed on the hydrodynamic force coefficients.
3. Investigate the links between the flow physics and the global force coefficients, by looking at the relation between energy dissipation, enstrophy and vortex shedding characteristics.
4. Analyze through experiments, whether scale effects in the added mass and damping are relevant.
5. To investigate numerically the dependence of the hydrodynamic force coefficients on the plate porosity.
6. To investigate numerically and experimentally the dependence of hydrodynamic coefficients on the presence and position of flaps.
7. To propose a novel heave plate design based on the generation of damping on fractal grids.

Chapter 3

Methodology

3.1 Methodology of the study

In order to achieve the objectives enumerated in previous chapter, the following tasks have been carried out, and are documented in the next chapters:

1. A review of the numerical modelling of the flow around a vertically oscillating single disc and a brief mathematical formulation which leads to the solution of the hydrodynamic problem and the governing equations are given in chapter 4, followed by the introduction and formulation of the dissipation mechanisms.
2. The parametric dependence of the hydrodynamic coefficients of heave plate on factors such as the KC number and the depth and seafloor elevation ratios are investigated in Chapter 5.
3. Chapter 6 considers the flow induced by the configuration of a vertical cylinder with a disc attached to the bottom, oscillating axially, corresponding to a semi-submersible platform column with a heave plate with this aim:
 - (a) The influence on hydrodynamic coefficients, of varying the depth, the oscillation amplitude and the frequency, of the semi-submersible platform column is investigated.
 - (b) Tests on plates at different scales, to perform a sensitivity study of scale and tests on plates with flaps, to study the influence of the shape of the edge on the hydrodynamics of the plates have been performed.

- (c) Finally, a set of tests on a fractal heave plate, to investigate the influence of the perforation ratio and hole sizes, on the hydrodynamics of the plates are carried out and results are discussed.

4. Chapter 7 summarizes the thesis main outcomes and suggests future work.

Chapter 4

Physical and numerical modelling

4.1 Introduction

In the present chapter, a brief mathematical formulation which leads to the solution of the hydrodynamic problem is described. The finite volume method (FVM) (LeVeque, 2002) has been used to discretize the governing equations. A harmonic model for the motion has been considered. This model allows to compute the hydrodynamic response by looking at individual wave excitation frequency. The response for these frequencies is obtained with forced excitation tests in which the fluid forces on the body are computed with the numerical solver. Open-source full CFD OpenFOAM (OpenCFD, 2013) has been used.

A solution to the Navier-Stokes equations with a Volume of Fluid (VOF, see Appendix E) technique (Hirt and Nichols, 1981) for the surface tracking is obtained idealizing the flow generated by the oscillating heave plate along its axis as axisymmetric by neglecting 3D effects by hypothesizing they have little influence on the longitudinal performance.

The PIMPLE algorithm that merged SIMPLE/PISO procedure (Semi-Implicit Method for Pressure-Linked Equation/Pressure Implicit with Splitting of Operators) was used to solve the Navier-Stokes equations (see Appendix D). OpenFOAM also has internal tools that allow to extract forces and moments from pressure and viscous effects in order to calculate the added mass and damping.

4.2 Review of numerical modelling of heave plates

Many researchers have studied the hydrodynamic problem with Computational Fluid Dynamics techniques, using vortex methods or RANS methods. Based on a discrete vortex method (DVM) the inviscid drag force due to vortex shedding of two-dimensional edges

was studied by [Graham \(1980\)](#) and [Bearman et al. \(1985\)](#). [Graham \(1980\)](#) found that the pattern of vortex shedding from a 2D isolated edge consists of one vortex pair of approximately equal and opposite strength shed per cycle (see Fig. 4.1). Since equalization of vorticity does not necessarily occur at the end of the second vortex formation, the pairing process splits the second vortex sheet leaving a smaller amount of residual vorticity to be engulfed by the next strong vortex.

[Bernardinis de et al. \(1981\)](#) assuming that vortex shedding is locally two dimensional, extended the method of discrete vortices to axisymmetric flows, obtaining similar results to the two-dimensional isolated edge flows of [Graham \(1980\)](#) up to a value of KC of about 3, but above this value the two results for 2D and axisymmetric disc diverge rapidly because the 3D effects in flow and force become important as KC increases.

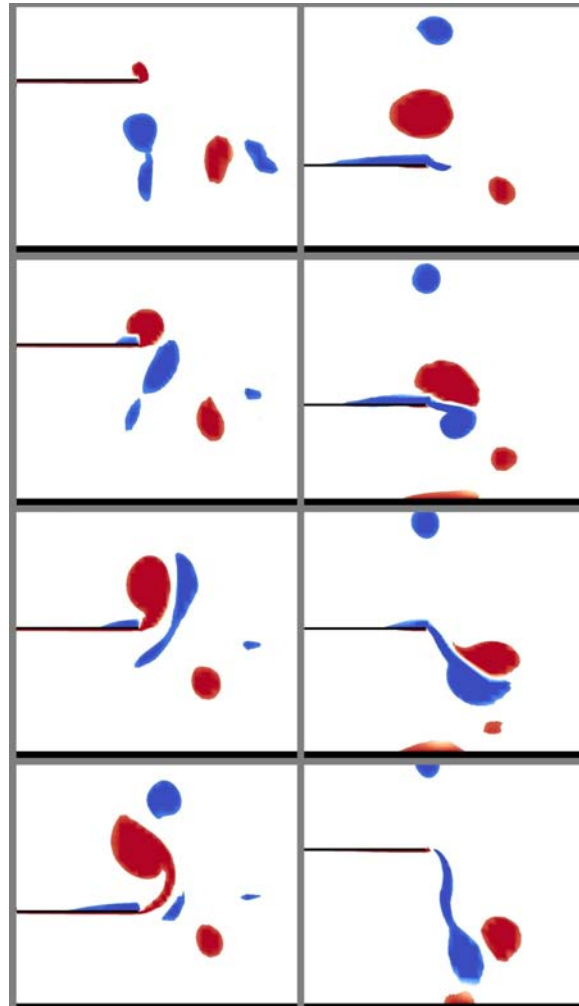


Fig. 4.1 Vortex generation around disc at $KC = 1.1$ from [Garrido-Mendoza et al. \(2013\)](#). Blue lines indicate negative vorticity (initial condition: Top Dead Centre. Spaced equally through one cycle of oscillation.

Molin (2001) studied arrays of porous discs in oscillatory flow perpendicular to their planes using potential flow theory. He concluded that no extra damping can be gained by making the disc porous when the KC number is larger than 1.0, but as the KC number becomes smaller, the heave damping of a porous disc is obviously larger than that of a solid disc. In addition, the added mass is sensitive to the amplitude of the motion. That is important in the vertical resonance of a spar platform. But the effects of the shape of the edge of the discs were not included in the potential flow approach used by Molin (2001).

Thiagarajan (1993) noticed a difference in strengths of two consecutive vortices forming a pair, and interpreted that as due to a longer time period available for one of the vortices to develop depending on the starting direction of the oscillation. Publications (e.g. Roveri et al. (1996) and Cermelli et al. (2003)) discuss the loads on the crane wire during deployment of a subsea equipment. Thiagarajan and Troesch (1998) observed the flow of cylinder+disc configuration using the Particle Image Velocimetry (PIV) technique. The vortex shedding pattern was found to be dependent on both flow parameters Keulegan-Carpenter and frequency parameter (KC , β) and the geometry of the structure. For a disc with two edges oscillating at small amplitude, the flow was found to be symmetric about the mean position of oscillation. Vorticity shed from the edges rolls up into vortex rings, which do not convect away from the disc. They remain in the proximity of the disc due to low KC , until flow reversal causes a rapid cancellation of vorticity. The measurements showed that the disc was found to increase the pressure drag coefficients (C_d) two-fold. In the case that the thickness of the disc is very small, the two edges of the disc become virtually one single sharp edge, a well-established and reasonably stable vortex shedding pattern was generated by the single sharp edge. Vortex shedding occurred at a large angle of either positive or negative direction depending on starting condition.

Other numerical investigations (Tao et al., 2000) have shown that for a vertical cylinder with sharp bottom edge in heave, the flow separates at the sharp edge immediately and vortices are found at even very small KC . Tao and Thiagarajan (2000) extended the previous research, investigating numerically the effects of the corner radius of a TLP column on the springing damping forces, showing the influence of the corner radius on ambient flow pattern.

Later, Tao and Thiagarajan (2003a,b) using direct numerical simulation (DNS) based on finite difference method investigated the flow structure and damping effects of discs attached to cylinders, finding different regimes of the flow where the damping showed different characteristics, and determining that thinner discs had higher form drag than thicker ones, and Tao and Cai (2004) investigated the vortex shedding flow and the associated hydrodynamic behaviour of the cylinder+disc configuration at low KC numbers using an axisymmetric

finite difference method.

More recently, [Tao et al. \(2007\)](#) studied the nonlinear viscous flow problem associated with a heaving vertical cylinder with two heave plates in the form of two circular discs attached which is solved using a finite difference method, and [An and Faltinsen \(2013\)](#) combining potential flow with linear free-surface conditions and a nonlinear viscous pressure loss condition at the mean oscillatory plate position to study forced small-amplitude vertical harmonic oscillations of a horizontally submerged and perforated rigid plate in the frequency domain.

The present work studies numerically the hydrodynamic coefficients of solid and porous heave plates in the context of their use as heave dampers for offshore structures oscillating close to the free surface and near seabed. Results from forced heave oscillation obtained in this study are compared with experimental data.

4.3 Theoretical formulation

4.3.1 Fluid governing equations.

As a starting point for the theoretical formulation, a fluid domain Ω is considered, whose boundaries, $\partial\Omega$, consist of a free surface, $\partial\Omega_F$, a solid boundary (comprising of the moving disc $\partial\Omega_B$, the seabed $\partial\Omega_G$), and a non-reflecting lateral boundary $\partial\Omega_C$ (Fig. 4.2).

The following set of monophasic incompressible Navier Stokes equations for a Newtonian fluid is considered:

$$\text{div}(\mathbf{u}) = 0, \quad (4.1)$$

$$\frac{D\mathbf{u}}{Dt} = \mathbf{f} + \frac{\text{div}(\mathbb{T})}{\rho}, \quad (4.2)$$

where D/Dt represents the Lagrangian derivative, \mathbf{u} the flow velocity, ρ is the fluid density, \mathbb{T} the stress tensor and \mathbf{f} is a generic specific body force.

The fluid is assumed to be Newtonian, therefore, the stress tensor can be written as:

$$\mathbb{T} = -p\mathbb{I} + 2\mu\mathbb{D}, \quad (4.3)$$

where p is the pressure, \mathbb{D} is the rate of strain tensor, i.e. $\mathbb{D} = (\nabla\mathbf{u} + \nabla\mathbf{u}^T)/2$, and finally, μ is the dynamic viscosity.

The stress on the fluid domain boundaries $\partial\Omega$ is:

$$\mathbb{T}\mathbf{n} = -p\mathbf{n} + \mu(\mathbf{n} \times \boldsymbol{\omega}) + 2\mu\nabla\mathbf{u}\mathbf{n}, \quad (4.4)$$

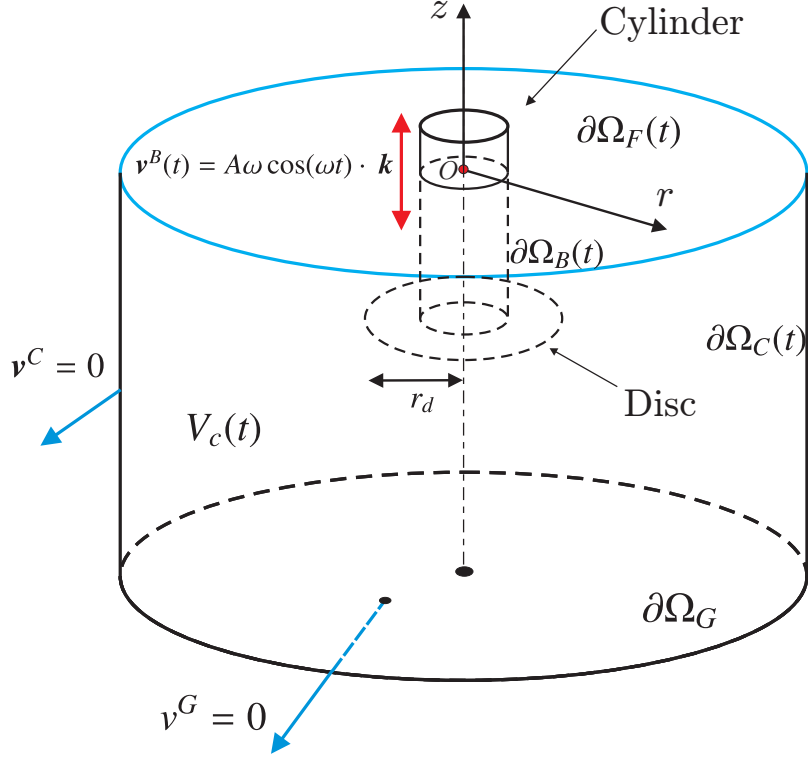


Fig. 4.2 Reference System and physical domain for a cylinder with a disk attached on its bottom subjected to heave motion. Origin at the intersection of the cylinder axis with the undisturbed free surface. Velocities refer to control surface.

where $\omega = \text{curl}(\mathbf{u})$.

On $\partial\Omega_B$ Eqn. (4.4) becomes:

$$\mathbb{T}\mathbf{n}_B = -p\mathbf{n}_B + \mu(\mathbf{n}_B \times \omega) + 2\mu \frac{\partial \mathbf{u}}{\partial \mathbf{n}_B}. \quad (4.5)$$

Therefore, the stress on the body is composed of three terms: the first one being a normal pressure term, the second and third ones being friction stress terms on the body surface. The same applies to the bottom boundary $\partial\Omega_G$.

4.3.2 Mechanical energy

The power that the fluid exerts on the moving body (heave plate), $P_{fluid/body}$, is obtained by integrating the power of the fluid stress acting on each body surface element:

$$P_{fluid/body} = - \int_{\partial\Omega_B} \mathbb{T}\mathbf{n} \cdot \mathbf{u} dS, \quad (4.6)$$

with n being the unit normal pointing outwards the fluid domain.

The power $-P_{fluid/body} = P_{body/fluid} := P_{ext}$ is converted into an energy variation of the fluid. An equivalent way to define the power using the divergence theorem gives:

$$P_{ext} = \int_{\Omega} \operatorname{div}(\mathbb{T}\mathbf{u}) dV. \quad (4.7)$$

Using the divergence theorem, Eqn. (4.7) becomes:

$$\int_{\Omega} (\operatorname{div} \mathbb{T}) \cdot \mathbf{u} dV = P_{ext} - \int_{\Omega} \mathbb{T} : \mathbb{D} dV \quad (4.8)$$

Using momentum conservation (Eqn. 4.2), Eqn. (4.8) can be written as:

$$\int_{\Omega} \operatorname{div}(\mathbb{T}) \cdot \mathbf{u} dV = \int_{\Omega} \left(\rho \frac{D\mathbf{u}}{Dt} - \rho \mathbf{f} \right) \cdot \mathbf{u} dV. \quad (4.9)$$

The conservative body forces are \mathbf{g} and \mathbf{f}_{NC} . The former admits a potential field G . In the case where there is only the gravity force field then $\nabla G = \mathbf{g}$, and $G = -gz$ where z is the vertical coordinate. Using the transport theorem and the continuity equation (see Appendix A), we get:

$$\int_{\Omega} \operatorname{div}(\mathbb{T}) \cdot \mathbf{u} dV = \frac{D}{Dt} \int_{\Omega} \rho \left(\frac{\mathbf{u}^2}{2} - G \right) dV. \quad (4.10)$$

We can define:

$$\mathcal{E}_K := \int_{\Omega} \frac{\mathbf{u}^2}{2} \rho dV, \quad \mathcal{E}_P := \int_{\Omega} -G \rho dV, \quad (4.11)$$

where \mathcal{E}_K is the kinetic energy and \mathcal{E}_P the potential energy with their sum giving the mechanical energy:

$$\mathcal{E}_M = \mathcal{E}_P + \mathcal{E}_K. \quad (4.12)$$

Therefore,

$$\int_{\Omega} \operatorname{div}(\mathbb{T}) \cdot \mathbf{u} dV = \dot{\mathcal{E}}_M. \quad (4.13)$$

The second term of Eqn. (4.8) is the derivative of the internal energy and can be expressed for an incompressible medium as:

$$\int_{\Omega} \mathbb{T} : \mathbb{D} dV = 2\mu \int_{\Omega} \mathbb{D} : \mathbb{D} dV. \quad (4.14)$$

This represents the classical viscous dissipation term for a Newtonian fluid. It is always

negative, for which the dissipative power may be defined as:

$$\dot{\mathcal{E}}_D := -2\mu \int_{\Omega} \mathbb{D} : \mathbb{D} dV. \quad (4.15)$$

Hence, Eqn. (4.8) can be rewritten as:

$$P_{ext} - \dot{\mathcal{E}}_M = \dot{\mathcal{E}}_D, \quad (4.16)$$

meaning that the power due to the external forces minus the mechanical energy of the fluid variation is balanced by the power dissipated by the fluid.

4.3.3 Dissipation

If the total head of the flow is defined, following (Larsson and Baba, 1996), as $H := \rho \mathbf{u}^2/2 + \rho g z + p$, then, for a fluid domain with zero velocity ($\mathbf{v}^C = 0$) on the lateral control surface $\partial\Omega_C(t)$ (Fig. 4.2), the mechanical energy balance on the control volume $V_C(t)$ reads:

$$\begin{aligned} \dot{\mathcal{E}}_M &= P_{body/fluid}^{Pressure} + P_{body/fluid}^{Viscous} \\ &\quad - \int_{\partial\Omega_C(t)} [H\mathbf{n} + \mu(\boldsymbol{\omega} \times \mathbf{n})] \cdot \mathbf{u} dS \\ &\quad + \dot{\mathcal{E}}_{\omega} + \dot{\mathcal{E}}_{FS}, \end{aligned} \quad (4.17)$$

where the terms in the RHS are defined as (see Appendix B for details):

$$P_{body/fluid}^{Pressure} := - \int_{\partial\Omega_B} p \mathbf{u} \cdot \mathbf{n} dS, \quad (4.18)$$

$$P_{body/fluid}^{Viscous} := -\mu \int_{\partial\Omega_B} (\boldsymbol{\omega} \times \mathbf{n}) \cdot \mathbf{u} dS, \quad (4.19)$$

$$\dot{\mathcal{E}}_{\omega} := -\mu \int_{\Omega} \boldsymbol{\omega}^2 dV, \quad (4.20)$$

$$\dot{\mathcal{E}}_{FS} := -2\mu \int_{\partial\Omega_F} (\nabla \mathbf{u} \mathbf{u}) \cdot \mathbf{n} dS. \quad (4.21)$$

Considering the solid surface boundary conditions and assuming vertical translation only for the body (no rotation), with $\mathbf{v}_B(t)$ being a sinusoidal function:

$$P_{body/fluid}^{Pressure} := \mathbf{v}_B(t) \cdot \mathbf{F}_{body/fluid}^{Pressure}, \quad (4.22)$$

$$P_{body/fluid}^{Viscous} := \mathbf{v}_B(t) \cdot \mathbf{F}_{body/fluid}^{Viscous}. \quad (4.23)$$

where,

$$\mathbf{F}_{body/fluid} = \mathbf{F}_{body/fluid}^{Pressure} + \mathbf{F}_{body/fluid}^{Viscous}. \quad (4.24)$$

Usually, the enstrophy term (Eqn. 4.20) is the largest contribution in dissipative free surface flows, however and in some cases, the free surface integral (Eqn. 4.21) can also be important, see e.g. Colagrossi et al. (2013). However, in present research, due to the large distance between the disc and the free surface, the disturbances in the free surface are expected to be very small, and the free surface viscous term $\dot{\mathcal{E}}_{FS}$ will be, for this reason, neglected.

Considering a body moving harmonically in z (Fig. 4.2), with velocity $\mathbf{v}_B(t)$, and integrating over a cycle, Eqn. (4.17) becomes:

$$\begin{aligned} \int_t^{t+T} \dot{\mathcal{E}}_M dt &= \int_t^{t+T} \mathbf{v}_B(t) \cdot \mathbf{F}_{body/fluid} dt - \\ &\quad \int_t^{t+T} \int_{\partial\Omega_C(t)} [H\mathbf{n} + \mu(\boldsymbol{\omega} \times \mathbf{n})] \cdot \mathbf{u} dS dt + \\ &\quad \int_t^{t+T} \dot{\mathcal{E}}_\omega dt. \end{aligned} \quad (4.25)$$

At the “T-periodic state”, the mechanical energy variation is null, thus implying that all the external power is dissipated by the fluid. The precedent expression then becomes:

$$\begin{aligned} \int_t^{t+T} \mathbf{v}_B(t) \cdot \mathbf{F}_{body/fluid} dt &= \int_t^{t+T} \int_{\partial\Omega_C(t)} [H\mathbf{n} + \mu(\boldsymbol{\omega} \times \mathbf{n})] \cdot \mathbf{u} dS dt - \\ &\quad \int_t^{t+T} \dot{\mathcal{E}}_\omega dt. \end{aligned} \quad (4.26)$$

It is convenient to note that if $\partial\Omega_C$ is far enough from the body, the vorticity is diffused inside the domain and the vorticity term flux in RHS of Eqn. (4.26) can be neglected. In addition and due to the large distance to the free surface, the oscillating body does not irradiate energy through the generation of gravity waves, the term that goes with H in Eqn. (4.26) can therefore also be neglected. The following expression for our continuous model, exact under such assumptions, applies:

$$\int_t^{t+T} \mathbf{v}_B(t) \cdot \mathbf{F}_{body/fluid} dt \approx - \int_t^{t+T} \dot{\mathcal{E}}_\omega dt. \quad (4.27)$$

This equation demonstrates that the power exerted by the body on the fluid can be directly correlated to the net change in the enstrophy per cycle.

4.4 Physical model

4.4.1 Numerical solution

Solution of the NS equations is complicated by the lack of an independent equation for the pressure, whose gradient contributes to each of the two momentum components equations. Furthermore, for incompressible flows the continuity equation becomes an additional constraint on the velocity field. A way to overcome this difficulty is to construct the pressure field such that velocity satisfies the continuity equation. This is done by modifying the continuity equation into an equation for pressure (Ferziger and Peric, 1999).

To obtain approximate solutions numerically, a discretisation method which approximates the differential equations by a system of algebraic equations has been used. The Finite Volume Method (FVM) implemented in the free software package OpenFoam (OpenCFD Ltd., 2013) has been used in this work.

The FVM and others, such as the finite element and finite difference methods, all discretize the problem as follows:

- **Spatial discretisation.** Defining the solution domain by a set of points that fill and bound a region of space when connected;
- **Temporal discretisation** (For transient problems). Dividing the time domain into into a finite number of time intervals, or steps;
- **Equation discretisation.** Generating a system of algebraic equations in terms of discrete quantities defined at specific locations in the domain, from the PDEs that characterise the problem.

The discretisation of the solution domain (see Fig. 4.3) produces a computational mesh on which the governing equations are subsequently solved. It also determines the positions of points in space and time where the solution is sought. Discretisation of time, if required, is simple: it is broken into a set of time steps Δt that may change during a numerical simulation, perhaps depending on some condition calculated during the simulation. The discretisation of space for the Finite Volume method used in this study requires a subdivision of the domain into control volumes (CV). Control volumes do not overlap and completely fill the computational domain.

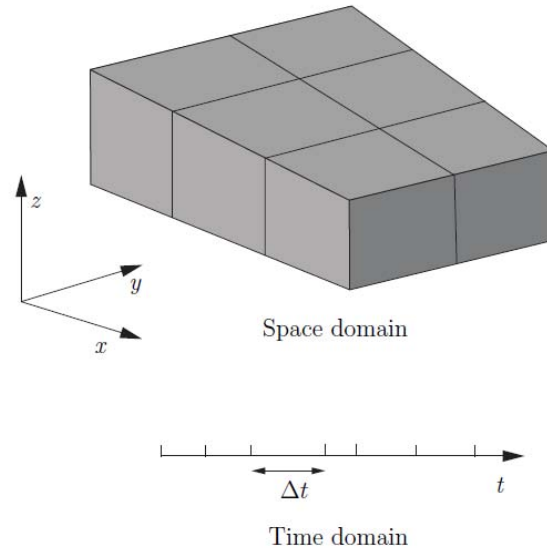


Fig. 4.3 Discretisation of the solution domain.

The CV is bounded by a set of faces and each face is shared with only one neighbouring CV. The face area vector n_f is constructed for each face in such a way that it points outwards from the “owner” and towards the “neighbour” cell, is normal to the face and has the magnitude equal to the area of the face, S_f . For the shaded face, the owner and neighbour cell centres are marked with P and N respectively. For simplicity, all the faces of the control volume will be marked with f , which also represents the point in the middle of the face (see Fig. 4.4).

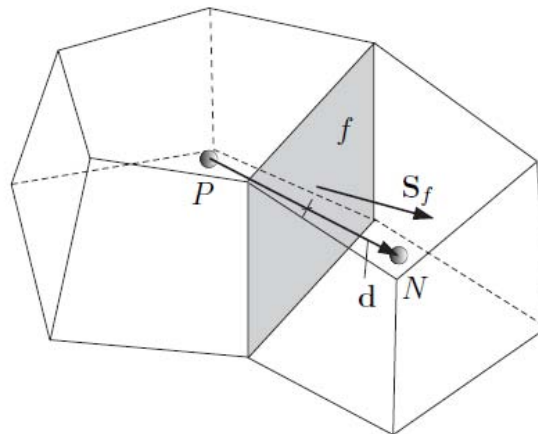


Fig. 4.4 Parameters in finite volume discretisation.

Dependent variables and other properties are principally stored at the cell centroid P although they may be stored on faces or vertices. The cell is bounded by a set of flat faces,

given the generic label f . In OpenFOAM there is no limitation on the number of faces bounding each cell, nor any restriction on the alignment of each face. This kind of mesh is often referred to as “arbitrarily unstructured” to differentiate it from meshes in which the cell faces have a prescribed alignment, typically with the coordinate axes.

Detailed descriptions of its implementation can be found in [Versteeg and Malalasekera \(1995\)](#), [Ferziger and Peric \(1999\)](#) and [Ubbink \(1997\)](#). Details of the pressure-velocity coupled algorithm and volume of fluid method implemented in OpenFOAM are presented in Appendix D and E.

4.4.2 Hydrodynamic modelling of semi-submersible FOWT concept

A forced harmonic vertical motion of a rigid body, with amplitude A and frequency ω , centered in the coordinate z_0 (see Fig. 4.2):

$$z(t) = z_0 + A \sin(\omega t), \quad (4.28)$$

is considered.

It is assumed that the two parameters that govern the small amplitude oscillating flow induced by the heave oscillation of a structure are the Keulegan-Carpenter number (KC) and the frequency parameter (β):

$$KC = 2\pi \frac{A}{D_d}, \quad (4.29)$$

$$\beta = \frac{D_d^2 f}{\nu}, \quad (4.30)$$

where f is the frequency in Hz of the oscillation, D_d is the disc diameter and ν is the kinematic viscosity of the fluid. Discussion of these parameters can be found in [Keulegan and Carpenter \(1958\)](#) and [Sarpkaya and Isaacson \(1981\)](#). One can obtain a Reynolds number based on the oscillation velocity of the disc as:

$$Re = KC \cdot \beta = \frac{A \omega D_d}{\nu}. \quad (4.31)$$

In addition, the elevation ratio h/r_d is considered to have an effect on the added mass and damping coefficients when the disc oscillates close to the seabed. Under these assumptions, in non-dimensional terms, the hydrodynamic coefficients are functions of KC , β and h/r_d . For a heave plate oscillating in heave, the added mass is approximately equal to the mass of fluid contained in an imaginary sphere of the same radius as the disc and the natural heave

period for a semi-submersible can be written as:

$$T_{33} = 2\pi \sqrt{\left(\frac{m + A_{33}}{\rho g S_w}\right)}, \quad (4.32)$$

4.4.3 Hydrodynamic force calculation.

The hydrodynamic force on the heave plate under prescribed harmonic motion in uniform flow is based on Morrison's equation and Fourier averaged method. In this section we will define the hydrodynamic coefficients used in this thesis, and specify how they are calculated from the calculated and measured force and motion signals.

4.4.4 Numerical tests

The hydrodynamic heave force on the disc was calculated using a Tool for post-processing force/lift/drag data with function tool available in OpenFOAM. The motions of the disc were restricted to axial (heave) direction.

The body is a fully-submerged plate, whose hydrostatic restoring is therefore zero. The vertical component of the hydrodynamic force is here modeled considering added mass, A_{33} , and linear damping, B_{33} , as:

$$-A_{33} \ddot{z}(t) - B_{33} \dot{z}(t) \approx \mathbf{F}_{fluid/body}(t) \cdot \mathbf{k}. \quad (4.33)$$

According to [Molin et al. \(1999\)](#), when close to a flat solid boundary, an extra term in Eqn. (4.33) is necessary to consistently model added mass related forces, namely:

$$-A_{33}(z) \ddot{z}(t) - \frac{1}{2} \frac{\partial A_{33}(z)}{\partial z} \dot{z}^2(t) - B_{33}(z) \dot{z}(t) \approx \mathbf{F}_{fluid/body}(t) \cdot \mathbf{k}. \quad (4.34)$$

Let's expand this equation in the vicinity of $z = z_0$:

$$\begin{aligned} -A_{33}(z_0) \ddot{z}(t) - \left. \frac{\partial A_{33}(z)}{\partial z} \right|_{z_0} \ddot{z}(t) \Delta z - \frac{1}{2} \left. \frac{\partial A_{33}(z)}{\partial z} \right|_{z_0} \dot{z}^2(t) - \frac{1}{2} \left. \frac{\partial^2 A_{33}(z)}{\partial z^2} \right|_{z_0} \dot{z}^2(t) \Delta z \\ - B_{33}(z_0) \dot{z}(t) - \left. \frac{\partial B_{33}(z)}{\partial z} \right|_{z_0} \dot{z}(t) \Delta z \\ \approx \mathbf{F}_{fluid/body}(t) \cdot \mathbf{k}, \end{aligned} \quad (4.35)$$

with $\Delta z := z - z_0$, and dropping terms on $(\Delta z)^2$ on the basis of small or moderate KC 's.

If Eqn. (4.35) is multiplied by \ddot{z} and integrated over one period, the following expression is obtained:

$$\begin{aligned} \int_t^{t+T} A_{33}(z_0) \ddot{z}^2(t) dt + \frac{1}{2} \int_t^{t+T} \left. \frac{\partial^2 A_{33}(z)}{\partial z^2} \right|_{z_0} \dot{z}^2(t) \Delta z \ddot{z}(t) dt \\ = \int_t^{t+T} \ddot{z}(t) \cdot \mathbf{F}_{body/fluid}(t) \cdot \mathbf{k} dt. \end{aligned} \quad (4.36)$$

This equation has been solved iteratively for each case, neglecting the second order derivative term in the first iteration, and incorporating it after its estimation from $A_{33}(z)$ obtained in the first iteration, and so on. It has been found that, in all cases analyzed, the weight of the second order derivative term in the equation is basically negligible.

On the other hand, if Eqn. (4.35) is multiplied by $\dot{z}(t)$ and integrated over one period, B_{33} can be directly obtained since only one summand survives in the projection:

$$B_{33} = \frac{\int_t^{t+T} \dot{z}(t) \cdot \mathbf{F}_{body/fluid}(t) \cdot \mathbf{k} dt}{\int_t^{t+T} \dot{z}^2(t) dt}. \quad (4.37)$$

Taking into account that $\mathbf{v}_B = \dot{z} \cdot \mathbf{k}$, this expression can be written as:

$$B_{33} = \frac{\int_t^{t+T} \mathbf{v}_B(t) \cdot \mathbf{F}_{body/fluid}(t) dt}{\int_t^{t+T} \mathbf{v}_B^2(t) dt}. \quad (4.38)$$

Substituting into Eqn. (4.27), we get an approximation of the linear damping coefficient from the analysis of the flow vorticity field, expressed as:

$$B_{33\omega} := \frac{\int_t^{t+T} \dot{\mathcal{E}}_\omega dt}{\int_t^{t+T} \mathbf{v}_B^2(t) dt}. \quad (4.39)$$

Thus we have obtained an explicit expression relating the global damping coefficient with the rate of change of enstrophy.

4.4.5 Experimental tests

In the case of experiments, the hydrodynamic force $\mathbf{F}_{fluid/body}(t)$ is then given by properly subtracting the body inertia force, $\mathbf{F}_I(t)$, and the hydrostatic restoring, $\mathbf{F}_K(t)$, from the

measured force $\mathbf{F}_{meas}(t)$. That is:

$$\mathbf{F}_{fluid/body}(t) = \mathbf{F}_{meas}(t) - \mathbf{F}_I(t) - \mathbf{F}_K(t), \quad (4.40)$$

$$\mathbf{F}_I(t) = -z\omega_1^2 m, \quad (4.41)$$

$$\mathbf{F}_K(t) = -zS_w\rho g. \quad (4.42)$$

The heave added mass A_{33} and damping coefficient B_{33} of the heave plate are calculated from the corresponding selected time history of the total force $\mathbf{F}_{fluid/body}(t)$ (Eqn. 4.40), velocity $\dot{z}(t)$, acceleration $\ddot{z}(t)$ and displacement $z(t)$ using a fourier projection method and by expressing the force as in the Eqn. (4.43). We can assume that the hydrodynamic force may be represented by a linear combination of acceleration and velocity signals.

$$-B_{33} \cdot \dot{z}(t) - A_{33} \cdot \ddot{z}(t) = \mathbf{F}_{fluid/body}(t). \quad (4.43)$$

The hydrodynamic coefficients are defined as follow, (Wadhwa et al., 2010):

$$A_{33} = \frac{F_{body/fluid,1} \cos(\phi)}{\omega^2 A}, \quad (4.44)$$

$$B_{33} = \frac{F_{body/fluid,1} \sin(\phi)}{\omega A}, \quad (4.45)$$

where $F_{body/fluid,1}$ and A are the magnitudes of the first harmonic component in the force and displacement respectively, ϕ is the phase angle between the force and the heave plate motion.

The added mass coefficient is based on the force in phase with acceleration normalized with respect to the mass of the displaced water and the acceleration amplitude of the harmonic oscillation, $\omega^2 A$, and the damping coefficient is based on the force in phase with velocity.

Hydrodynamic coefficients (from numerical and experimental results) are presented in their non-dimensional form, as follows:

$$C_a = \frac{A_{33}}{M_a}, \quad (4.46)$$

$$C_b = \frac{B_{33}}{\omega M_a}, \quad (4.47)$$

where M_a is the added mass in an unbounded fluid, defined as $M_a = 8/3 \rho r_d^3$, (Sarpkaya and

Isaacson, 1981).

4.4.6 Numerical model of turbulence

Since early last century, a number of turbulence models have been developed to improve the performance of numerical simulations for a large variety of different two or three dimensional flow problems especially at high Reynolds numbers. The central concept is to average the governing equations over a time or space scale so that the resultant equations describe the distribution of the mean velocity and pressure in the flow. This is acceptable from an engineering point of view since the mean motion rather than the details of the fluctuating motion is of primary interest for engineers in most practical calculations. The introduction of turbulence models serves to provide closure to the time or space averaged governing equations which contain unknown terms representing the transport of turbulent motion.

Numerical calculation of the springing damping of a single cylinder was performed by Huse and Utnes (1994) and Utnes et al. (1995). The axisymmetric numerical model is based on Reynolds equations with a one-equation turbulence closure. A Galerkin finite element method is used to solve the equations. For the momentum equations a fractional step formulation is applied. An intermediate velocity is first computed by neglecting the pressure, the pressure field is then computed from a Poisson equation, and the velocity field is finally corrected by including the pressure effect. The intermediate velocity and the turbulence equations are computed using a weak form of the characteristics method. No distinct difference among the results of laminar and turbulence modelling was found from the calculations.

There is good agreement among the previous investigations that the boundary layer is expected to be laminar in model scale as well as prototype TLP in springing oscillations due to their very small amplitudes (Huse and Utnes, 1994). Therefore, in the present study, the numerical calculations of viscous damping of heave plates configurations are based on the Navier-Stokes formulation, omitting any turbulence modelling.

Prislin et al. (1998) examined how the added mass and drag coefficients of a solid square-plate in infinite fluid vary with the Reynolds number (the width of the plate being the characteristic length) and with the KC number. Their conclusion was that the added mass of solid plates does not depend on the Reynolds number and that the drag coefficient at Reynolds numbers higher than 10^5 does not vary significantly with Reynolds number.

The Reynolds number of the present simulations is large and therefore significant turbulence may develop. However, the boundary layer separation takes place at a known location (the plate edge), and the size of the vortical structures is relatively large (of the order of the motion amplitude) and, hence, insensitive to subgrid RANS modelling. For these reasons,

at this stage of the present work, no turbulence modelling has been included in the numerical model.

4.4.7 Computational tool

The OpenFOAM (Open Source Field Operation and Manipulation) software is an open source computational fluid dynamic software that was first released in 2004. OpenFOAM is essentially a C++ library that is used to create applications. Applications can be solvers or utilities. Solvers are designed to solve a specific physical problem in continuum mechanics and utilities are used to perform tasks that involve data manipulation (OpenCFD, 2013). OpenFOAM comes pre-equipped with many solvers and utilities.

OpenFOAM is supplied with pre and post-processing environments. The interface to the pre- and post-processing are themselves OpenFOAM utilities, thereby ensuring consistent data handling across all environments. The overall structure of OpenFOAM is shown in Fig. 4.5.

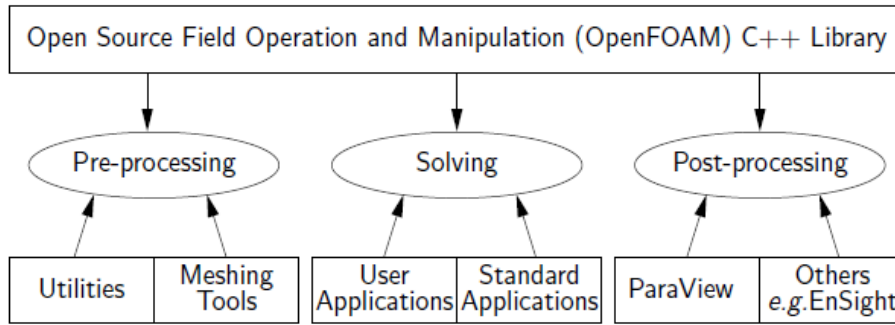


Fig. 4.5 Overview of OpenFOAM structure.

The unsteady incompressible finite volume solver “interDyMFoam”, implemented in OpenCFD (2013) has been used in present work. It uses a Volume of Fluid method (VoF) (Hirt and Nichols, 1981) to track the free surface evolution. In this method the two phases are considered as a single phase characterized by a volume fraction ($\alpha \in [0; 1]$). The free surface (interface between two phases) is not a sharp surface, but a region where further mesh refinements are made. Using a two phase model is a computational convenience. Since free surface breaking does not place and since the gas phase density is very low, such two phase model can be considered a good approximation to the monophasic governing equations presented in previous section.

The *PIMPLE* algorithm (Ubbink, 1997), (Ferziger and Peric, 1999) is used in the coupling of continuity and momentum equations. This algorithm guesses pressure and flux using values

from the previous time step, and uses momentum equation in order to find the velocity. An equation, obtaining the pressure, is then solved and fluxes are finally corrected in order to satisfy continuity. All steps must be repeated until convergence task is achieved.

The schemes implemented for both convection divergence and laplacian terms were the bounded *vanLeer* limiter (but to produce smoother interfaces in this work the specialised *interfaceCompression* scheme will be used) and the unbounded second order *linear corrected*, respectively were used. The first time derivative term of the transient time scheme implemented in this model used the *Euler* scheme, which is the first order, bounded and implicit scheme available in OpenFOAM for solving ordinary differential equations (OpenCFD, 2013). The generalised *geometric algebraic multi-grid* (GAMG) were used to discretized pressure and cell displacement, and *smoother GaussSeidel* to discretized velocity governing equations.

It is important to underline that results obtained by the application of numerical method must be independent from the grid used in the calculation. For this reason a mesh have to be fine enough in order to evaluate the variation in space of variables, but it must be taken into account that computational efforts grow up with the growth of the number of cells. The next Chapters (5 and 6) shown the convergence analysis, both in time and mesh generation for each study case analyzed in this work.

4.4.8 Validation of numerical procedure

The validation of the numerical model has been carried out in three stages. First, a comparison of the calculated damping ratio with the experimental results of Thiagarajan and Troesch (1998) for a cylinder + disc configuration was done, second, the same was done for the experimental work done by Wadhwa et al. (2010), and third, flow pattern comparisons with the flow visualization experiments of He et al. (2008) were conducted. Details of an extensive convergence studies and mesh definition can be found in Garrido-Mendoza et al. (2013).

In the first stage, the damping ratios from Thiagarajan and Troesch (1998) are taken as reference. The damping ratio allows for the dependence of the viscous damping on the geometry of the disc to be examined. The damping ratio can be defined as:

$$Z = \frac{1}{3\pi^2} C_G \frac{C_d}{C_m} KC, \quad (4.48)$$

where C_G is a geometric constant depending on the geometry of the cylinder + disc configuration, C_d and $C_m = 1 + C_a$ are the drag coefficient and the inertia coefficient, respectively, calculated from time history force. More details of the formulation can be found in Thia-

garajan and Troesch (1998). Fig. 4.6 shows the results of the damping ratio of the cylinder + disc configuration at different amplitudes of oscillation and a good agreement is seen between the experimental and numerical data.

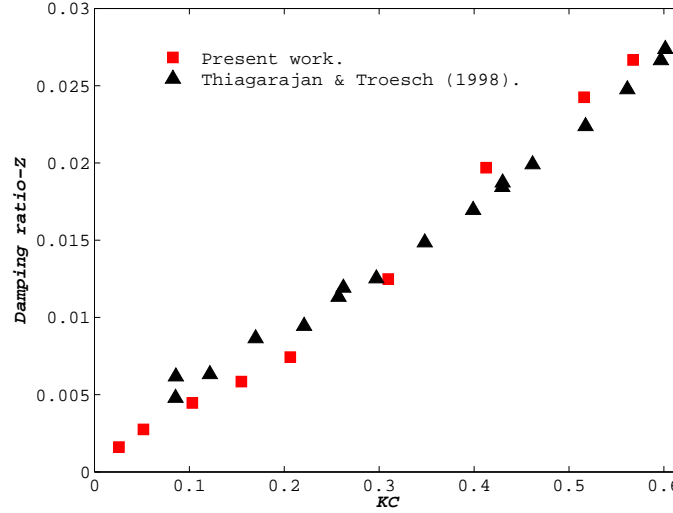


Fig. 4.6 Damping ratio Z vs. KC for a cylinder with disc using Eqn. (4.48).

The second set of validation simulations were aimed at numerically reproducing the experimental work done by Wadhwa et al. (2010) for a solid disc 200 mm in diameter, 2 mm thick, oscillating at amplitudes varying from 1 to 48 mm and an elevation h of the disc from the seabed varying between 0.2 and 2 times the disc radius. Figs. 4.7(a) and 4.7(b) show a comparison with the published experimental data of Wadhwa et al. (2010), Vu et al. (2008) and Tao and Dray (2008) for different KC ranges. Our results for added mass and damping show similar behaviour to the curves obtained by Tao and Dray (2008).

Fig. 4.7(a) presents a larger C_a value for simulations in comparison to experiments, although the behaviour for smaller KC tends to the theoretical value, which does not happen in experiments of Wadhwa et al. (2010). Some differences could be attributed to the fact that all experiments were conducted in a finite volume of fluid (e.g. Wadhwa et al. (2010) work was conducted in a 1 m³ tank). Some effects of the flow recirculating in the tank could have contributed to the difference. Furthermore, some experimental values were consistently higher than others, pointing to some calibration or zeroing errors.

Compared to flow visualization based on experiments, flow visualization based on well validated numerical procedures can provide more details about the flow field, which can be useful in order to understand the mechanisms of vortex shedding. Fig. 4.8 shows a comparison between present numerical simulations and the experiments performed by He et al. (2008). The frames have been evenly spaced over one period starting at top dead

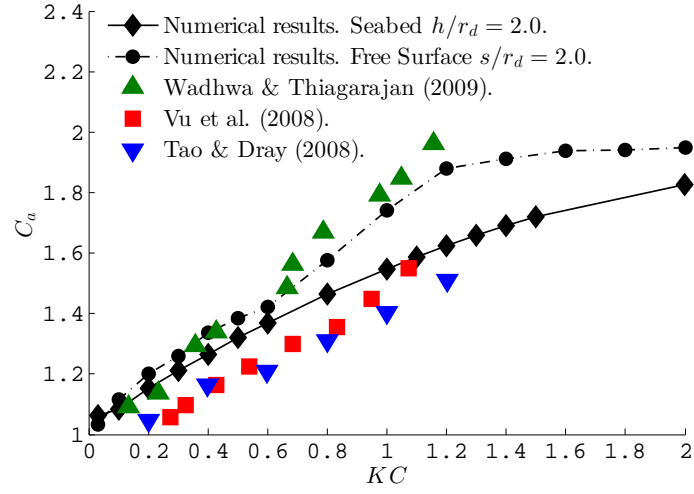
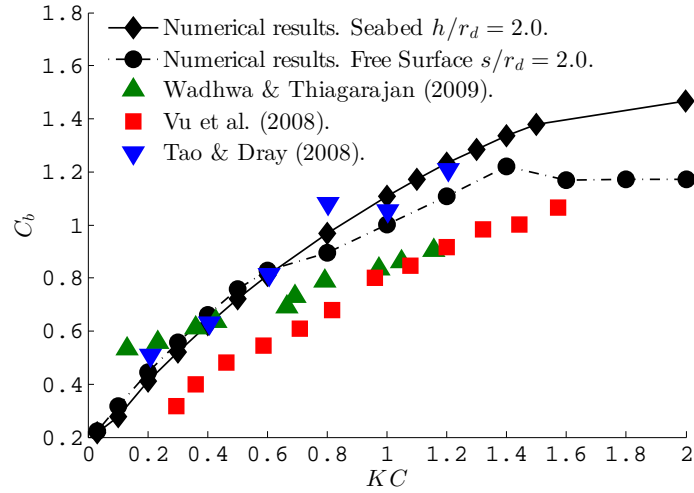
(a) Added mass coefficient C_a using Eqn. (4.46).(b) Damping coefficient C_b using Eqn. (4.47).

Fig. 4.7 Comparison of numerical and experimental added mass and damping coefficients for an oscillating heave plate.

centre (TDC). The results have been obtained with a disc whose thickness-diameter ratio is $t_d/D_d = 1/87.5$ and forced to oscillate sinusoidally in calm water, with a KC number of 0.16. Qualitatively, the agreement between experiments and simulations, in the location of the vortical structures, can be considered reasonable.

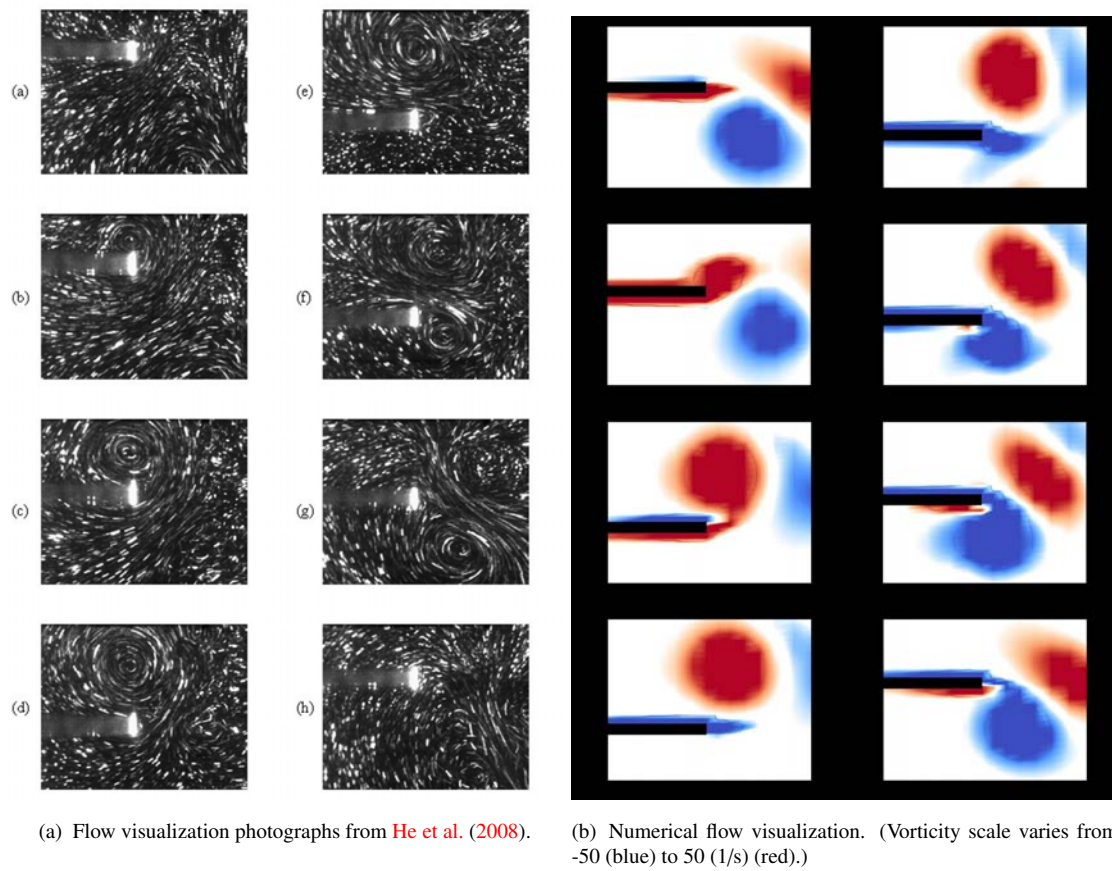


Fig. 4.8 Vortex generation around the disc edges at $KC = 0.16, t_d/D_d = 1/87.5$.

Chapter 5

Parametric dependence of hydrodynamic coefficients of a heave plate oscillating near a seabed or a free surface

5.1 Heave plate moving near a seabed

5.1.1 Introduction

This section is dedicated to the hydrodynamics of an oscillating heave plate close to the seabed. This problem is not directly related to the installations of floating offshore wind turbines, which is our main topic. However, it helps in understanding how the hydrodynamic of the heave plates is modified when getting closer to a fluid domain boundary. This boundary (the seabed) is theoretically simpler than the free surface (moving boundary) because it is fixed.

If a body is moving in a fluid close to other bodies (moving or not), then its added mass and damping differ from the added mass and damping corresponding to motion in an infinite fluid. This difference arises due to different boundary conditions: for an isolated body in an infinite fluid one has only a boundary condition (impenetrability) on the body surface and a boundary condition at infinity. In the presence of other bodies one should also impose boundary conditions on their surfaces.

In some offshore applications such as deployment of foundation templates and subsea structures, the penetration of a structure through the water surface and through the water column are important stages. Publications (Cermelli et al., 2003; Roveri et al., 1996) discuss the loads on the crane wire during deployment of a subsea equipment. More recently, Thurston et al. (2011) have discussed simplified mathematical models for statistical estimates of slack

and snap loads on the crane wire, due to sudden changes in the net load on the wire. This typically happens when the difference between the hydrostatic and hydrodynamic loads changes sign, i.e. crosses the zero value. The hydrodynamic load is strongly dependent on the hydrodynamic coefficients of the structure being deployed. It is well-known that hydrodynamic properties get altered significantly in the presence of a surface, hence requiring the use of the method of images. Other studies, summarized in [Sumer and Fredsøe \(1997\)](#), on flow past pipelines on a seabed reveals that the vortex street formation is altered significantly by the presence of a seabed. The Strouhal number is increased when a cylinder is close to a surface, and the effect of the wall is negligible at about 1.5 diameters.

A practical application of such a situation is the motion of a heave plate near a seabed. In this work the seabed was simulated as a solid wall. The numerical results are compared with the experiments conducted by [Wadhwa et al. \(2010\)](#).

5.1.2 Case study description

Forced numerical oscillations have been conducted in order to investigate the heave response of a solid disc. The disc is oscillated at varying distances from the seabed (see Fig. 5.1) and different amplitudes are applied, represented by the Keulegan-Carpenter parameter KC , as shown in Table 5.1. The Reynolds number range used is also documented.

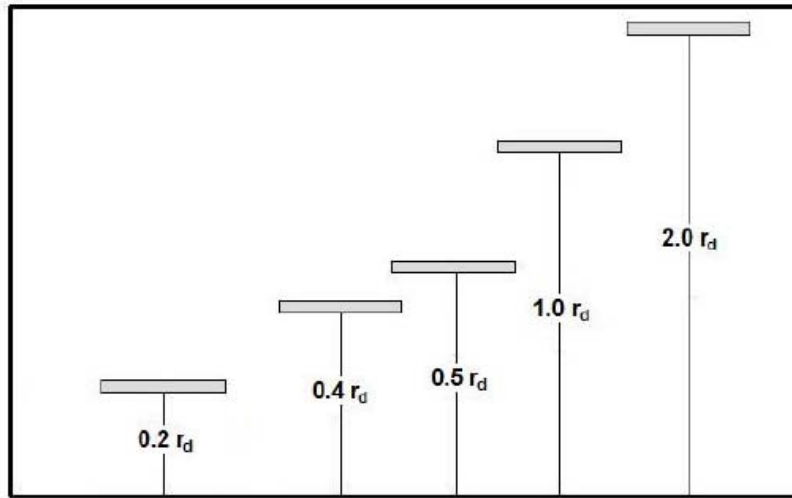


Fig. 5.1 Disc elevation (h) from the seabed. r_d is disc radius.

Fig. 5.2 shows the domain characteristics and the boundary conditions imposed for the case when the heave plate is oscillating near seabed. It is important to note that the seabed in our simulations is impermeable, and that the simulations considered the flow as laminar, hence no turbulence model was used.

Table 5.1 Parameters of simulations for heave plate oscillating near a seabed.

Water depth	0.84 m
Amplitude of oscillation	1 mm – 48 mm
Frequency of oscillation	1 Hz
Elevation from seabed h	$0.2 r_d - 2.0 r_d$
Diameter of the disc	200 mm
Thickness of the disc	2 mm
KC	0.03 – 1.5
Frequency parameter β	40000
Reynolds number Re	1200 – 60000

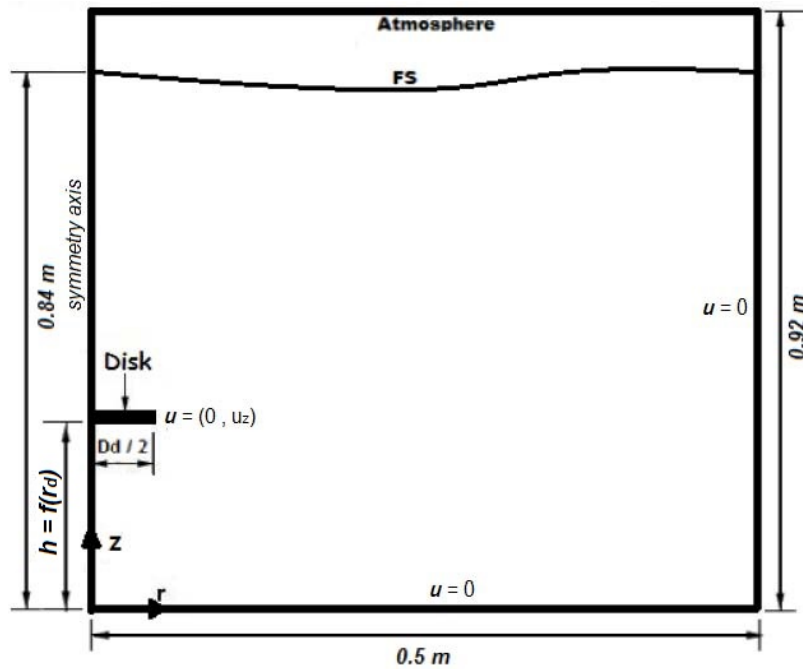
**Fig. 5.2** Tank geometry, flow domain and boundary conditions.

Fig. 5.3 shows tank used by [Wadhwa et al. \(2010\)](#) for their experimental setup. Their study suggests that as a structure moves closer to the mean seabed the added mass and damping coefficients increase monotonically and the slope of the added mass curve decreases with increasing proximity to seabed. This perhaps gives an idea of what can happen near the seabed, i.e. continuous variation of hydrodynamic forces due to proximity with a surface.

The objective of this chapter is to investigate the behavior of damping and added mass coefficients with various elevations of an object such as a disc from the seabed.

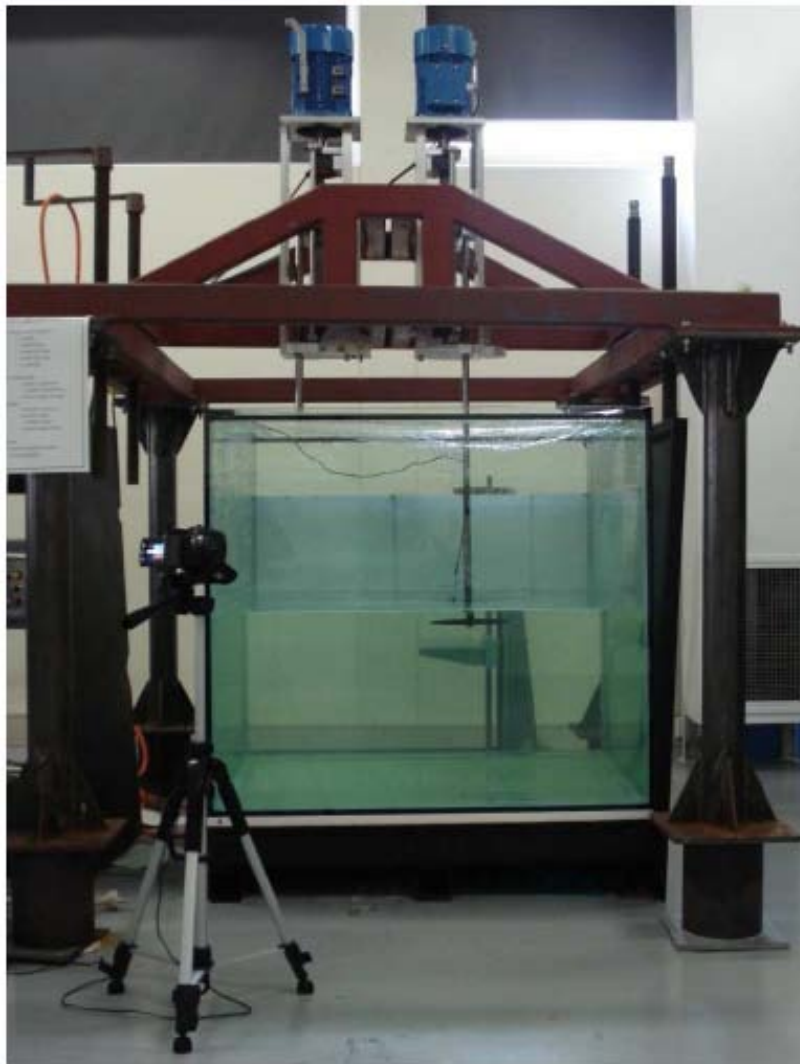


Fig. 5.3 Experiment set up in experiments conducted by [Wadhwa et al. \(2010\)](#).

5.1.3 Mesh generation

Due to the axisymmetric flow assumption, meshes for the simulation of the flow induced by the oscillating vertical cylinder are generated in a $2D$ region. The geometrical characteristics of the analyzed moving body (cylinder + heave plate) allow us to use quadrilateral structured meshes, which facilitate the convergence analysis.

Since the amplitudes of oscillations are relatively small, the vortex patterns around the cylinder are expected to depend only on the local flow around the sharp edge of the heave plate, flaps and holes.

The small regions around these elements, where the vortices are generated and shed during the oscillation, are resolved with more resolution by clustering the grid points in these

regions. Such a grid distribution ensures both high quality computation in the vicinity of sharp edge and global efficiency.

The free surface was also refined, but the mesh near to the free surface does not need mesh size as small as near the heave plate.

As can be seen in Fig. 5.4, the grid is fully orthogonal and the small regions around the sharp edge of the disc where the vortices are generated and shed during the oscillation, are resolved with more resolution by clustering the grid points in these regions. Such a grid distribution ensures both high quality computation in the vicinity of sharp edge and global efficiency.

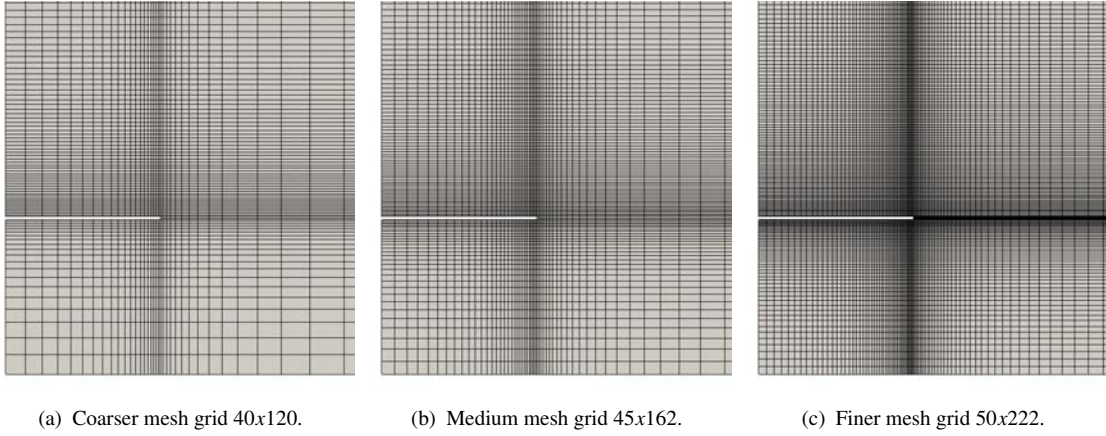


Fig. 5.4 Axisymmetric meshes used in the convergence analysis.

5.1.4 Convergence analysis

5.1.4.1 General

In order to rely on the accuracy of a numerical solution, convergence, as the mesh size and time step go to zero, has to be studied through different numerical experiments.

Time step and mesh size are linked by stability considerations. More specifically, in the scheme used, it has to be guaranteed that the CFL has to be smaller than one, with:

$$CFL = \frac{u\Delta t}{\Delta z} < 1. \quad (5.1)$$

This inequality, in which u is the velocity at the cell barycenter, has to be true for each cell. Convergence analysis will be conducted on a solid heave plate. It will be assumed that the parameters which allow us to find reasonable convergence for this case will be also valid for

the rest of simulations. The rationale behind this hypothesis is that the flow characteristics are similar as well as the forces and integral quantities.

The parameter to check convergence will be the drag coefficient C_d , that is obtained from a force time history by Fourier analysis (Sarpkaya and Isaacson, 1981):

$$C_d = -\frac{3\omega_{osc}}{4\rho S A^2 \omega_{osc}^2} \int_0^T F(t) \cos(\omega_{osc} t) dt, \quad (5.2)$$

where S is the projected area of the heave plate in the direction of the flow.

5.1.4.2 Convergence in mesh size

5.1.4.2.1 General. The numerical results of force and drag coefficient, obtained from different meshes for $KC = 1.0$, $\beta = 40000$ and $\Delta t = 1e^{-4}s$ are presented in Fig. 5.5. It has been checked that $CFL < 1$ with this Δt for all cases analyzed.

The details of the corresponding mesh parameters are listed in Table 5.2.

Table 5.2 Test cases for the influence of the meshes.

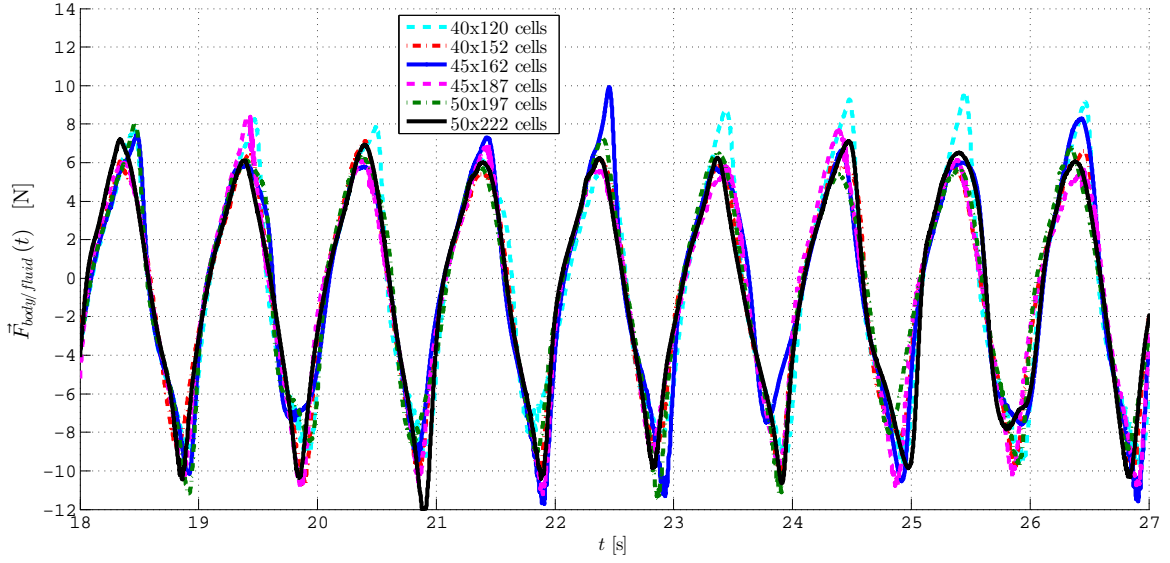
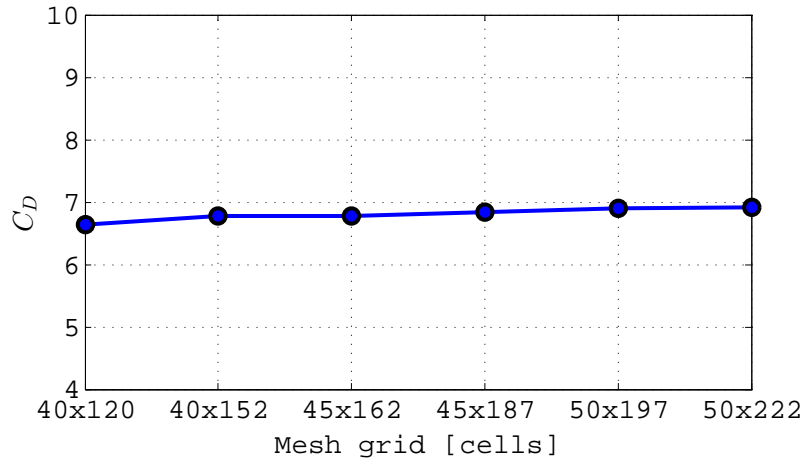
	Mesh	Total number of cells
Coarser mesh	40 x 120	4800
Coarser-Medium mesh	40 x 152	6080
Medium mesh	45 x 162	7290
Medium-Finer mesh	45 x 187	8415
Finer mesh	50 x 197	9850
Much Finer mesh	50 x 222	11100

Fig. 5.5 shows graphs that represent the force history and drag coefficient (Eqn. (5.2)) calculated for the different mesh grid.

As can be seen in the Fig. 5.5(a), the force amplitudes converge quickly. The finest mesh seems to present a smoother shape which is related with a force more concentrated in the frequency of the motion. Fig. 5.5(b) shows good convergence results when the mesh grid increases.

5.1.4.2.2 Near wall treatment. Near-wall regions, where boundary layers occur, present larger gradients in the solution variables, and momentum and other scalar transports occur most vigorously. These regions are made up of three zones (with their corresponding wall y^+) (Salim and Cheah, 2009), namely the:

- Viscous sublayer ($y^+ < 5$)

(a) Force history convergence with $\Delta t = 1e^{-4}$.(b) Drag coefficient convergence with $\Delta t = 1e^{-4}$ using Eqn. (5.2).**Fig. 5.5** Convergence tests in mesh sizes for $h/r_d = 2.0$ and $KC = 1.0$.

- Buffer layer or blending region ($5 < y^+ < 30$)
- Fully turbulent or log-law region ($y^+ > 30$ to 60)

The non-dimensional wall distance for a wall-bounded flow y^+ can be defined in the following way:

$$y^+ = \frac{u_* y}{\nu}; \quad (5.3)$$

where u_* is the friction velocity at the nearest wall, y is the distance to the nearest wall and ν is the local kinematic viscosity of the fluid.

For the finest mesh the computational y^+ value, based on the cell size was approximately 4.5, being within the viscous layer. It is in general recommended to have $y^+ < 1$. In our case not enough computational power is available to reach that limit. Nonetheless, as discussed in section 5.1.4.1, mesh convergence was reasonably good.

Other estimation is given by Batchelor (1967) and used by Tao and Dray (2008) in a similar context. Batchelor found that for a circular cylinder of infinite length oscillating along its axis in a still fluid, the boundary layer thickness is:

$$\delta = \sqrt{\frac{2\nu}{\omega}}. \quad (5.4)$$

This characteristic length is chosen as the base of the the mesh sensitivity test. To predict the skin friction accurately, the condition that $\Delta x_{min}/\delta < 0.3$ along the heave plate side surfaces is essential, which ensures that at least three mesh points are located in the boundary layer of cylinder side wall.

Again, for the test cases with $\beta = 40000$, the value of the boundary layer thickness is $\delta = 5.6419e^{-4}m$ and the minimum mesh spacing for all simulations was chosen as $2.5e^{-4}m$. It indicates that the meshes used in this work and the minimum mesh spacing around the heave plate are good enough for the treatment of near-wall regions.

Based on convergence tests, a mesh of 50×222 cells with a total number of cells equal to 11100 and minimum mesh spacing of $\Delta x_{min} = 2.5e^{-4}m$ was constructed in such a way that the node points are concentrated near the cylinder and disc surfaces and stretched out gradually.

5.1.4.3 Convergence in Δt

The choice of the time step to be used in the calculations is not straightforward. An important consideration is the accuracy of the schemes with which the governing equations are discretized in time. A smaller time step or, equivalently, a higher-order integration procedure increases this accuracy. Balanced against this is the of computational time, which increases and may lead the computation to be too expensive. Stability is in principle guaranteed on the basis of the *CFL* monitoring, as aforementioned.

In order to determine a suitable time step, a number calculations for different time steps are carried out. Fig. 5.6(a) shows a comparison between forces obtained for different time steps, while Fig. 5.6(b) shows that the lowest time step considered may be required for the accurate calculation of the drag coefficient.

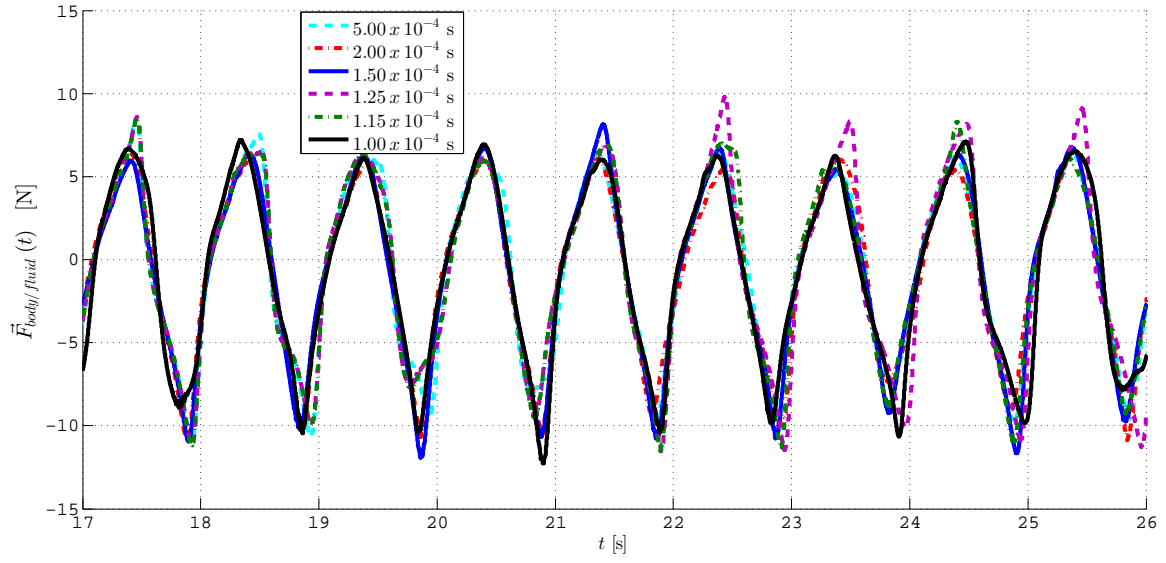
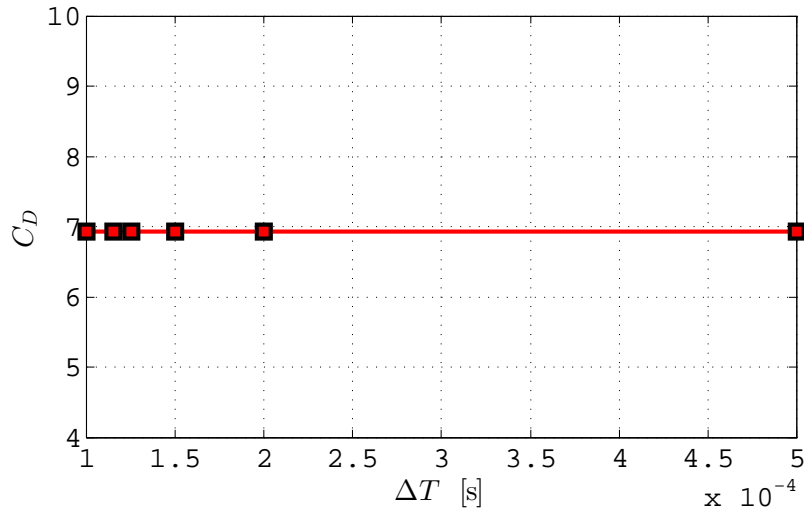
(a) Forces obtained for different time step at $KC = 1.0$ and 50×222 cells.(b) Drag coefficient time step convergence at $KC = 1.0$ and 50×222 cells using Eqn. (5.2).**Fig. 5.6** Convergence tests in Δt for $h/r_d = 2.0$ and $KC = 1.0$.

Figure 5.6(a) shows how the discrepancies are mainly concentrated in the sharp of forces and in the phase angle between them.

After this analysis, all the calculations were carried out with a mesh of 50×222 cells and a time step of $\Delta t = 1.0e^{-4}s$.

5.1.5 Results

5.1.5.1 General

In order to investigate the hydrodynamic coefficients of heave plates undergoing vertical oscillations, the results for hydrodynamic damping and added mass coefficients at $KC = 0.03 - 1.5$ and $f = 1 \text{ Hz}$ for a solid disc and different elevations of the disc from the seabed are discussed hereafter.

The discussion refers first to the values of the hydrodynamic coefficients. Once these aspects are covered, the flow patterns focusing on the vortex shedding mechanisms are treated. The relationship between the linear damping coefficient and the vorticity field through the enstrophy integral is also discussed.

5.1.5.2 Influence of flow parameter KC and elevation of the disc from the seabed

Figs. 5.7 and 5.8 show the variation of added mass and the damping coefficient, respectively, with KC , at different elevations, h , of the disc from the seabed. For each elevation, the coefficients display a linear trend until a certain critical value of KC is reached. A similar behaviour was also noticed in the experiments of Wadhwa et al. (2010). The slope of the curves increases as the disc is moved closer to the seabed. The added mass approaches its theoretical value when KC tends to zero for $h/r_d > 1.0$, as noticed in Fig. 5.7. As can also be appreciated in Fig. 5.7, the asymptotic value of C_a , as KC goes to zero, grows when the distance to the seabed is made smaller.

On the other hand, the damping coefficient C_b appears to converge, when KC goes to zero, irrespective of the seabed distance ratio h/r_d , (see Fig. 5.8).

Looking at the graphs of Figs. 5.7 and 5.8, it is clear that a critical KC number exists, above which the linear trend of hydrodynamic coefficients vs KC is broken. This critical KC can be related to h/r_d , as shown in Fig. 5.9. For values of h/r_d less than 1.0, including it, the law relating KC_{cri} to h/r_d is nearly linear with a slope close to one, suggesting that $KC_{cri} \simeq h/r_d$.

Above the critical KC , from preliminary computations, the behaviour of the coefficients was found not to follow a clear tendency, and its investigation has been therefore left for future work.

Fig. 5.10 shows the slope comparison of the added mass coefficient, between the present numerical data and the experimental data from Wadhwa et al. (2010). The figure shows a difference with experiments when the disc oscillates near to the seabed. This difference may be caused by the influence of the sandy bed when the disc is oscillating close to the seabed, resulting in a formation of cavities (Wadhwa et al., 2010), whereas in the simulations the

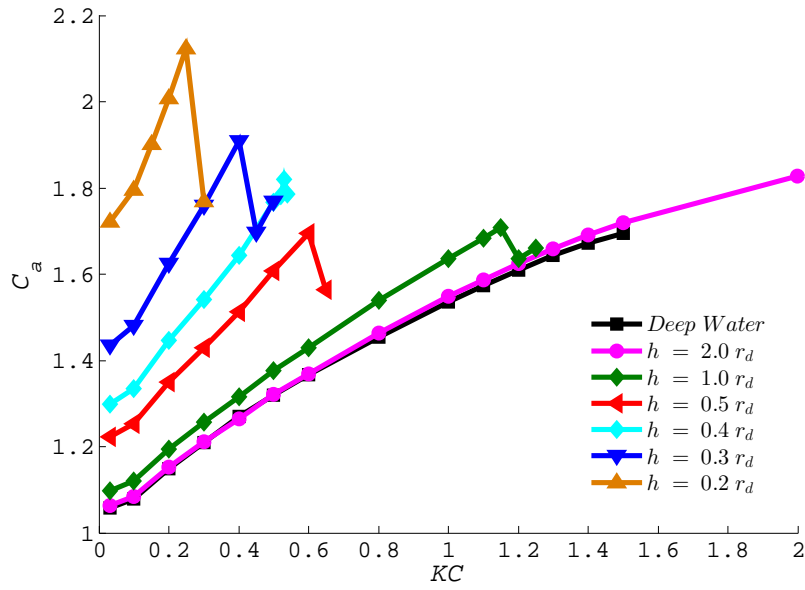


Fig. 5.7 Comparison of the added mass coefficient at different elevations from the seabed using Eqn. (4.46).

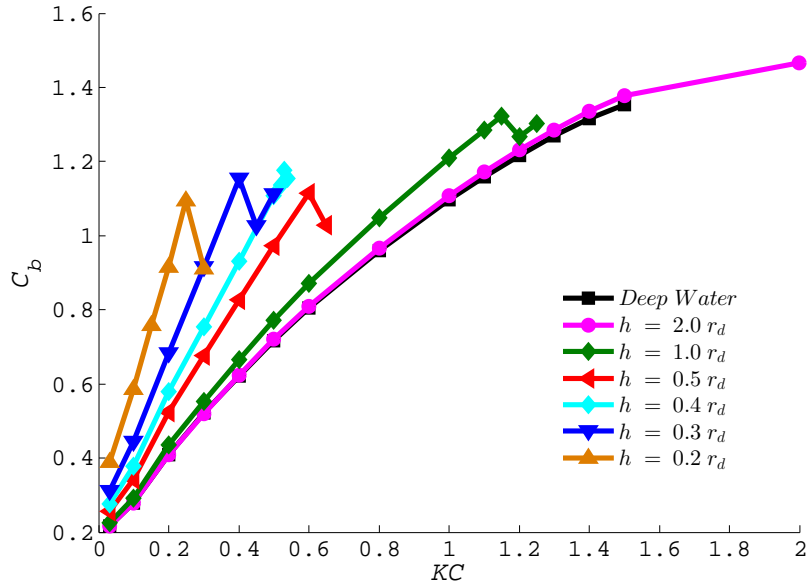


Fig. 5.8 Comparison of the damping coefficient at different elevations from the seabed using Eqn. (4.47).

seabed has been modeled as a fixed solid wall.

In order to describe the dependence of C_a and C_b coefficients with the submergence and KC number, the slope and offset of the least square linear fitting of such coefficients have been

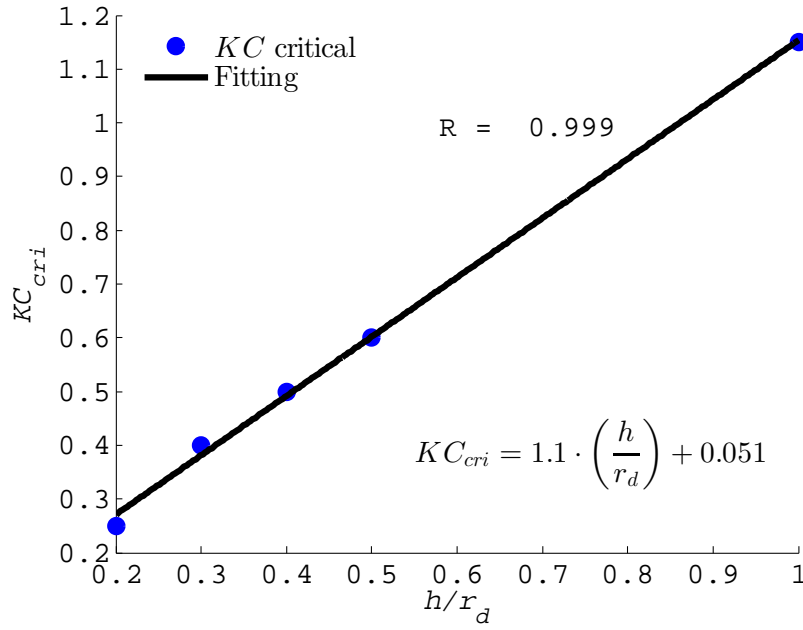


Fig. 5.9 Critical KC vs disc elevation from seabed.

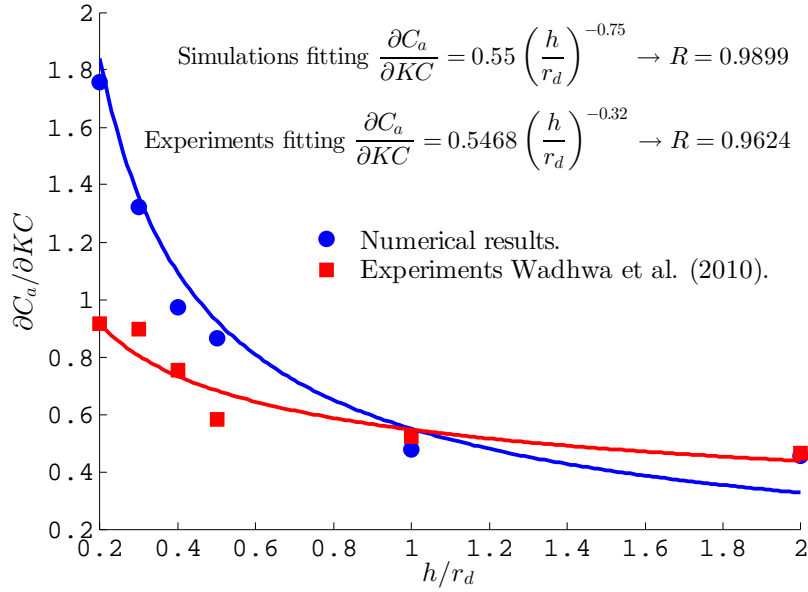


Fig. 5.10 Variation of $\partial C_d / \partial KC$ with disc elevation from seabed.

obtained. These two parameters (slope and offset) change quite dramatically for structures oscillating very close to the seabed and stabilize as the disc distance to the seabed increases. The values are summarized in Table 5.3. In general, the slope decreases continuously as the disc oscillates at larger elevations, h/r_d , from the seabed. A power regression analysis of the slope and offset data of the Table 5.3 allows one to express C_d and C_b in terms of h/r_d

for each KC value (see Eqn. (5.5) and (5.6)). These expressions can be used to evaluate the added mass and damping near the seabed for ' $h/r_d \leq 2$ '. For larger elevation ratios, deep water condition is seen to be the best fit. Fig. 5.11 and 5.12 show the comparison between the calculated coefficients and those fitted by Eqns. (5.5) and (5.6). The agreement is satisfactory.

Submergence h	C_a		C_b	
	Slope ($\partial C_a / \partial KC$)	Offset	Slope ($\partial C_b / \partial KC$)	Offset
$2.0 r_d$	0.47	1.06	0.82	0.22
$1.0 r_d$	0.56	1.10	1.00	0.23
$0.5 r_d$	0.85	1.22	1.53	0.26
$0.4 r_d$	1.01	1.30	1.80	0.28
$0.3 r_d$	1.32	1.43	2.30	0.31
$0.2 r_d$	1.87	1.72	3.23	0.39

Table 5.3 Slope and offset of curve fits for C_a and C_b .

$$C_a = 0.55 \left(\frac{h}{r_d} \right)^{-0.75} KC + \frac{0.10}{\frac{h}{r_d}} + 1; \quad (5.5)$$

$$C_b = 0.95 \left(\frac{h}{r_d} \right)^{-0.55} KC + \frac{0.02}{\frac{h}{r_d}} + 0.2; \quad (5.6)$$

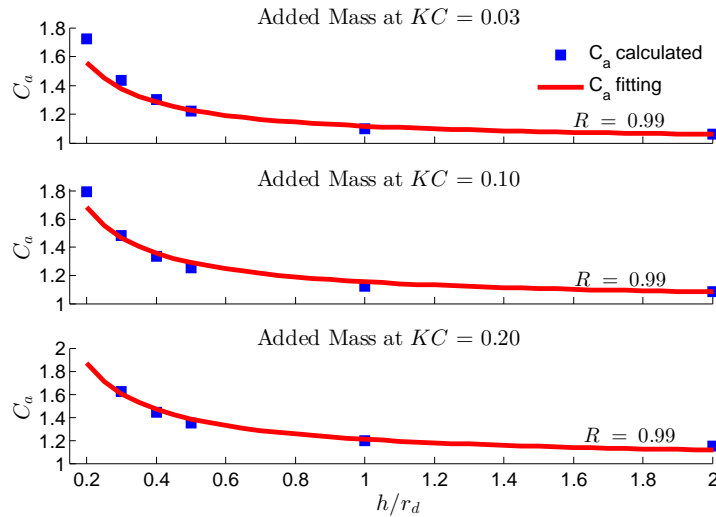


Fig. 5.11 Variation of C_a with disc elevation from seabed for different KC numbers.

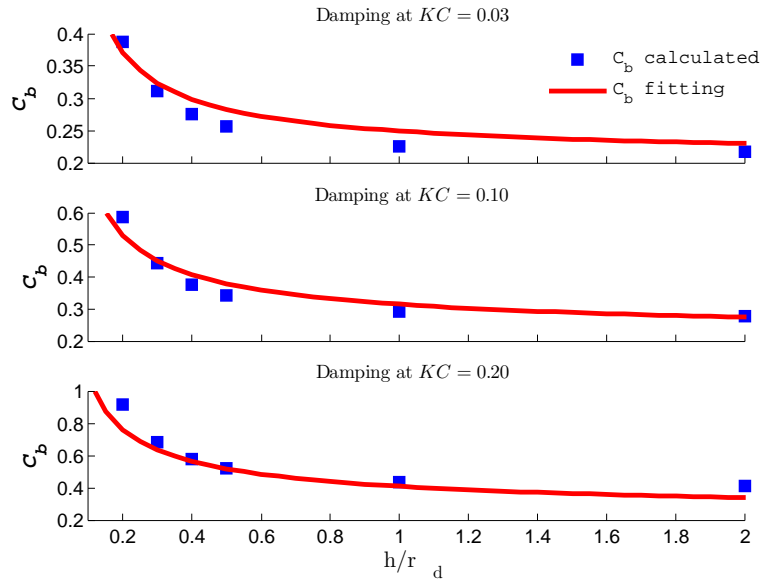


Fig. 5.12 Variation of C_b with disc elevation from seabed for different KC numbers.

In Fig. 5.13, the expression for C_a (Eqn. 5.5) has been compared with the results by [Molin and Nielsen \(2004\)](#) of potential flow around a porous oscillating disc, and with the widespread use frequency domain potential flow software WAMIT, displaying fairly good agreement. It has to be mentioned that [Molin et al. \(1999\)](#) and [Vinje \(2001\)](#) derived asymptotic expressions for the added mass of a disc oscillating close to a solid wall. However, such formulae present small discrepancies that need to be sorted out before using them for comparison. A future work thread about this topic has been included.

Results of added mass and damping coefficients (Figs. 5.7 and 5.8) can also be made non-dimensional with the aforementioned numerical values from WAMIT. With this non-dimensionalization, the offset difference between the curves is significantly reduced (see Figs. 5.14 and 5.15), indicating, that the numerical results follow the potential flow predictions. However, the ratios between the numerical results and the *WAMIT* values do not exactly tend to one for low KC values, something for which an explanation at this stage is yet missing. In these figures the KC values in the horizontal axis have been rescaled with the proposed asymptotic value for critical KC , $KC_{cri}^* := h/r_d$. It is interesting to see how, with this rescaling, the abscissae of the points, for which the linear trend is broken, coincide.

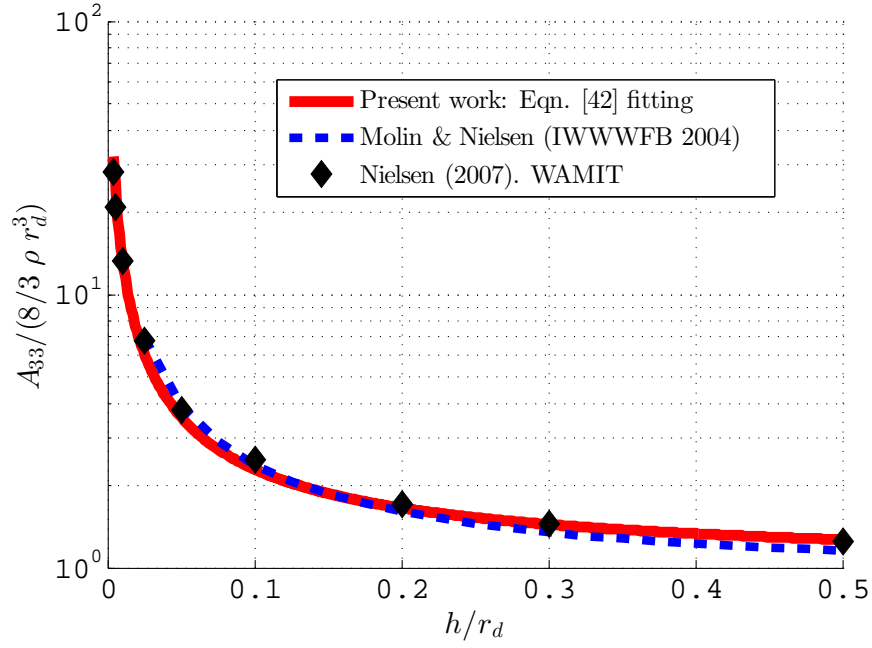


Fig. 5.13 Comparison of C_a between Eqn. (5.5), numerical values from WAMIT and analytical results of Molin and Nielsen (2004).

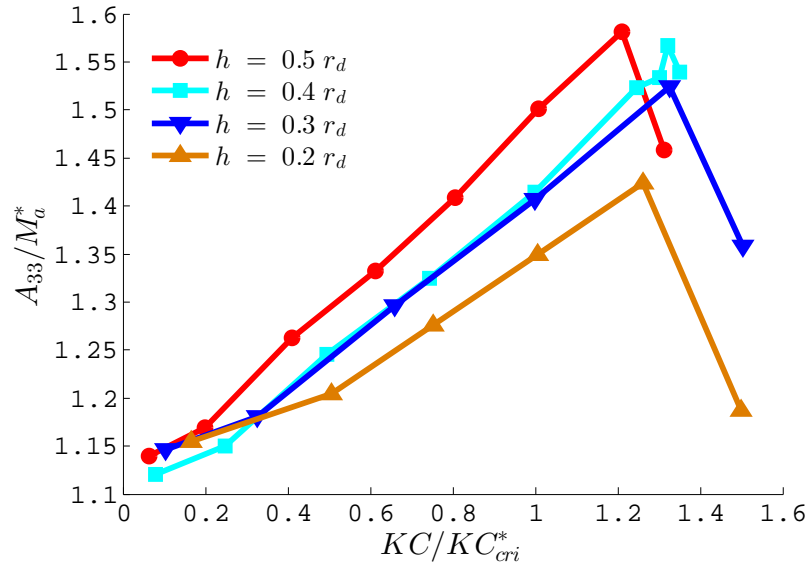


Fig. 5.14 Added mass coefficient for $h/r_d \leq 0.5$ non-dimensionalized with M_a^* , with M_a^* being the numerical value from WAMIT.

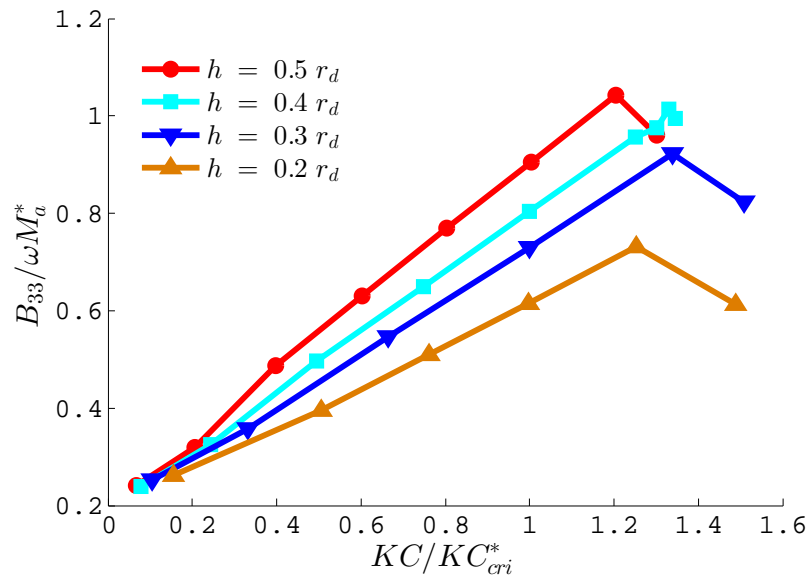


Fig. 5.15 Damping coefficient for $h/r_d \leq 0.5$ non-dimensionalized with ωM_a^* , with M_a^* being the numerical value from WAMIT.

5.1.5.3 Flow patterns analysis

5.1.5.3.1 General. Explanations for the behaviour of the hydrodynamic coefficients in proximity to the seabed ought to be obtained from examination of the flow features: while added mass modelling can be accurately achieved under the potential flow assumption (Molin et al., 1999), damping is more difficult to treat within that framework, although very relevant results for simple configurations can be obtained (e.g. Graham (1980)). The variation of damping is normally attributed to flow separation and vortex shedding, and full CFD analysis of the flow, is therefore, in principle, necessary to understand the damping properties of an oscillating body.

5.1.5.3.2 KC influence. Flow separation does not always result in vortex shedding (Faltinsen, 1990). With increasing KC number, the transition from separation without vortex shedding to separation with vortex shedding should be visible. Clearly, this will also affect the damping coefficient. When the KC number is small, the maximum displacement of particles in the undisturbed flow is small compared to the scale of the body. It is therefore unfeasible for vortices to move far from the edge of the body from which they are shed, except under the induced velocity field of other vortices.

Fig. 5.16 shows, in frames equally spaced over one cycle, the distributions of the vorticity, where red denotes positive values and blue means negative. Half disc is shown, with the bottom of each frame indicating the position of the tank bottom. This is also the case for all figures in this section.

Results are presented for increasing KC values in panels *a*, *b* and *c*. For low and intermediate KC numbers, as the disc begins the descent (frames *a*1, *b*1), a dominant positive vortex (red) is created (frames *a*2, *b*2), which pairs with the negative vortex (blue) (frames *a*3, *b*3) in the upstroke, resulting in shedding of the vortex pair (frames *a*4, *b*4). When the disc reaches the maximum absolute displacement, the flow separates from the disc surface causing vortex shedding. Fig. 5.16(c) shows the instantaneous vorticity contours obtained at a higher Keulegan-Carpenter number, $KC = 1.20$. With this highest KC , the strength of the vortices is much larger, due to the larger vorticity shed from the edges of the disc.

In order to understand the meaning of the KC critical value, an analysis of the vorticity contours for three cases with KC numbers just under, equal to, and just over the critical KC was conducted. When the disc is oscillating just above the KC critical value, Fig. 5.17(c), entrainment of vortices by the seafloor (shown in blue in frame 1 of Fig. 5.17(c)) from earlier cycles influences the shedding pattern and, thus, alters the force on the disc. In both Figs. 5.17(a) and 5.17(b), such intense entrainment does not occur.

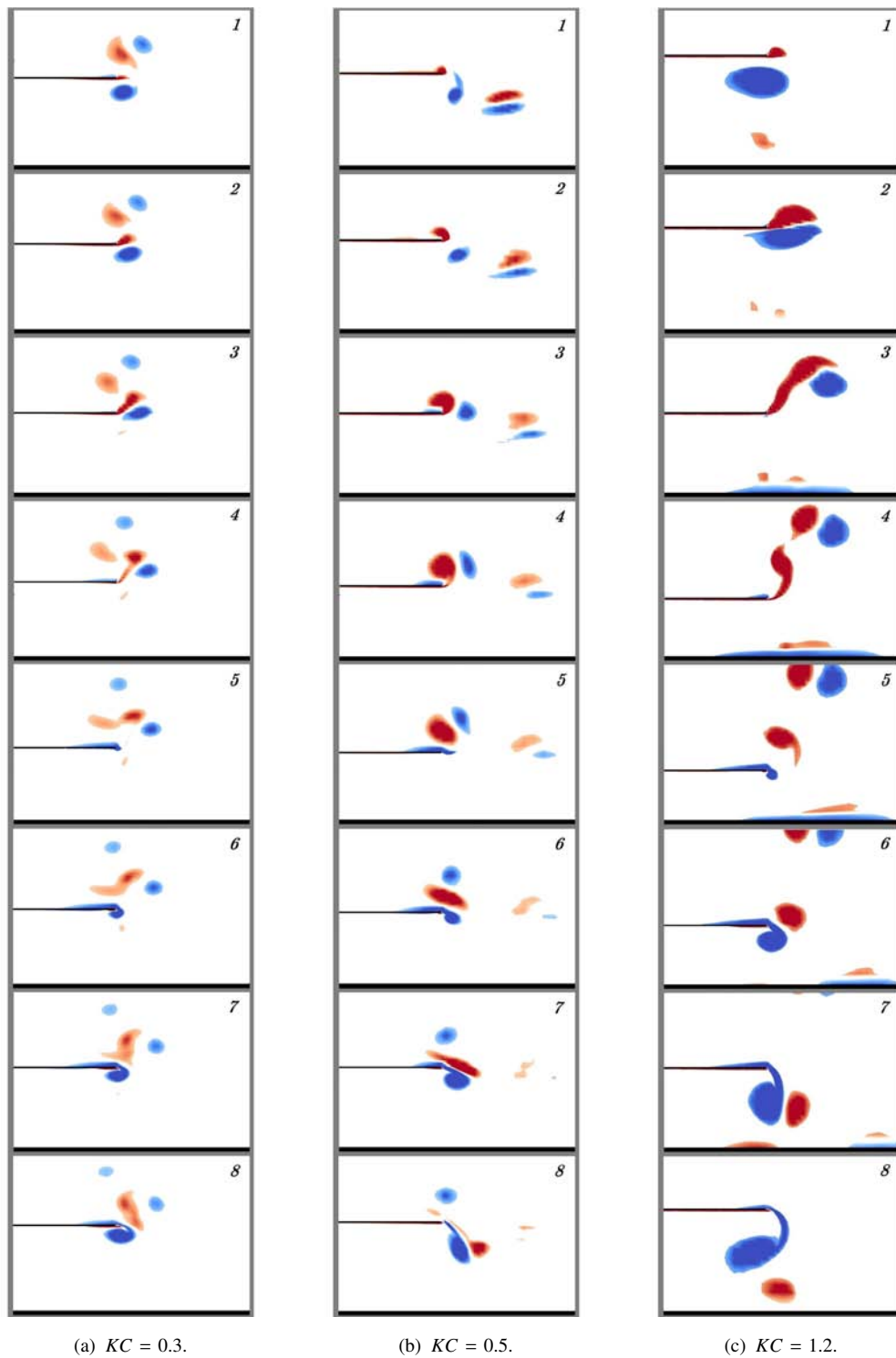
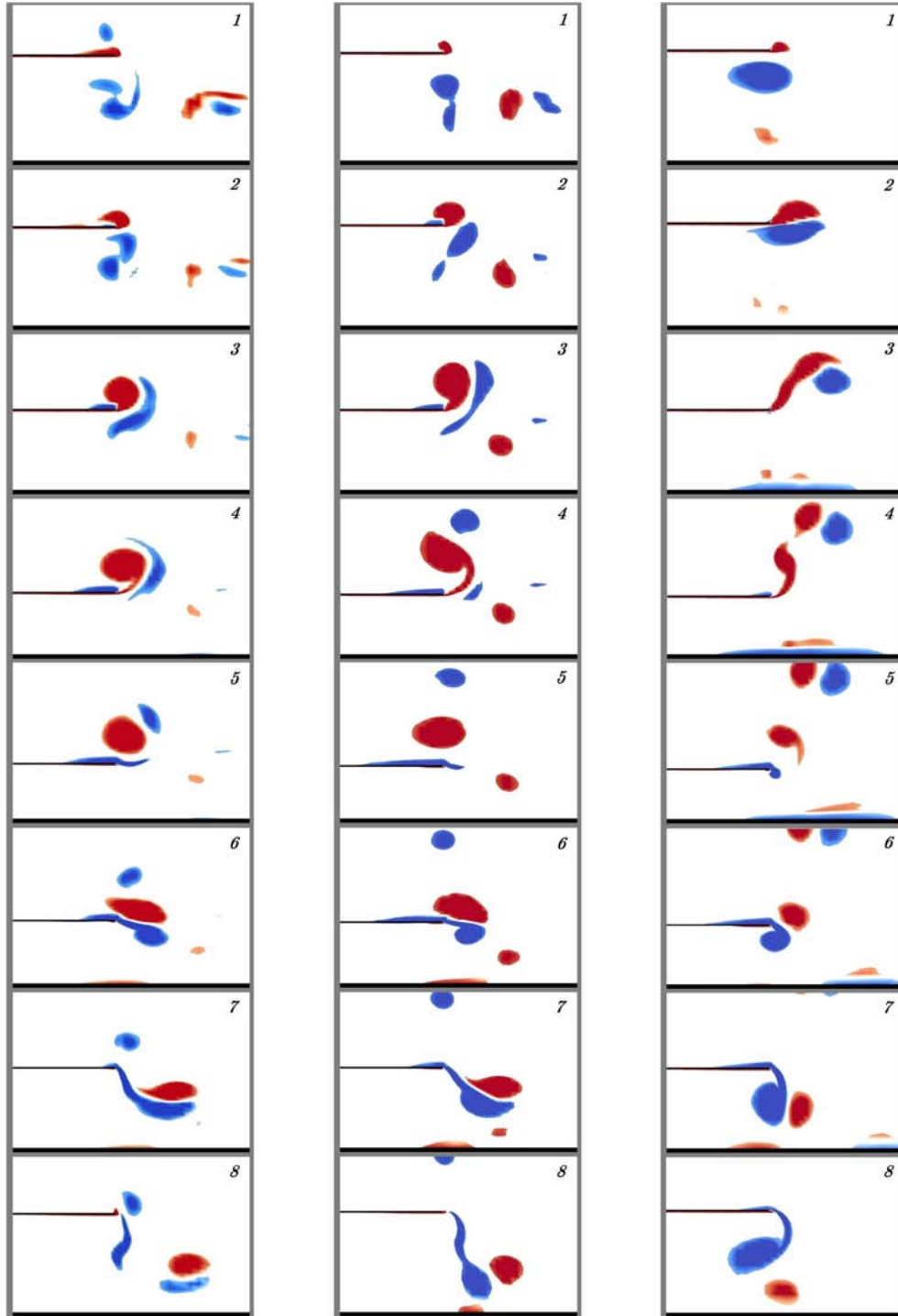


Fig. 5.16 Vortex generation around disc close to seabed at $h/r_d = 1.0$. (Vorticity scale varies from -25 s^{-1} (blue) to 25 s^{-1} (red).)



(a) Vortex generation around the disc at $KC/KC_{cri} = 0.96$.
 (b) Vortex generation around the disc at $KC/KC_{cri} = 1.00$.
 (c) Vortex generation around the disc at $KC/KC_{cri} = 1.04$.

Fig. 5.17 Vortex generation around the disc at $h/r_d = 1.0$. Blue lines indicate negative vorticity (initial condition: Top Dead Centre). Scale varies from -25 s^{-1} (blue) to 25 s^{-1} (red).

5.1.5.3.3 Influence of seabed distance ratio (h/r_d). It is expected that the vortex shedding behaviour will be strongly dependent on the h/r_d ratio.

Fig. 5.18 shows the vortex patterns at a constant KC for three different height to radius ratios. Fig. 5.18(a) shows that the intensity of the vortices increases when reducing the h/r_d ratio, i.e., as the disc mean position is closer to the seabed.

5.1.5.4 Enstrophy dissipation term analysis

5.1.5.4.1 KC influence. Fig. 5.19 and 5.20 show the time history of the enstrophy term (Eqn. 4.20) for different amplitudes of oscillation corresponding, to the cases in Fig. 5.16. Actually, in Fig. 5.19, some labels indicate the instants of the selected frames shown in Figure 5.16(c).

In order to make the curves comparable, Eqn. (4.27) shows that the enstrophy integral, $\dot{\mathcal{E}}_\omega$, is of the order of $\mathbf{F}_{body/fluid} \cdot \mathbf{v}_B(t)$, in itself of the order of $C_b \rho r_d^3 A^2 \omega^3$. The factor $\rho r_d^3 A^2 \omega^3$ has been therefore used to make $\dot{\mathcal{E}}_\omega$ non-dimensional, a choice which should allow to establish comparisons with C_b tendencies.

In order to estimate $B_{33\omega}$, these curves are integrated along one period, which means that the mean value is the crucial quantity. Such mean value is quite stable in time, as can be seen in Fig. 5.20. However, the ripples, whose rms amplitude is around 10% of the mean value, display a non-periodic behavior whose investigation has been left for future work.

Looking at Figs. 5.19 and 5.20, it is clear that the mean values of the non-dimensional enstrophy integral grows with KC number, an aspect which is consistent with the growth of C_b with KC (see Fig. 5.8).

Figs. 5.21 and 5.22 show the time history of the enstrophy term at $h/r_d = 1$ for KC s close to the KC critical value. There is a clear variation in the behaviour of the curves when the disc exceeds the critical value of KC , dissipating less energy, thus confirming the existence of an amplitude in which the linear trend of the hydrodynamic coefficients is broken (see Figs. 5.7 and 5.8).

5.1.5.4.2 Influence of seabed distance ratio (h/r_d). It is also important to analyze the effect that the seabed has on the dissipation term $\dot{\mathcal{E}}_\omega$. Figs. 5.23 and 5.24 show the enstrophy integral for different elevation ratios. They heuristically demonstrate that, in non-dimensional terms, the energy dissipation is larger when the elevation ratio, h/r_d , is smaller, consistently with the C_b values shown in Fig. 5.8. This helps in clarifying the influence, on the hydrodynamic coefficients, of the distance between the disc and the seabed.

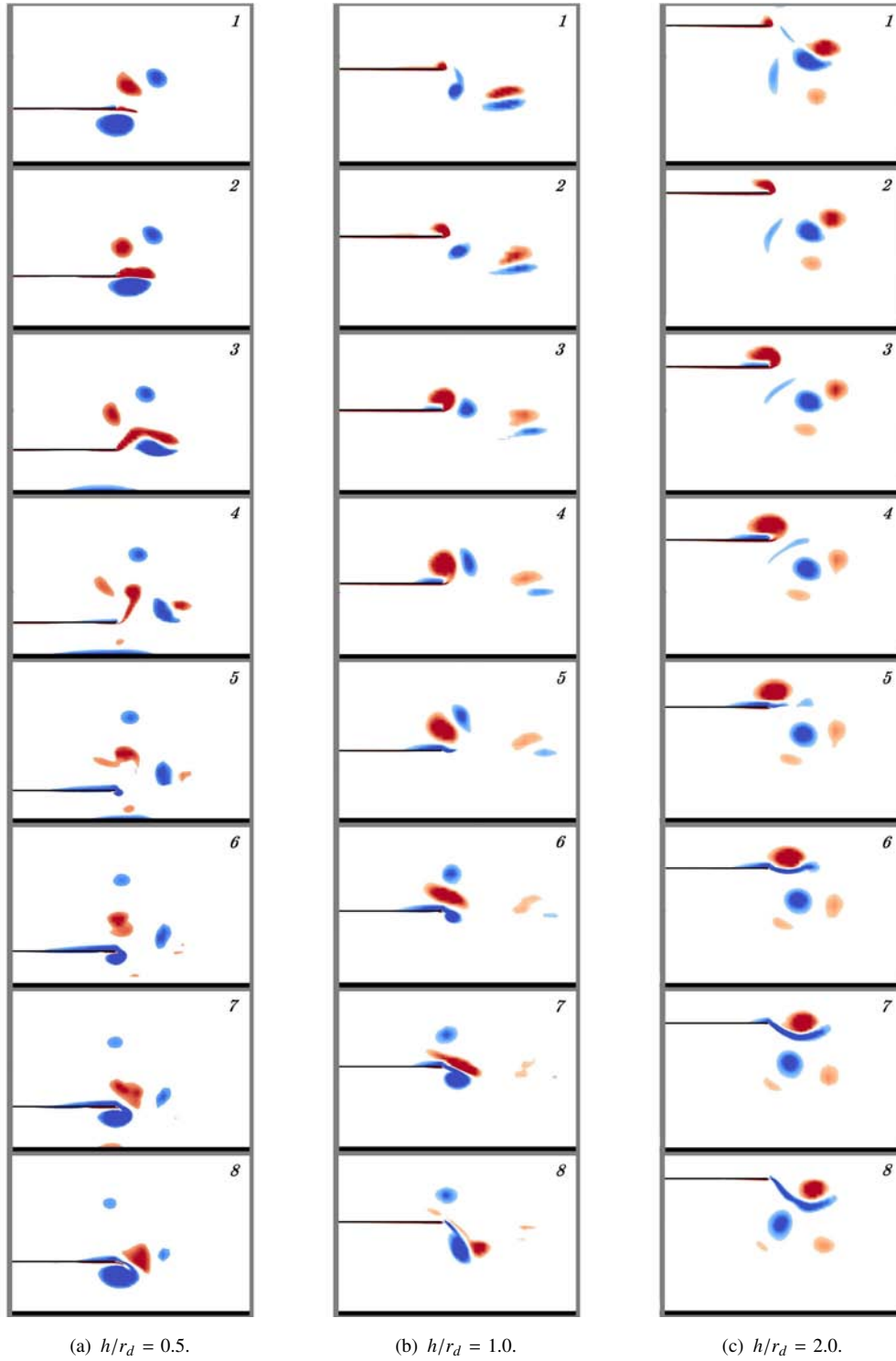


Fig. 5.18 Vortex generation around the disc close to the seabed at $KC = 0.5$. (Scale varies from -25 s^{-1} (blue) to 25 s^{-1} (red).)

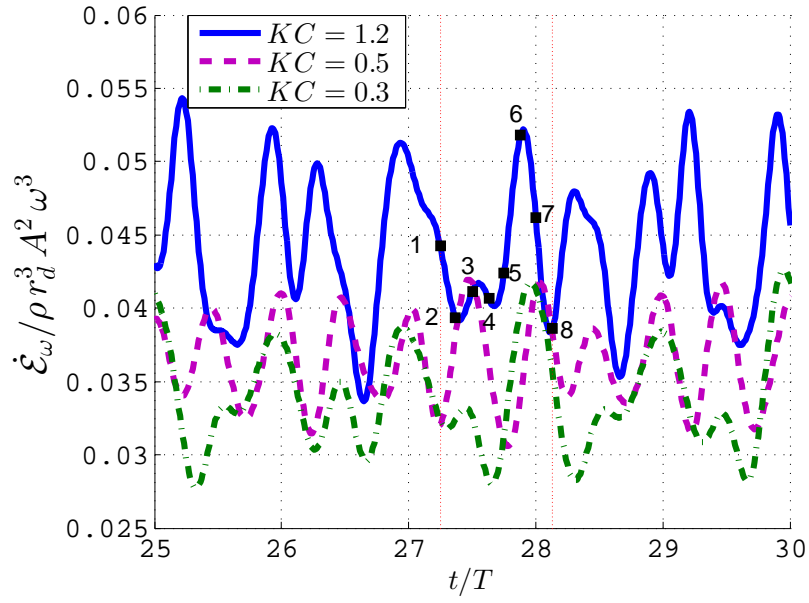


Fig. 5.19 Time history of the enstrophy term from Eqn. (4.20) for an oscillating disc close to the seabed for different KC values at $h/r_d = 1.0$. Markers correspond to the frames depicted in Fig. 5.16.

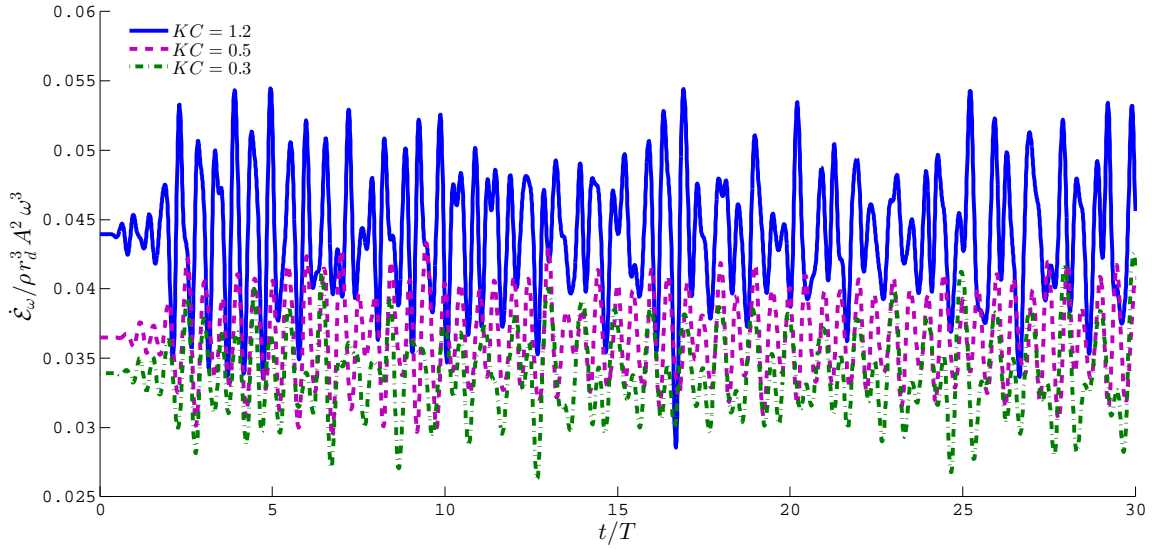


Fig. 5.20 Time history of the enstrophy term from Eqn. (4.20) for an oscillating disc close to the seabed for different KC values at $h/r_d = 1.0$.

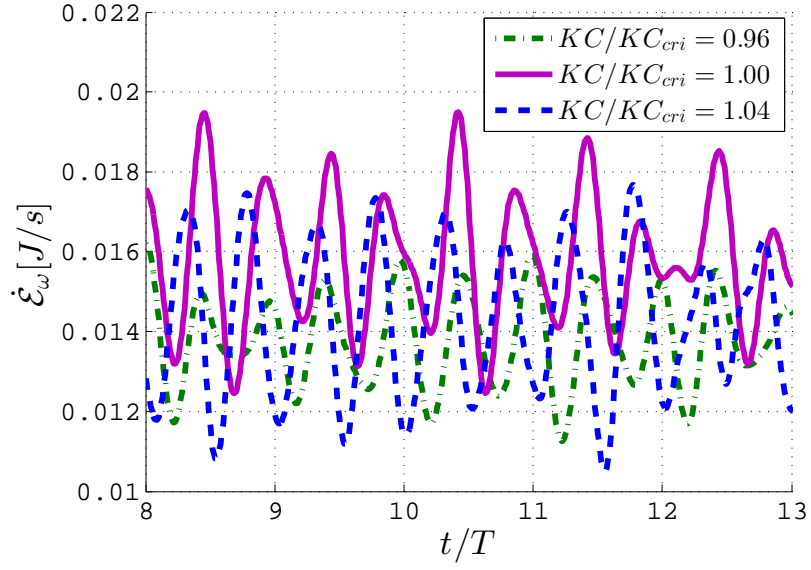


Fig. 5.21 Time history of the enstrophy term from Eqn. (4.20) for an oscillating disc close to the seabed at $h/r_d = 1.0$ around critical KC value. See Figs. 5.8 and 5.17 for $h/r_d = 1.0$.

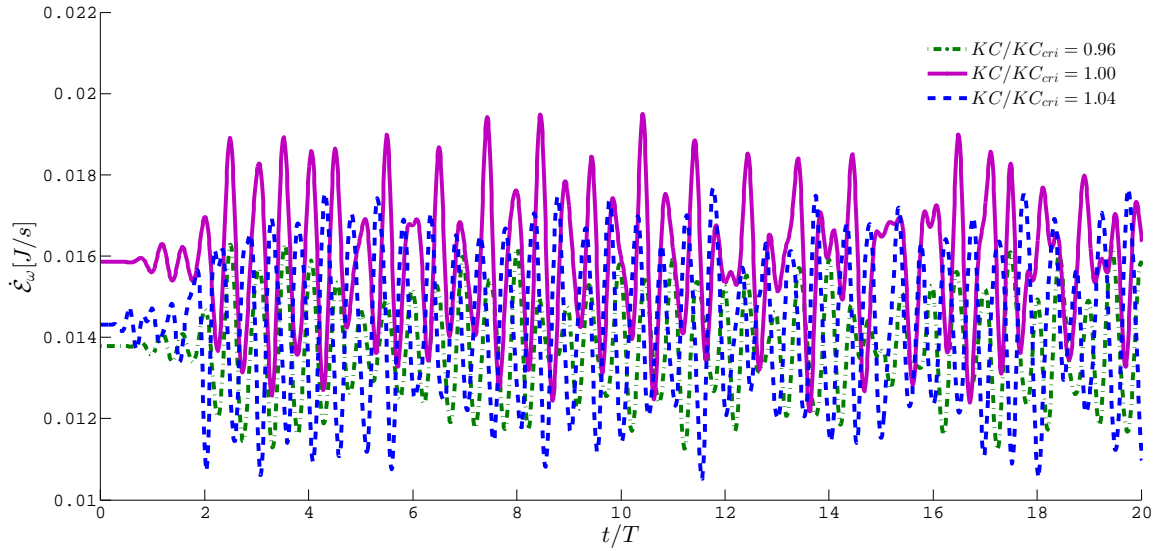


Fig. 5.22 Time history of the enstrophy term from Eqn. (4.20) for an oscillating disc close to the seabed at $h/r_d = 1.0$ around critical KC value.

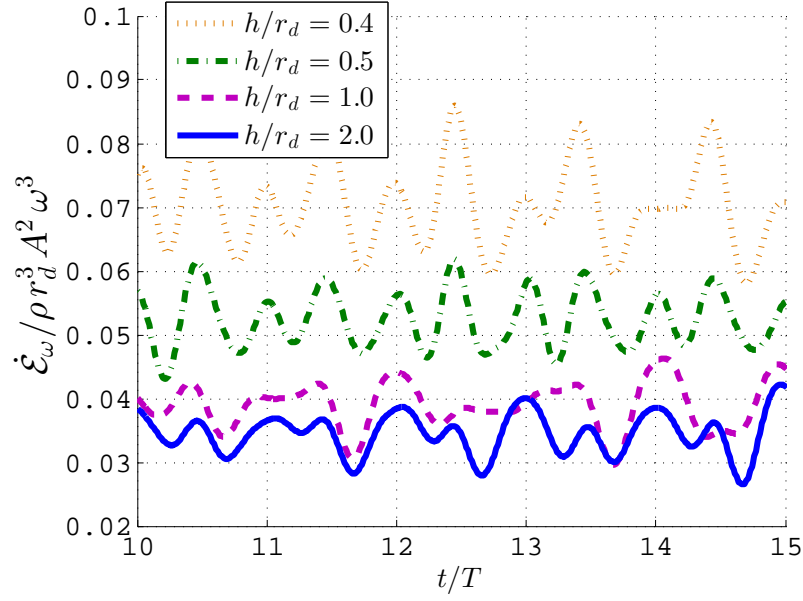


Fig. 5.23 Time history of the enstrophy term from Eqn. (4.20) for an oscillating disc close to the seabed for different h/r_d values at $KC = 0.4$.

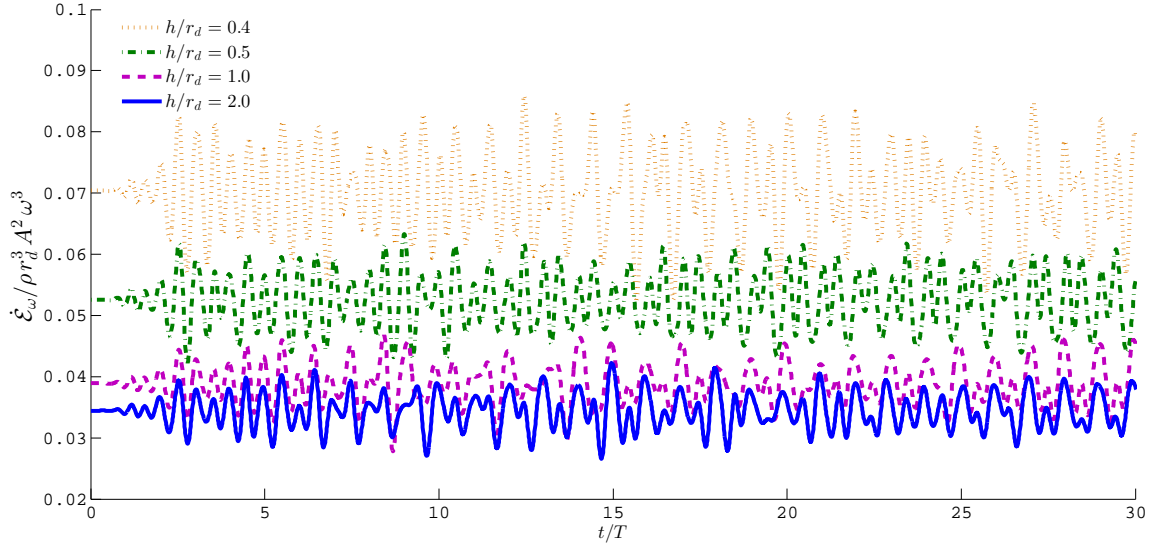


Fig. 5.24 Time history of the enstrophy term from Eqn. (4.20) for an oscillating disc close to the seabed for different h/r_d values at $KC = 0.4$.

5.1.5.4.3 Comparison between B_{33} and $B_{33\omega}$. The relationship between the damping coefficient $B_{33\omega}$ obtained through the enstrophy integral (Eqn. 4.39) and the damping coefficient obtained with the classical forces projection approach (Eqn. 4.37), are discussed hereinafter. Figs. 5.25 – 5.27 show the comparison of the damping coefficient obtained with both approaches for three representative cases. The matching is, in general, very good. This indicates that the enstrophy contribution to the dissipation $\dot{\mathcal{E}}_\omega$ may be the lead actor in this type of flows.

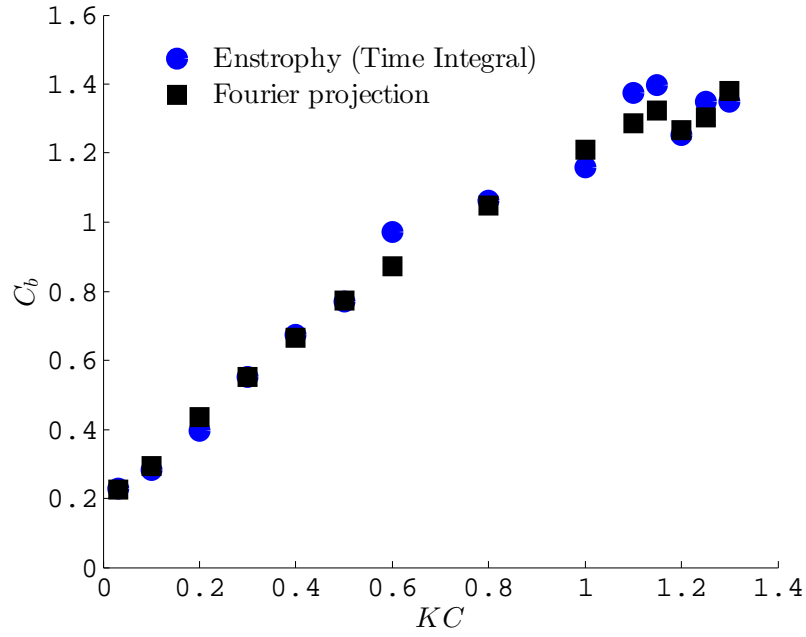


Fig. 5.25 Comparison of hydrodynamic damping coefficient (C_b) with B_{33} at $h/r_d = 1.0$, obtained with the enstrophy integral (Eqn. (4.39)) and classical (Sarpkaya and Isaacson, 1981) Fourier projection (Eqn. (4.47)), for an oscillating heave plate near a seabed.

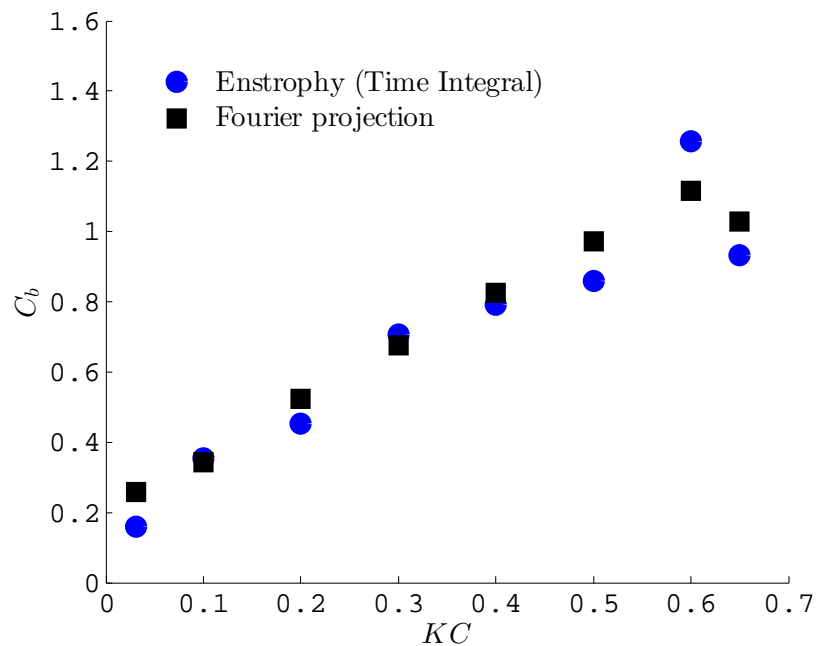


Fig. 5.26 Comparison of hydrodynamic damping coefficient (C_b) with B_{33} at $h/r_d = 0.5$, obtained with the enstrophy integral (Eqn. (4.39)) and classical (Sarpkaya and Isaacson, 1981) Fourier projection (Eqn. (4.47)), for an oscillating heave plate near a seabed.

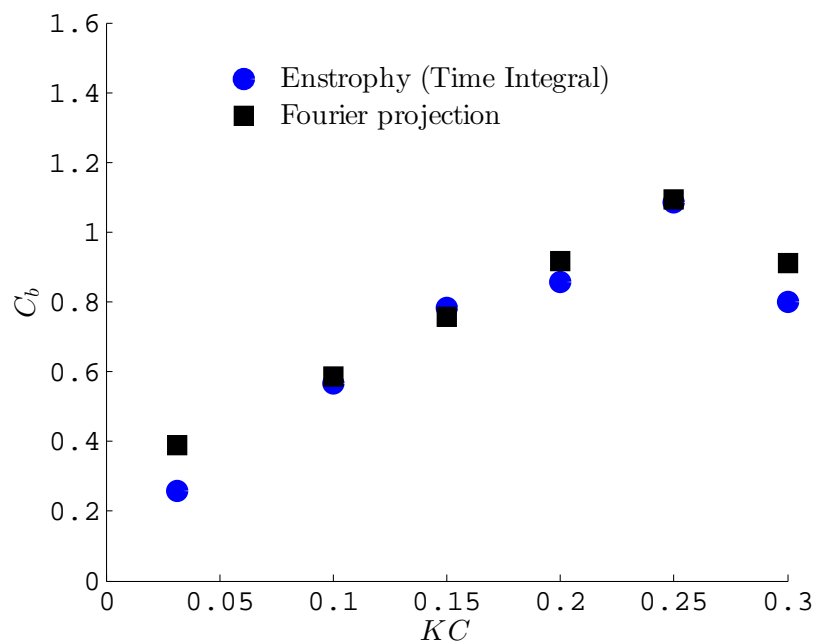


Fig. 5.27 Comparison of hydrodynamic damping coefficient (C_b) with B_{33} at $h/r_d = 0.2$, obtained with the enstrophy integral (Eqn. (4.39)) and classical (Sarpkaya and Isaacson, 1981) Fourier projection (Eqn. (4.47)), for an oscillating heave plate near a seabed.

5.2 Heave plate oscillating close to a free surface

5.2.1 Introduction

This section will study the hydrodynamic forces of the submerged heave plate oscillating near a free surface, and unlike the presence of a solid boundary (5.1), a free surface boundary increase considerably to the complexity of the problem.

The flow induced by a body oscillating near a free surface of a fluid is significantly different from that of an infinite fluid. The difference is due to the presence of a boundary condition (constancy of pressure) on the free surface. The free surface effect can strongly influence the added mass and damping coefficient values as a function of the frequency when the submerged body oscillates near a free surface (Chung, 1977). Also the flow is highly non-linear even at very small amplitude of oscillation, when the body is slightly submerged.

Any prior rotational or translational motion of those bodies would have generated free surface waves which would in turn affect the loading on the body. This represents the major complication introduced by the presence of a free surface. It is however clear that if the body motion is sufficiently slow (characterized by a velocity, U say), then the waves created will be negligibly small and these prior history effects would also be small (Brennen, 1982).

5.2.2 Case study description

Figure 5.28 shows the simulation setup and boundary conditions used in all cases in this section. The no-flux and no-slip velocity boundary conditions are imposed along the oscillatory body surface. The heave plates were forced to oscillate harmonically in a vertical direction in quiescent water.

The parameters for the simulations used in this section were listed in Table 5.1.

5.2.3 Mesh generation

A brief description of the mesh characteristics used in this case study is presented in Figure 5.29. Mesh distribution and minimum cell size around the disc is the same to the mesh and parameters used in section 5.1.3. Here the refining of the free surface is also shown.

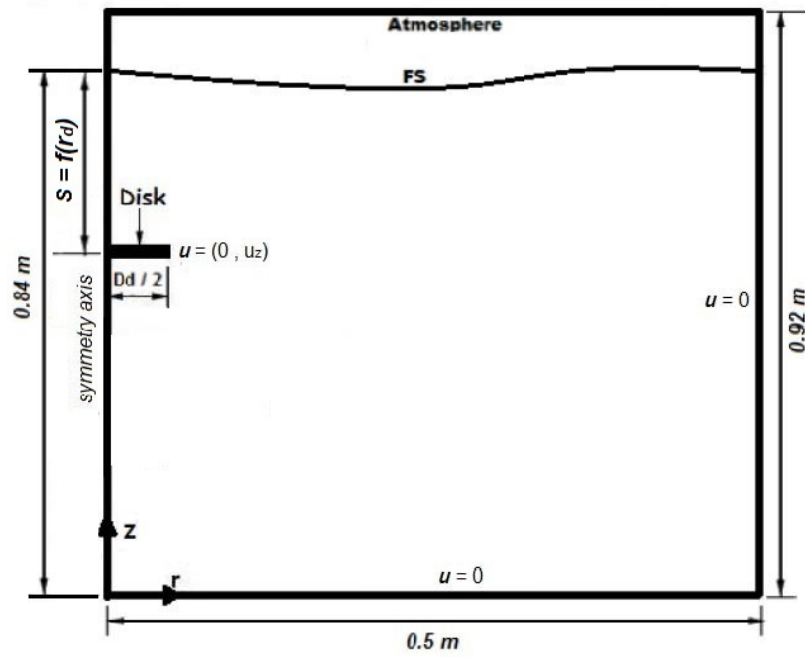


Fig. 5.28 Disc submergence (s) from the free surface. r_d is disc radius.

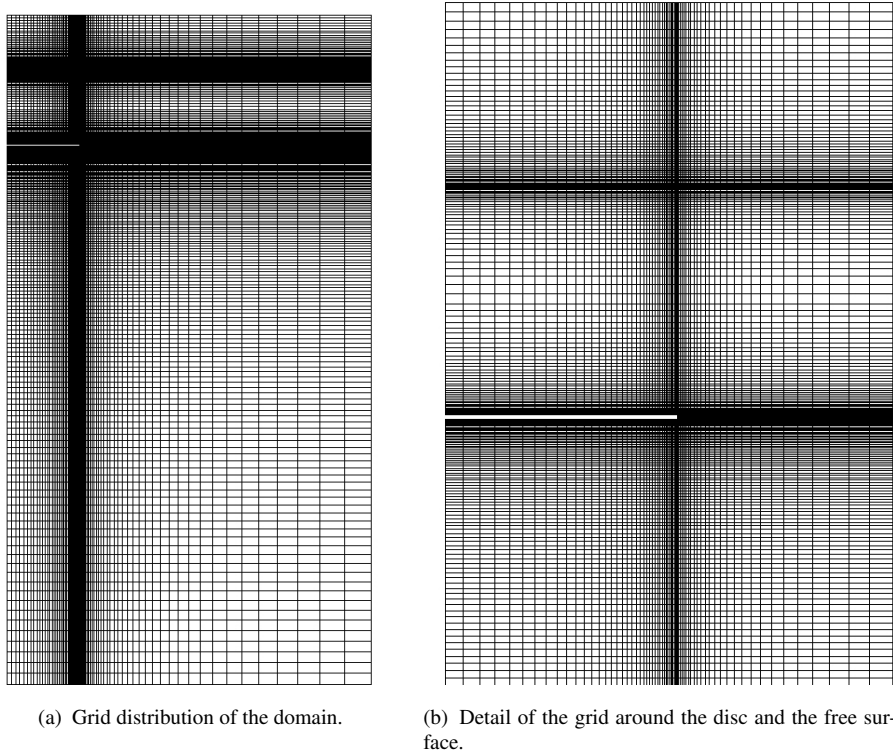


Fig. 5.29 Axisymmetric mesh used for the disc oscillating close to the free surface cases.

5.2.4 Results

5.2.4.1 General

Similar to the previous case (heave plates oscillating close to the sea-floor), the hydrodynamic coefficients of a heave plate oscillating in vertical direction at different submergence from the free surface are discussed hereafter.

The results section refers first to the dependence of the hydrodynamic coefficients with the amplitude of the motion and the submergence ratio. Then, vorticity and free-surface visualization is made in order to understand the flow features. Finally, the relationship between the linear damping coefficient and the dissipation terms, \dot{E}_ω and \dot{E}_{FS} , (Eqn. 4.20 and 4.21), enstrophy and free surface dissipation, respectively, is discussed.

5.2.4.2 Influence of flow parameter KC and submergence of the disc from the free surface

Figures 5.30 and 5.31 show the influence on the added mass and damping when the heave plate is oscillating close to the free surface. As can be seen, the added mass first increases at the acceleration of the fluid between the free surface and the body increases, but then decreases when the depth is less than about one body dimension because less fluid is being accelerated.

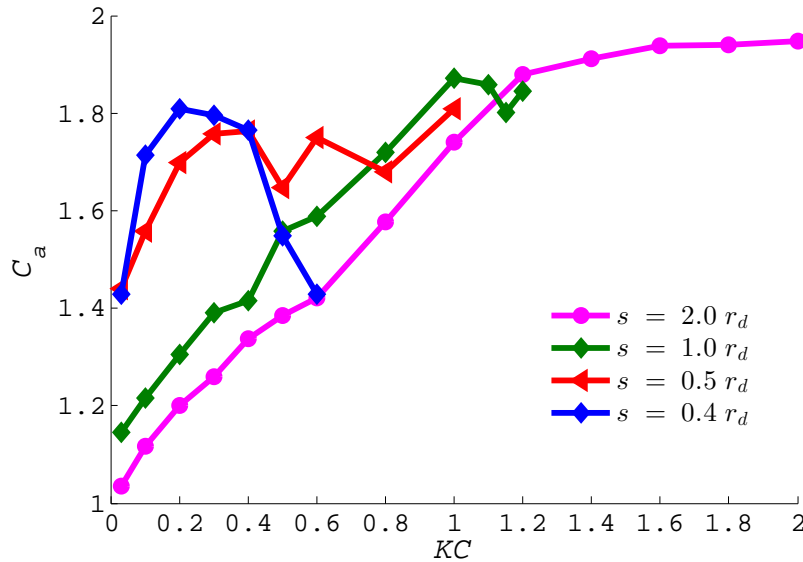


Fig. 5.30 Comparison of the added mass coefficient at different submergences from the free surface using Eqn. (4.46).

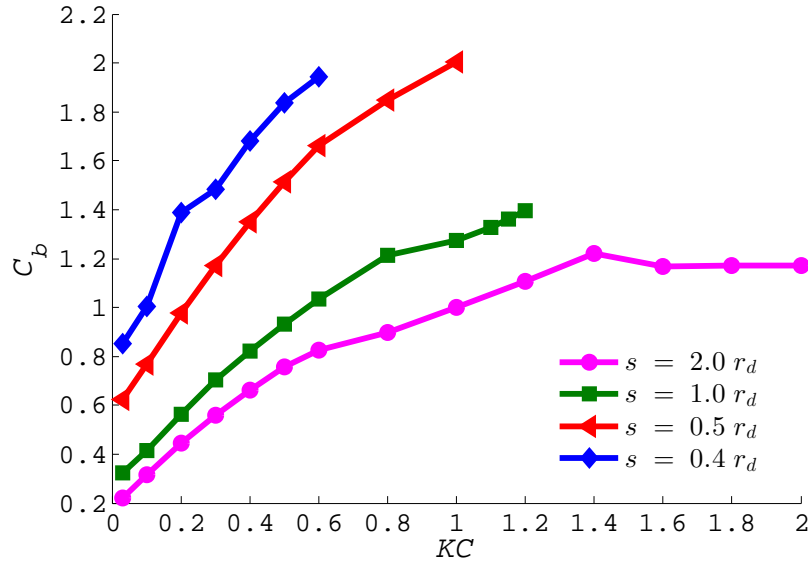


Fig. 5.31 Comparison of the damping coefficient at different submergences from the free surface using Eqn. (4.47).

The behaviour of the added mass when reach certain KC value as the disc approaches to a free surface was also observed in the case when the disc oscillates near the seabed. Fig. 5.32 shows the relation of the critical KC and the s/r_d ratio.

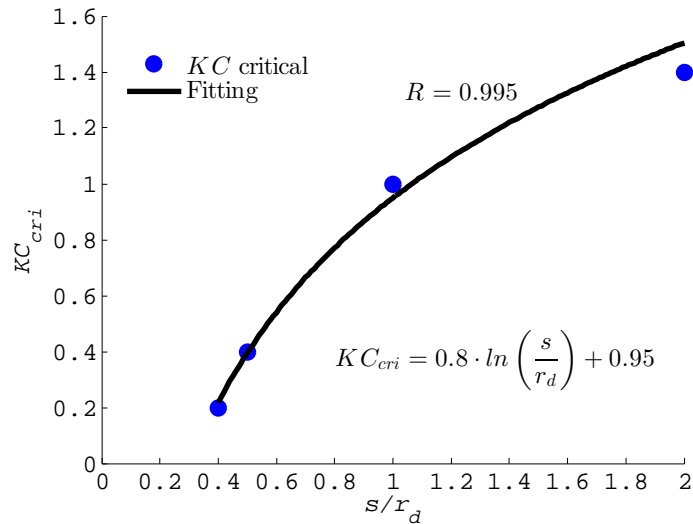


Fig. 5.32 Critical KC vs disc submergence from free surface ' s '.

In order to describe the dependence of C_a and C_b coefficients on the submergence and KC number, the slope and offset of the least square linear fitting of such coefficients have been obtained. These two parameters (slope and offset) change quite dramatically for structures

oscillating very close to the seabed and stabilize as the disc distance to the free surface increases. The values are summarized in Table 5.4. In general, the slope decreases continuously as the disc oscillates at larger submergences, s/r_d , from the free surface. A power regression analysis of the slope and offset data of the Table 5.4 allows one to express C_a and C_b in terms of s/r_d for each KC value (see Eqn. (5.7) and (5.8)). These expressions can be used to evaluate the added mass and damping for a disc oscillating closer to a free surface. Figs. 5.33 and 5.34 show the comparison between the calculated coefficients and those fitted by Eqns. (5.7) and (5.8). The agreement is satisfactory.

Table 5.4 Slope and offset of curve fits for C_a and C_b .

Submergence s	C_a		C_b	
	Slope ($\partial C_a / \partial KC$)	Offset	Slope ($\partial C_b / \partial KC$)	Offset
$2.0 r_d$	0.70	1.04	0.63	0.22
$1.0 r_d$	0.64	1.15	0.91	0.32
$0.5 r_d$	0.86	1.44	1.98	0.62
$0.4 r_d$	1.25	1.43	2.49	0.85

$$C_a = 0.90 \frac{s^{-0.95}}{r_d} KC + \frac{0.15}{\frac{s}{r_d}} + 1; \quad (5.7)$$

$$C_b = 1.25 \frac{s^{-0.95}}{r_d} KC + \frac{0.15}{\frac{s}{r_d}} + 0.2; \quad (5.8)$$

In order to validate the above expression for added mass (Eqn. 5.7), a comparison with published data is made in Fig. 5.35. Figure shows that the added mass obtained by present work differs from Greenhow's data (non-dimensionalized with $\rho \pi r^2$) for smaller submergences ($s/r_d \ll 0.5$) due to fact that Greenhow used a horizontal circular cylinder in his work, but both cases, when the disc or cylinder approach the free surface, the heave added mass becomes infinite.

5.2.4.3 Flow patterns analysis

5.2.4.3.1 General. In the same way that in the previous case (disc oscillating close to the seabed), flow visualisation for observing the vortex shedding generated by an oscillating body is presented in the next section, where the effect of the free surface is shown due to the radiated waves by a submerged disc heaving very near the free surface. The dissipation terms (\dot{E}_ω and \dot{E}_{fs}) are also shown.

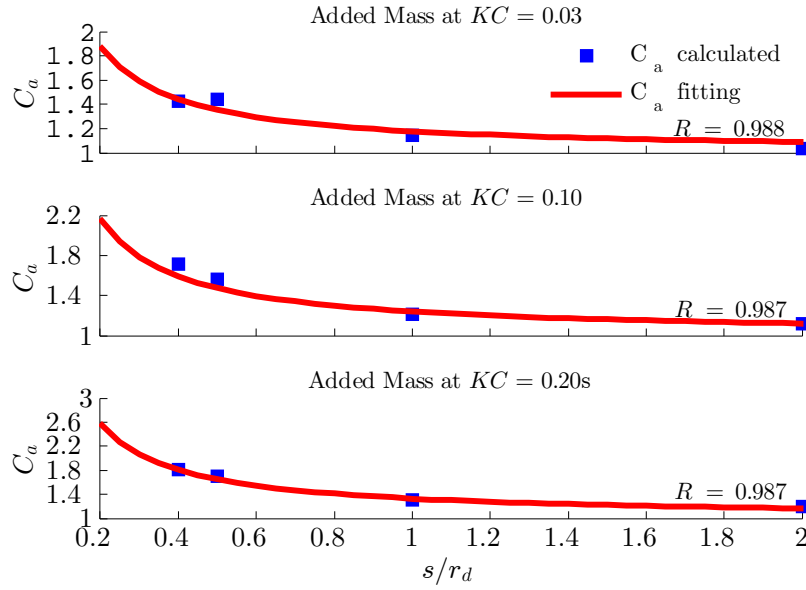


Fig. 5.33 Variation of C_a with disc submergence from the free surface for different KC numbers.

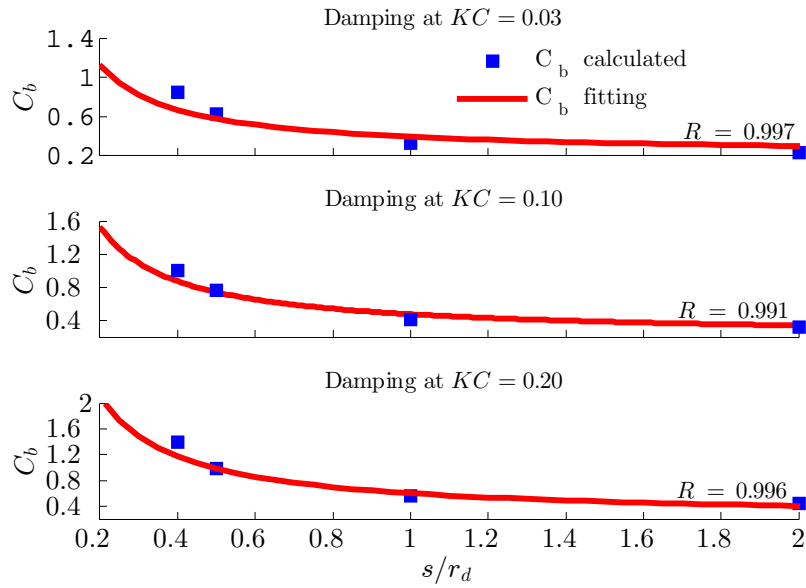


Fig. 5.34 Variation of C_b with disc submergence from the free surface for different KC numbers.

5.2.4.3.2 KC influence. Fig. 5.36 shows, in frames equally spaced over one cycle, the distributions of the vorticity, where red denotes positive values and blue means negative. Results are presented for increasing KC values in panels *a*, *b* and *c*. For low and intermediate KC numbers, as the disc begins the descent (frames a1, b1), a dominant positive vortex (red) is created (frames a2, b2), which pairs with the negative vortex (blue) in the upstroke,

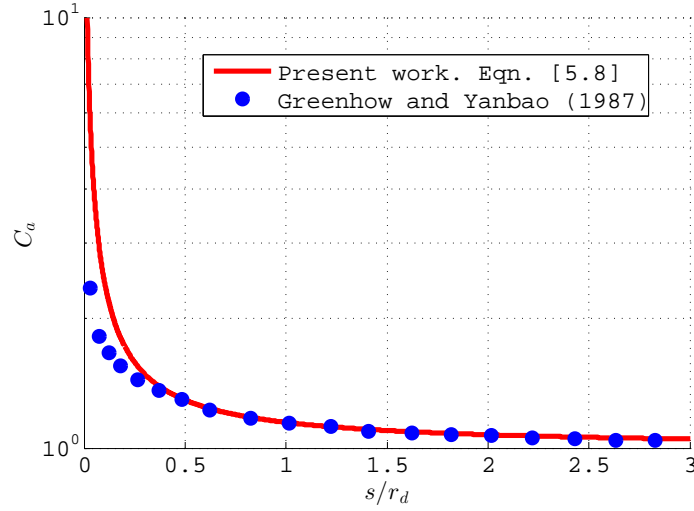


Fig. 5.35 Comparison of C_d between Eqn. (5.7) ($A_{33}/(8/3 \rho r_d^3)$) and analytical results from **Greenhow and Yanbao (1987)** ($A_{33}/(\rho \pi r^2)$).

resulting in shedding of the vortex pair (frames a6, b6). When the disc reaches the maximum absolute displacement, the flow separates from the disc surface causing vortex shedding (frames a8, b8). Fig. 5.36(c) shows the instantaneous vorticity contours obtained at a higher Keulegan-Carpenter number, $KC = 1.20$. With the higher KC the strength of the vortices formed are much stronger due to the higher vorticity level shed from the edges of the disc, and the radiated waves are generated, which help to dissipate the energy produced by the movement of the disc.

Fig. 5.37 show the vorticity generation when the disc oscillates around the critical KC number. In general words, the shed patterns are similar for all amplitudes of oscillation for a disc moving close to a free surface, increasing the strength of the vortices as the KC increase. It indicates, as we see in Fig. 5.31, that the damping coefficient keeps the increasing trend with the KC number for a fully submerged disc, unlike the added mass that shows a change in the growing trend when disc reaches a certain KC value due to less fluid being accelerated.

5.2.4.3.3 Influence of submergence ratio (s/r_d). Added mass and damping coefficients are shown to be influenced strongly by the free surface effect, which depend on the amplitude of the oscillation and on the depth of submergence from the free surface (s/r_d). Fig. 5.38 shows the vortex patterns at a constant KC for three different submergence ratios. Fig. 5.38(a) shows that as the disc mean position is closer to a free surface the intensity of the vortices increases, as well as the radiated wave is clearly generated.

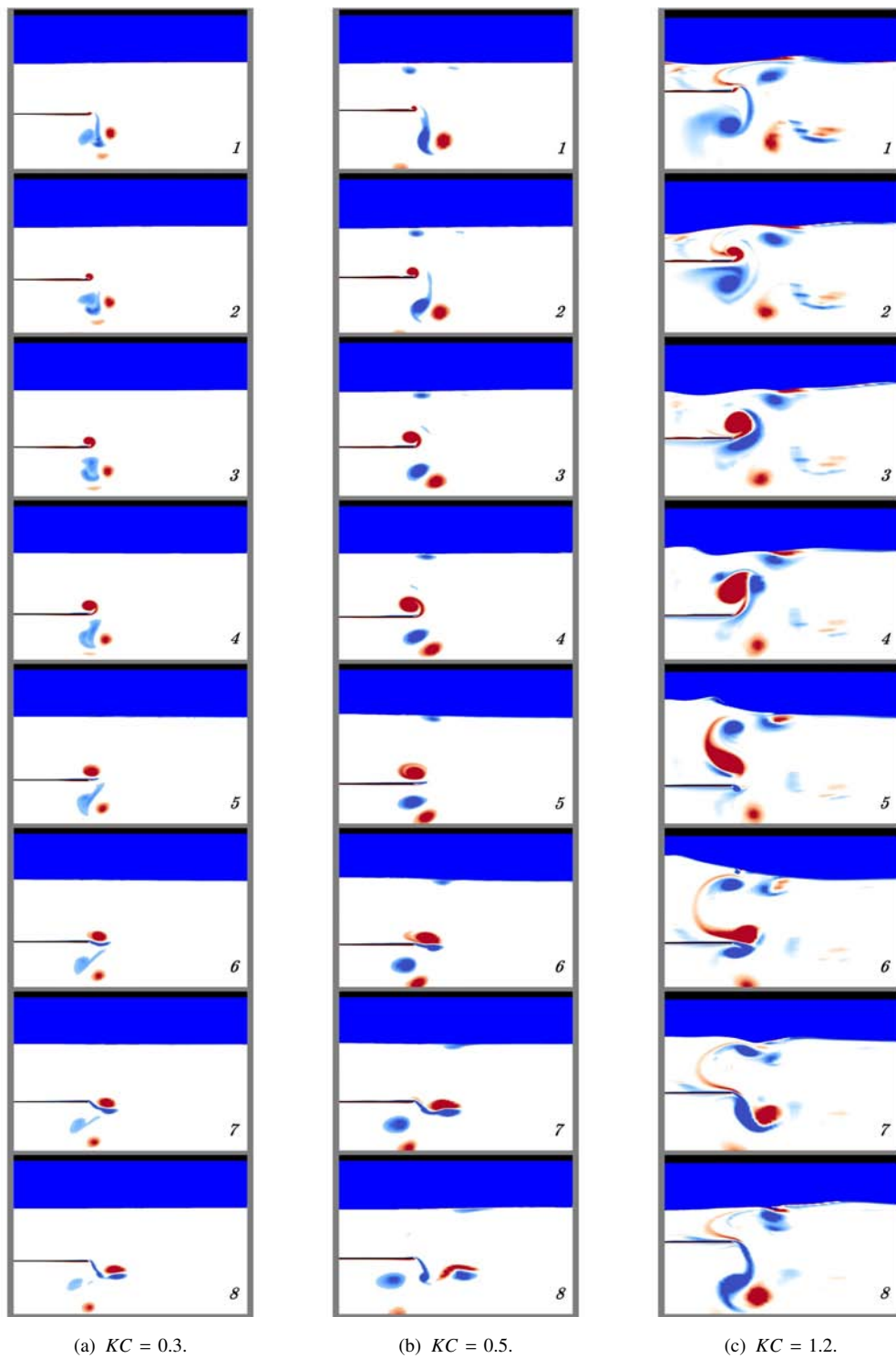
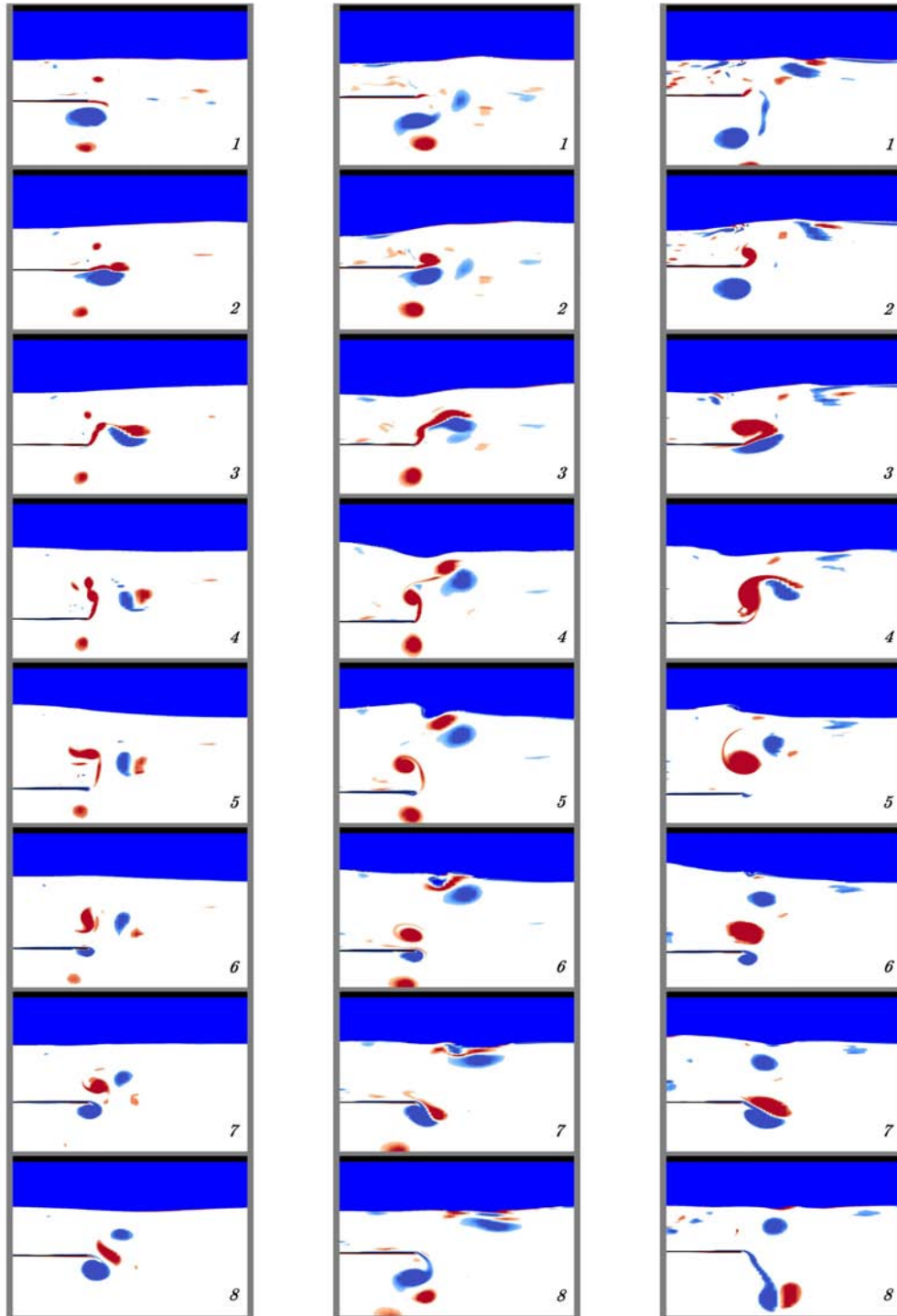


Fig. 5.36 Vortex generation around disc close to the free surface at $s/r_d = 1.0$. (Vorticity scale varies from -25 s^{-1} (blue) to 25 s^{-1} (red).)



(a) Vortex generation around the disc at $KC/KC_{cri} = 0.80$.
 (b) Vortex generation around the disc at $KC/KC_{cri} = 1.00$.
 (c) Vortex generation around the disc at $KC/KC_{cri} = 1.10$.

Fig. 5.37 Vortex generation around the disc at $s/r_d = 1.0$ from the mean free surface. Blue lines indicate negative vorticity (initial condition: Top Dead Centre). Scale varies from -25 s^{-1} (blue) to 25 s^{-1} (red).

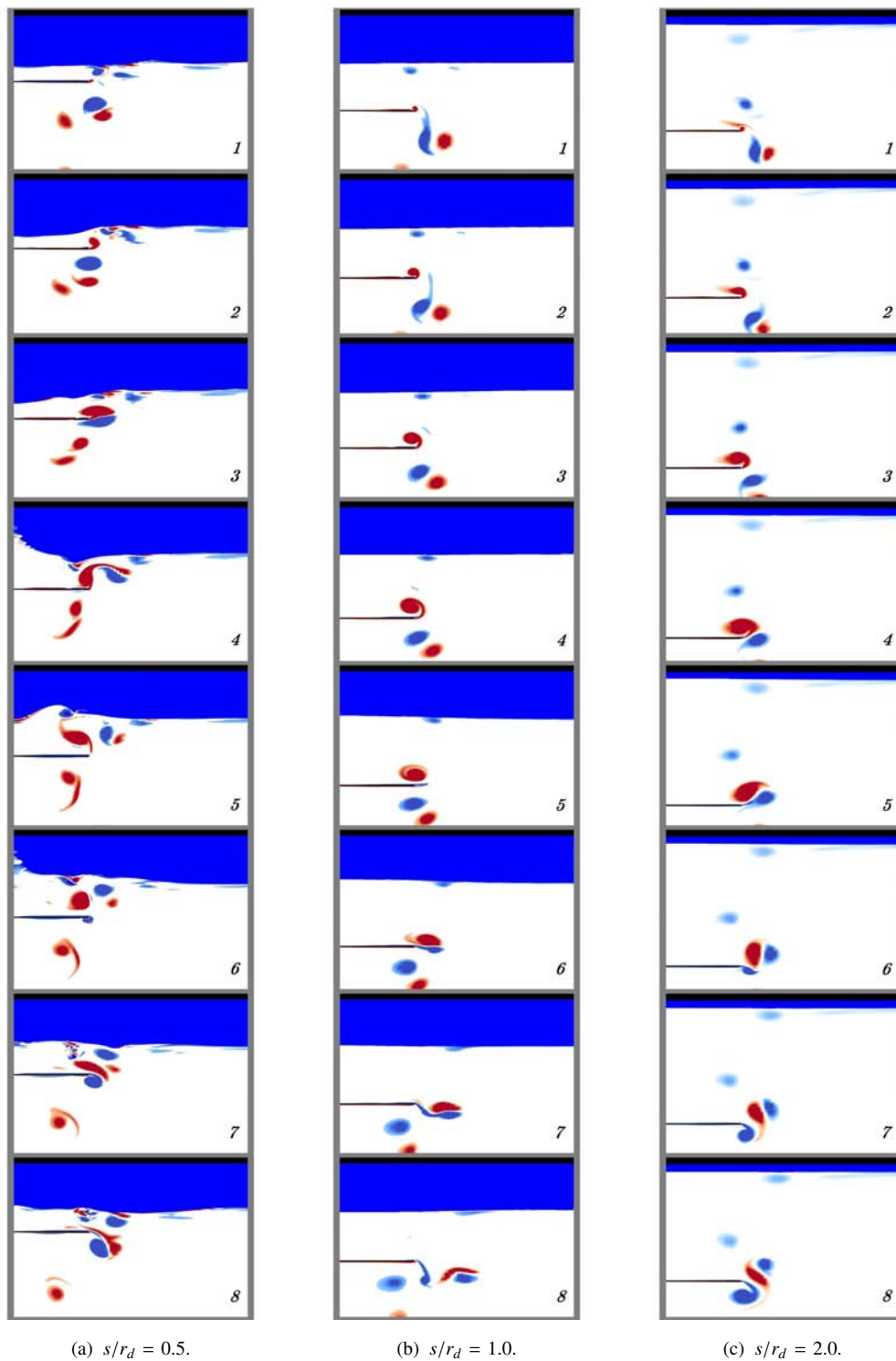


Fig. 5.38 Vortex generation around the disc under the free surface at $KC = 0.5$. (Scale varies from -25 s^{-1} (blue) to 25 s^{-1} (red).)

5.2.4.4 Enstrophy and free surface dissipation terms analysis

5.2.4.4.1 KC influence. Unlike the case when the disc oscillates near the seafloor, a disc moving closer to a free surface dissipates energy from the enstrophy term ($\dot{\mathcal{E}}_\omega$) and from the radiated waves ($\dot{\mathcal{E}}_{fs}$).

Figures 5.39 to 5.46 show the time history of the enstrophy and free surface dissipation terms for different KC numbers. Fig. 5.40 shows that for a specific submergence ratio the fluid dissipates more energy as the amplitude of oscillation increases due to the higher vorticity shed, and the energy dissipated by the radiated waves also increases (see Fig. 5.42), confirming the linear trends of the damping coefficient.

Figs. 5.44 and 5.46 show the dissipation terms at $s/r_d = 1$ for different amplitudes of the oscillation around the critical KC value. From these figures is clearly observed that for large KC values, both dissipation terms ($\dot{\mathcal{E}}_\omega$ and $\dot{\mathcal{E}}_{fs}$) present a similar quantity of energy dissipation, but for smaller KC values the energy dissipation is dominated by the vortex shedding.

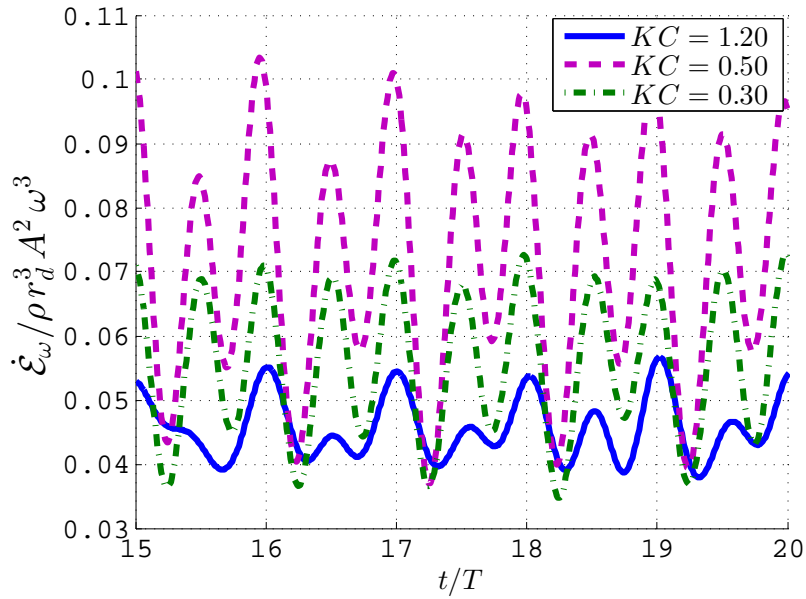


Fig. 5.39 Time history of the enstrophy term from Eqn. (4.20) for an oscillating disc close to the free surface for different KC values at $s/r_d = 1.0$. Markers correspond to the frames depicted in Fig. 5.36.

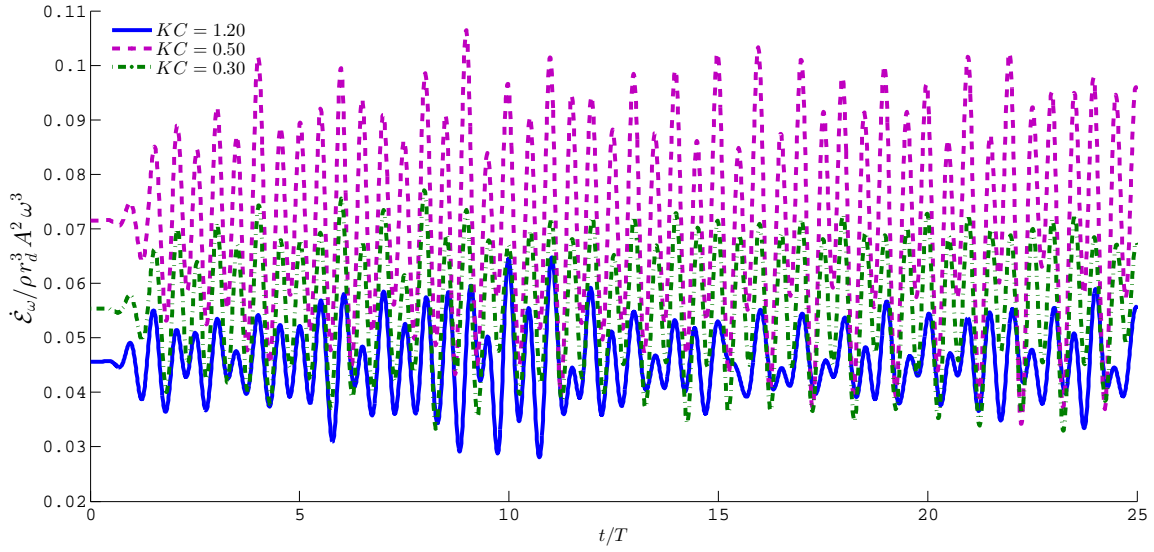


Fig. 5.40 Time history of the enstrophy term from Eqn. (4.20) for an oscillating disc close to the free surface for different KC values at $s/r_d = 1.0$.

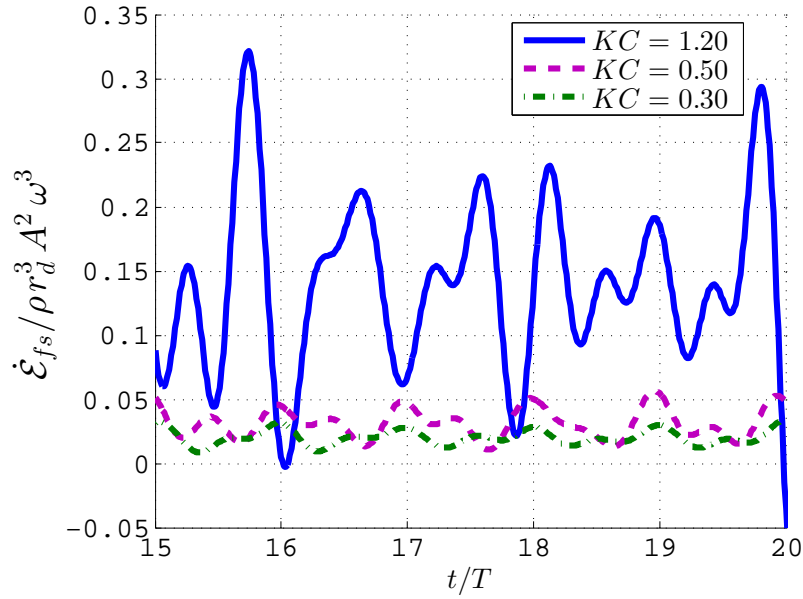


Fig. 5.41 Time history of the free surface dissipation term from Eqn. (4.21) for an oscillating disc close to the free surface for different KC values at $s/r_d = 1.0$. Markers correspond to the frames depicted in Fig. 5.36.

5.2.4.4.2 Influence of submergence distance ratio (s/r_d). It is also important to analyze the effect that the free surface has on the dissipation terms. Fig. 5.47 and 5.48 shows the enstrophy and free surface dissipation integral, respectively, for different submergence

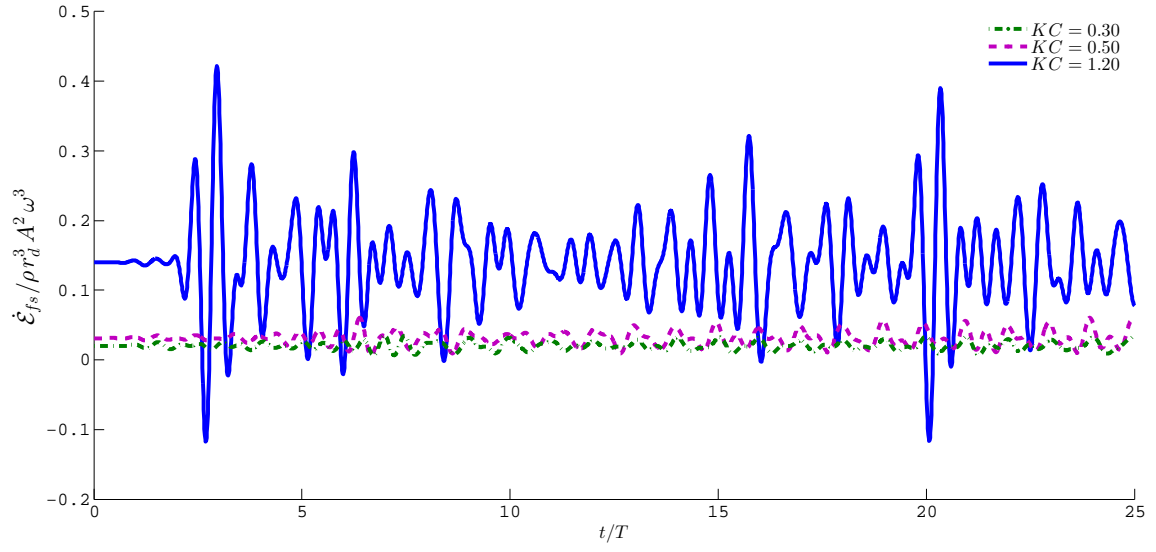


Fig. 5.42 Time history of the free surface dissipation term from Eqn. (4.21) for an oscillating disc close to the free surface for different KC values at $s/r_d = 1.0$.

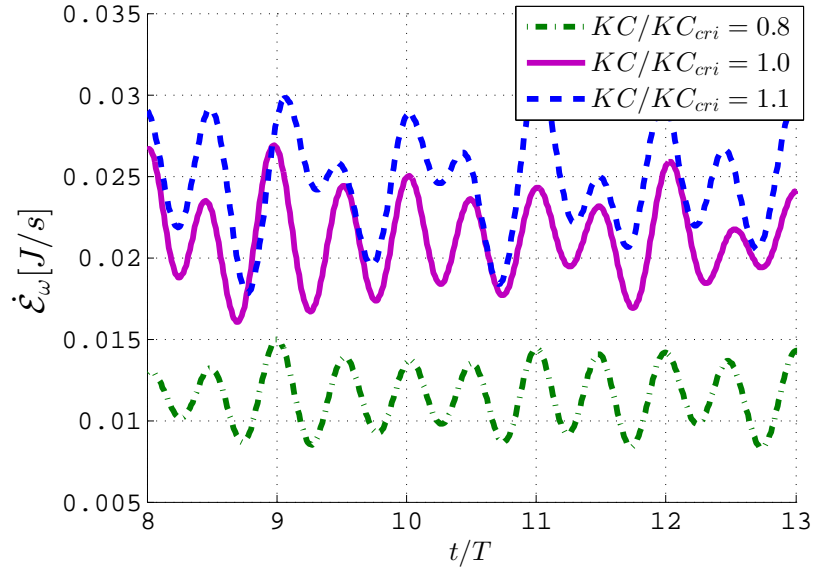


Fig. 5.43 Time history of the enstrophy term from Eqn. (4.20) for an oscillating disc close to the free surface at $s/r_d = 1.0$ around critical KC value. See Figs. 5.31 and 5.37 for $h/r_d = 1.0$.

ratios ‘ s ’.

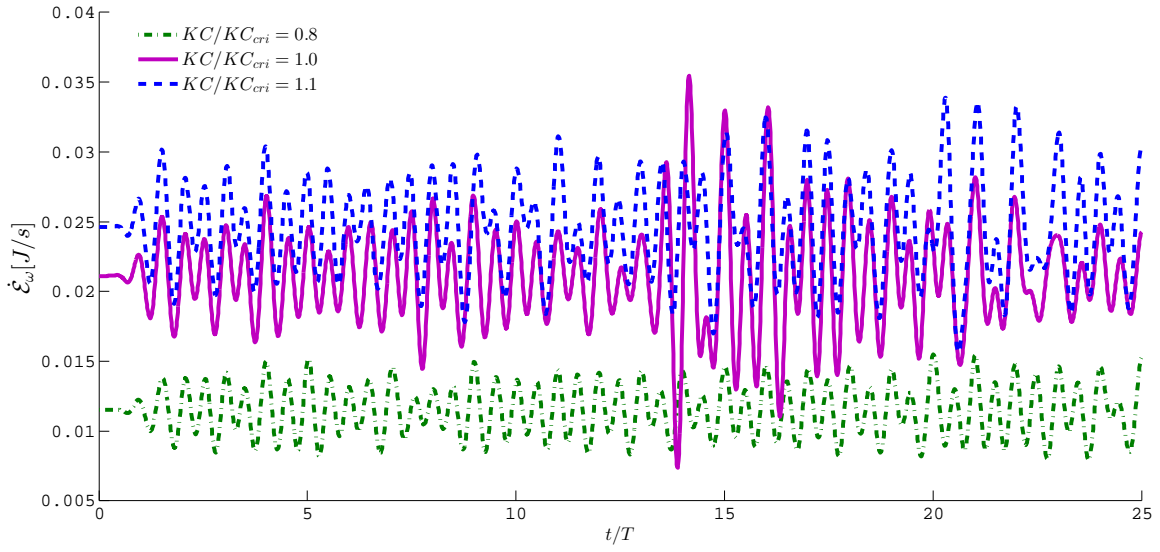


Fig. 5.44 Time history of the enstrophy term from Eqn. (4.20) for an oscillating disc close to the free surface at $s/r_d = 1.0$ around critical KC value.

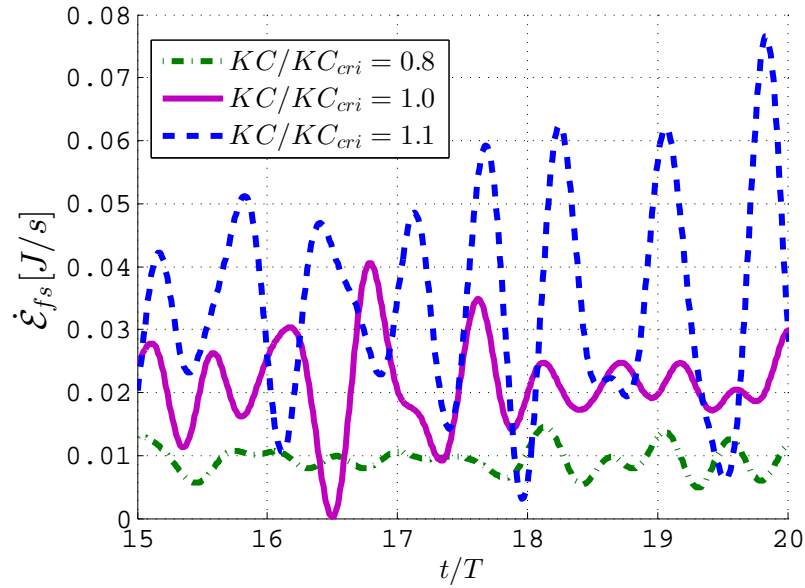


Fig. 5.45 Time history of the free surface dissipation term from Eqn. (4.21) for an oscillating disc close to the free surface at $s/r_d = 1.0$ around critical KC value. See Figs. 5.31 and 5.37 for $s/r_d = 1.0$.

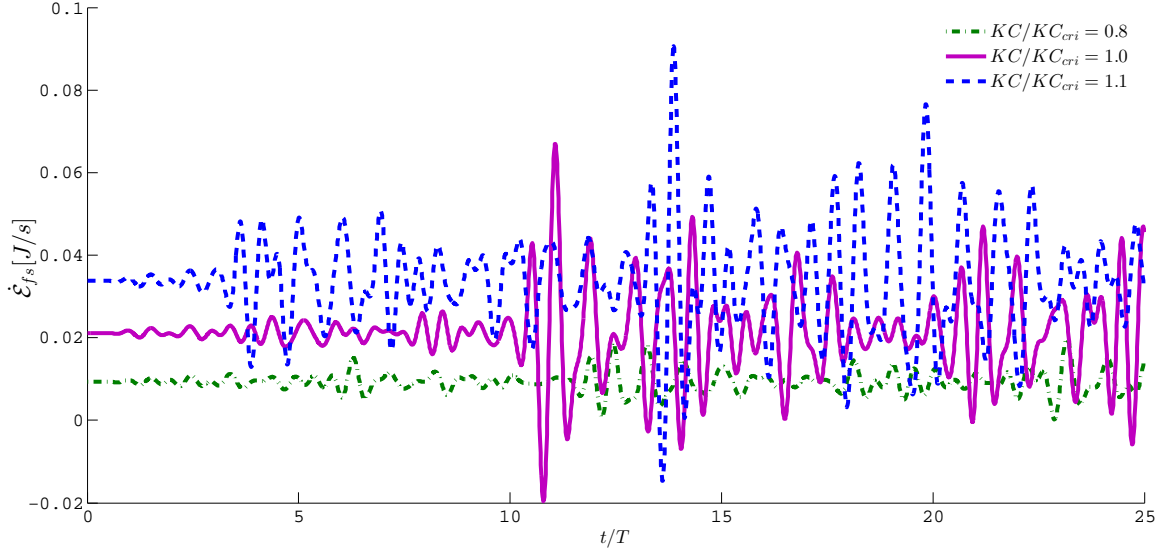


Fig. 5.46 Time history of the free surface dissipation term from Eqn. (4.21) for an oscillating disc close to the free surface at $s/r_d = 1.0$ around critical KC value.

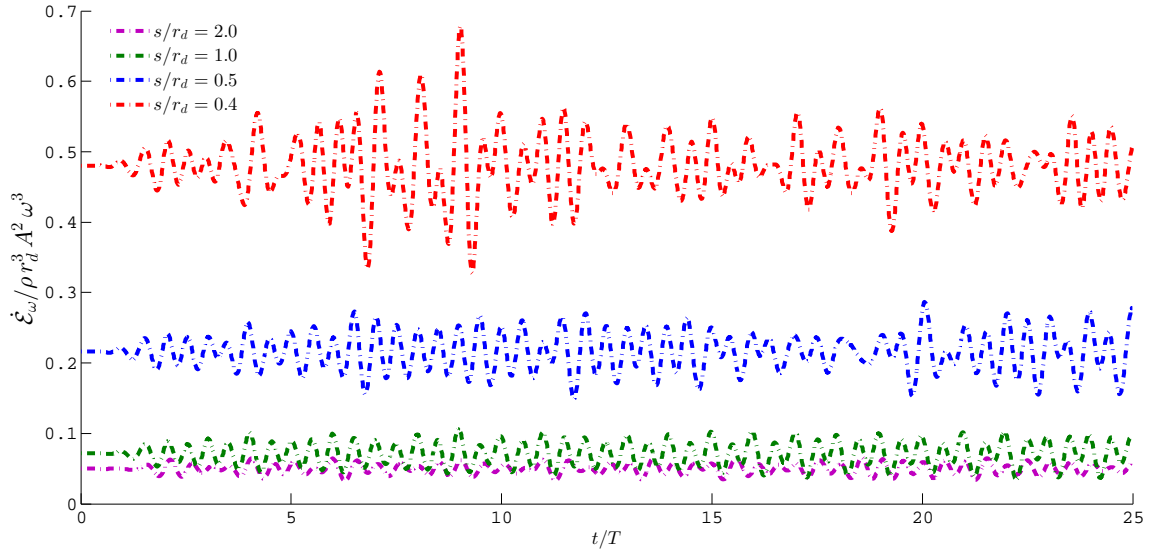


Fig. 5.47 Time history of the enstrophy term from Eqn. (4.20) for an oscillating disc close to the free surface for different s/r_d values at $KC = 0.5$.

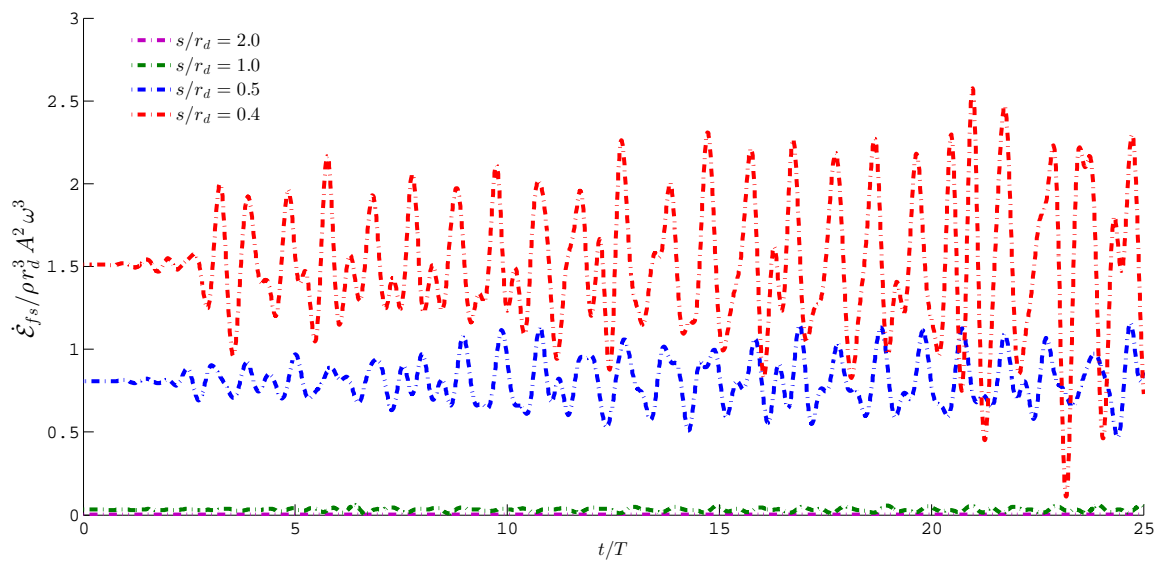


Fig. 5.48 Time history of the free surface dissipation term from Eqn. (4.21) for an oscillating disc close to the free surface for different s/r_d values at $KC = 0.5$.

5.2.4.4.3 Damping and Enstrophy comparison. The relationship between the damping coefficient $B_{33\omega}$ obtained through the dissipation terms (Eqn. (4.39)) and the damping coefficient obtained with the classical forces projection approach (Eqn. (4.47)), are discussed hereinafter. Figs. 5.49 – 5.51 show the comparison of the damping coefficient obtained with both approaches for three representative cases. The matching is, in general, very good. This indicates that the enstrophy and free surface contribution to the dissipation, $\dot{\mathcal{E}}_\omega$ and $\dot{\mathcal{E}}_{FS}$, may be the lead actor in these type of flows.

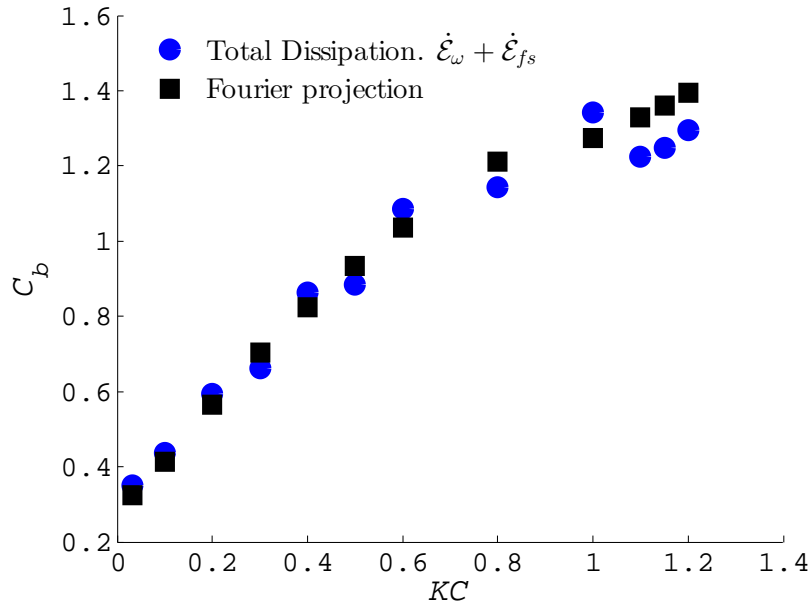


Fig. 5.49 Comparison of hydrodynamic damping coefficient (C_b) with B_{33} at $s/r_d = 1.0$, obtained with Eqn. (4.39) and classical (Sarpkaya and Isaacson, 1981) Fourier projection (Eqn. (4.47)), for an oscillating heave plate near a free surface.

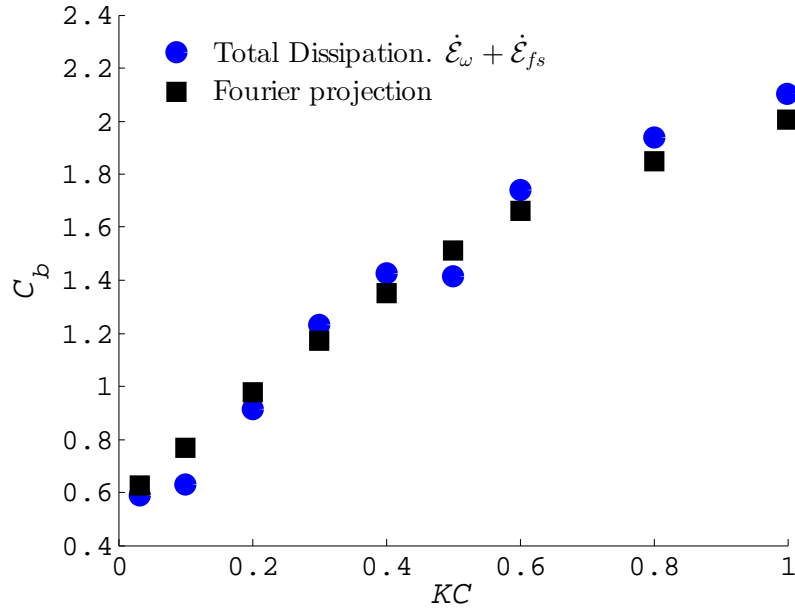


Fig. 5.50 Comparison of hydrodynamic damping coefficient (C_b) with B_{33} at $s/r_d = 0.5$, obtained with Eqn. (4.39) and classical (Sarpkaya and Isaacson, 1981) Fourier projection (Eqn. (4.47)), for an oscillating heave plate near a free surface.

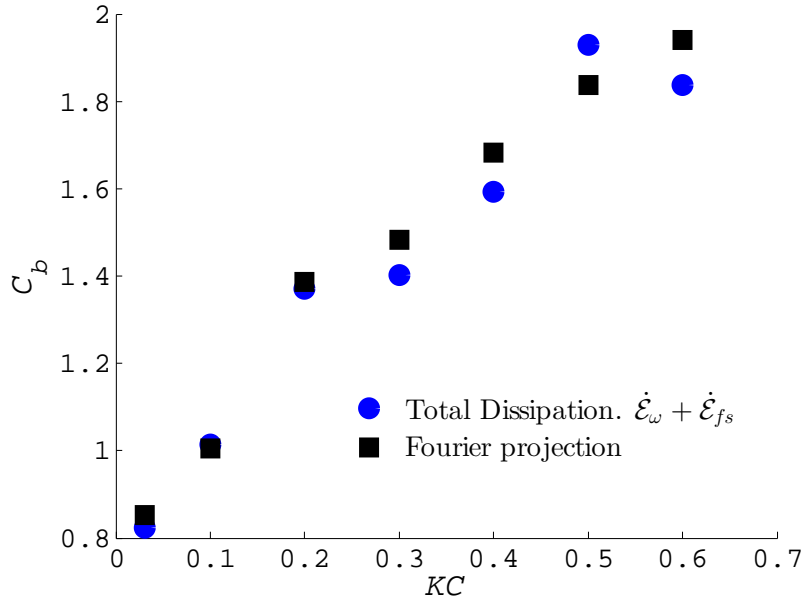


Fig. 5.51 Comparison of hydrodynamic damping coefficient (C_b) with B_{33} at $s/r_d = 0.2$, obtained with Eqn. (4.39) and classical (Sarpkaya and Isaacson, 1981) Fourier projection (Eqn. (4.47)), for an oscillating heave plate near a free surface.

5.3 Analogies between plates oscillating close to free surface and seabed

Figs. 5.52 and 5.53 show a comparison of the hydrodynamic coefficients for a disc oscillating close to the seabed and the free surface at varying KC numbers. As can be seen, for large h/r_d or s/r_d ratios the coefficients presents similar values at smaller oscillations, and differs for higher KC numbers showing that the free surface effects have more influence than the seafloor. As the disc approaches to the seabed or the free surface (smaller h/r_d or s/r_d ratios) the coefficients for the free surface case are greater than those when the disc oscillates near the seabed.

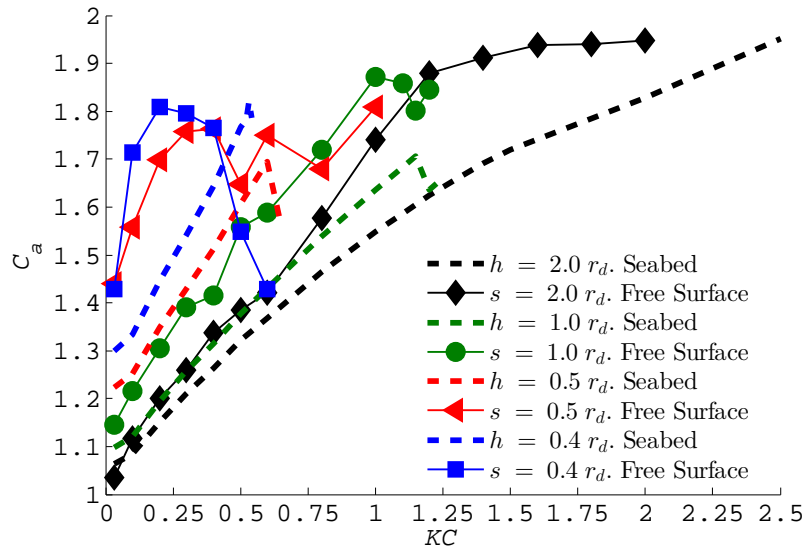


Fig. 5.52 Comparison of added mass coefficient for a disc oscillating close to the seabed and the free surface using Eqn. (4.46).

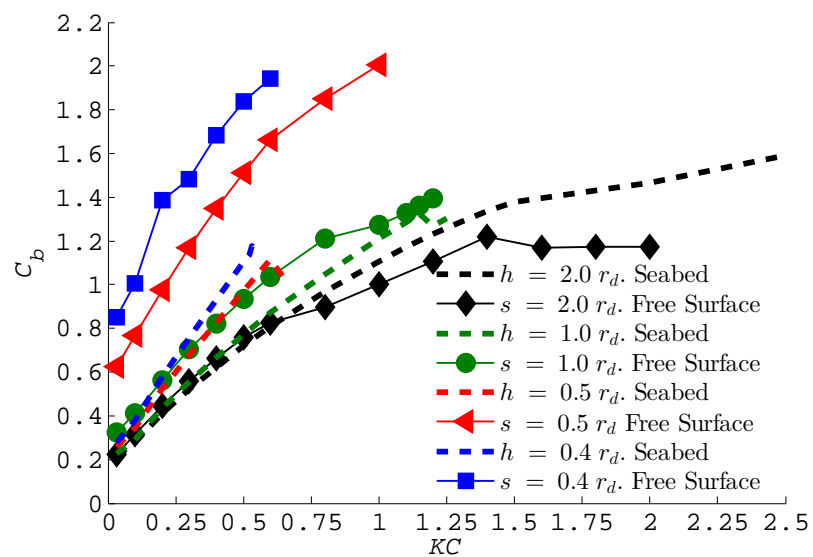


Fig. 5.53 Comparison of damping coefficient for a disc oscillating close to the seabed and the free surface using Eqn. (4.47).

Chapter 6

Hydrodynamic coefficients of an oscillating semi-submersible column with a heave plate

6.1 General

The motion response, especially heave response, should be minimal for effective and efficient working of floating offshore platforms because this motion is primarily responsible for increasing the downtime as well as causing damage to the risers and moorings systems due to excessive vertical motion of the platform. In order to reduce heave, damping elements such as heave plates are sometimes used.

This section will study the hydrodynamic forces of a semisubmersible column with a heave plate attached on its bottom.

6.2 Case study description

6.2.1 Experimental investigation

The experiments were conducted in the tow tank at the School of Naval Architecture and Ocean Engineering (ETSIN), Technical University of Madrid which has dimensions 100 meters long, 3.8 *m* wide and 2.2 *m* deep. A sketch of the transversal section (the restrictive one) of the basin, including the specimen, is presented in Figure 6.1. Regarding eventual bottom effects, the ratio, h/r_d , between the distance to the bottom and the disc radius is $(2.2 - 0.775)/0.5 = 2.85$. With this ratio and according to the numerical analysis of Garrido-

Mendoza et al. (2013), the effect of the bottom on the heave plate flow is expected to be negligible.

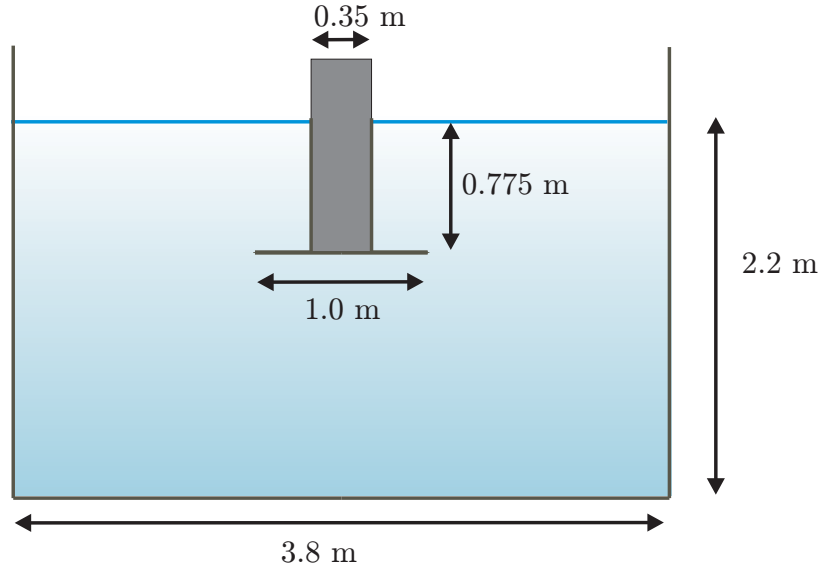


Fig. 6.1 Sketch of the column and the plain disc and transversal section of the basin.

6.2.1.1 Model

The heave plates under study belong to the semi-submersible platform whose second order surge motions were analyzed by Lopez-Pavon et al. (2013) and whose damping properties were discussed in Lopez-Pavon and Souto-Iglesias (2015). The structure of the floater consists of three vertical columns linked by trusses. A circular heave plate is added to the bottom of each column, as a mean to increase the natural heave period and, as a consequence, to prevent resonant motions in both operational and survival sea states.

The main dimensions of the platform are given in Table 6.1 and a schematic view of the floater geometry is presented in Fig. 6.2. The depth-radius ratio of the heave plate can be considered large ($15.5/10=1.55$). To put this figure in perspective, it must be noted that, for example, Wadhwa and Thiagarajan (2009), in their specific work regarding free surface influence in hydrodynamic coefficients, considered only depth-radius ratios lower than 0.5. With this depth-radius ratio (1.55), it is expected that viscous damping will be dominant with respect to radiation damping.

In order to assess the added mass and damping characteristics of the platform when subjected to heave motion, a 1 : 20 scale single column model was built. The distance between the center of the legs is 35 m and the distance between the plate edges of two columns is 15 m both at full scale. This distance is significantly larger than the maximum considered

Table 6.1 Main dimensions of the platform (prototype and model scale, 1:20). Distance between legs not included at model scale since only one column model was considered. Full scale heave plate steel thickness not available.

Characteristic	Symbol	Prototype	Model
Platform draft, disc depth	s	15.5 m	0.775 m
Legs centre to centre distance		35 m	
Columns diameter	D_c	7.0 m	0.35 m
Heave plate (disc) diameter	D_d	20 m	1.0 m
Heave plate (disc) radius	r_d	10 m	0.5 m
Heave plate (disc) thickness	t_d		5 mm
Depth-radius ratio	s/r_d	1.53	1.53
Disc aspect ratio	t_d/D_d		0.0049
Leg mass	M	663 t	82.83 kg
Disc distance to the tank bottom	h_b		1.425 m
Disc distance to the bottom-radius ratio	h_b/r_d		2.85

motion amplitude (2.8 m). Since the characteristic length of the vortex structures that are generated during heave motion is of the order of the motion amplitude, the heave motion hydrodynamic interaction between the columns is expected to be not significant. This is the main technical reason behind testing one individual column when it comes to optimizing the heave plate design. For subsequent design phases (e.g. mooring design), a complete model of the platform was built and tested (Lopez-Pavon et al., 2013). The shape of the disc edge is rectangular. As shown by Li et al. (2013), this shape may have some influence in the hydrodynamic performance of the plate.

In the experimental work of the references cited in Chapter 1 (e.g. An and Faltinsen (2013); Tao and Dray (2008)), the models were no larger than 0.5 m in side length for rectangular plates or diameter for circular plates. A larger model has been used in the present investigation (1 m diameter plate), thus becoming, to the candidate knowledge, the largest for which data has been published. This larger size implies that under the same conditions, the forces involved in the present analysis are 8 times larger, thus helping to reduce measurement uncertainties and scale effects.

6.2.1.2 Excitation force and motion measurement experiments

The motion is generated with a 1.3 kW electric actuator (FESTO DNCE 63-300-BS-10-PQ). The actuator is attached to the towing tank trolley with a frame (left panel of Fig. 6.3). The actuator had previously been used to generate high precision motions (± 0.01 mm) in a sloshing rig (Bulian et al., 2014).



Fig. 6.2 Semisubmersible platform case study sketch.

The force signals were measured using a load cell placed between the actuator and the leg model (center panel of Fig. 6.3). The cell model was Tedeo Huntleigh 615-s-type G, with a range of ± 200 kg and a precision of 0.02%. This uncertainty is lower than the one associated to the 24 bits analog-digital converter used.

6.2.1.3 Test matrix

For the model described above, the experiments were mainly divided in four parts:

- Part 1: Tests on solid plain plate at varying depths, oscillation amplitudes and frequencies to check the effect of the immersed depth of the plate on the hydrodynamic coefficients. These tests are thoroughly discussed in [Lopez-Pavon and Souto-Iglesias \(2015\)](#).



Fig. 6.3 (Left) Frame attached to the towing tank trolley, actuator and heave plate. (Center) Load cell. (Right) Top view of the model.

- Part 2: Tests on plates at different scales, to perform a sensitivity study of scale.
- Part 3: Tests on plates with flaps, to study the influence of the shape of the edge on the hydrodynamics of the plates.
- Part 4: Tests on fractal heave plate, to investigate the influence of the perforation ratio and hole sizes on the hydrodynamics of the plates.

6.2.1.3.1 Solid heave plate. Vertical oscillations were performed with different amplitudes (0.05, 0.1, 0.14 m) and periods (1 to 4 s). For each period, the maximum feasible amplitude depended on the actuator power, leading to smaller motion amplitudes for the highest oscillation frequencies. The test matrix is presented in Table 6.2, with β being the frequency parameter (Eqn. 4.30), Re the Reynolds number (Eqn. 4.31) and m and p subindexes referring to model and prototype scales respectively. As aforementioned, the experiments corresponding to the solid plate are discussed in Lopez-Pavon and Souto-Iglesias (2015). Here the ones corresponding to $\omega = 2.51 \text{ rad/s}$ will be numerically simulated.

The basic geometry to test is formed by a circular Heave Plate and a column of semisubmersible structure, as show in Figure 6.4:

From the forces measured by the load cell located between the actuator and the leg column, the added mass and damping values are extracted computing the first harmonic of the force and its phase with respect to the imposed movement.

Table 6.2 Test matrix for a solid heave plate tests.

ω	A_m	T_{1_m}	KC	β_m	Re_m	A_p	T_{1_p}
[rad/s]	[m]	[s]				[m]	[s]
1.57	0.05	4	0.309	257542	79695	0.985	17.8
2.09	0.05	3	0.309	342842	106091	0.985	13.3
2.51	0.05	2.5	0.309	411738	127411	0.985	11.1
3.14	0.05	2	0.309	515083	159391	0.985	8.9
4.83	0.05	1.3	0.309	792309	245178	0.985	5.8
1.57	0.1	4	0.618	257542	159391	1.97	17.8
2.09	0.1	3	0.618	342842	212183	1.97	13.3
2.51	0.1	2.5	0.618	411738	254822	1.97	11.1
3.14	0.1	2	0.618	515083	318782	1.97	8.9
3.59	0.1	1.8	0.618	588901	364467	1.97	8
4.83	0.1	1.3	0.618	792309	490355	1.97	5.8
1.57	0.14	4	0.866	257542	223147	2.758	17.8
2.09	0.14	3	0.866	342842	297056	2.758	13.3
2.51	0.14	2.5	0.866	411738	356751	2.758	11.1
3.14	0.14	2	0.866	515083	446294	2.758	8.9



Fig. 6.4 Geometry of Heave Plate in a column of semisubmersible.

6.2.1.3.2 Scale analysis. It is also important to perform a sensitivity study of scale, to analyze whether scale effects in the added mass and damping occurs. small scales are faster than large ones.

Figure 6.5 shows the different scales of the model and the dimensions of the geometry at different scales are described in Table 6.3.

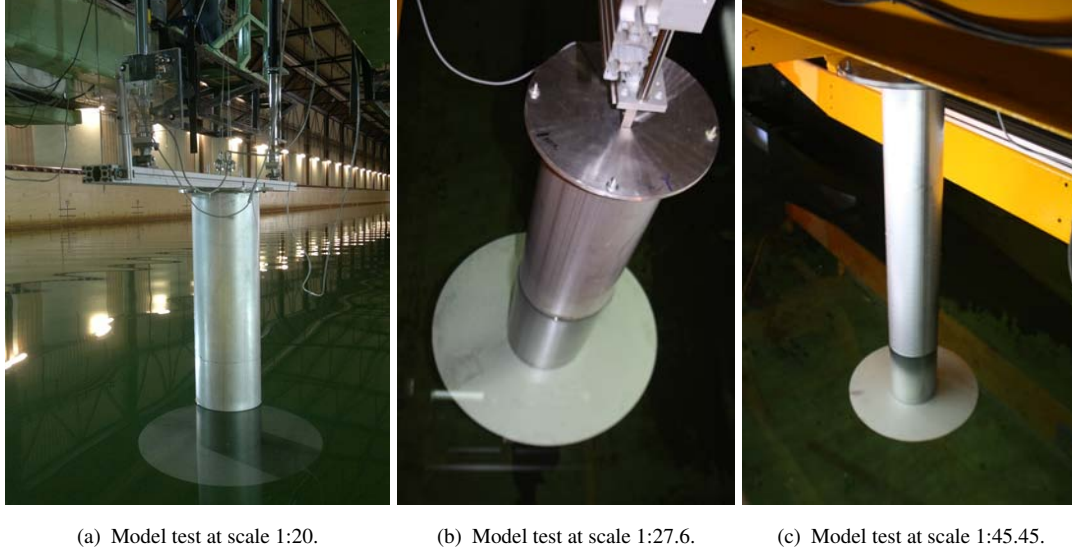


Fig. 6.5 Model of heave plates at different scales.

Table 6.3 Dimensions of the geometry at different scales.

	Scale 1. 1:20	Scale 1. 1:27.6	Scale 1. 1:45.45
Semisubmersible Column			
Diameter [m]	0.354	0.257	0.156
Length [m]	1.187	0.860	0.522
Thickness [m]	0.003	0.0022	0.0013
Heave Plate			
Diameter [m]	1.000	0.7246	0.4400
Thickness [m]	0.005	0.0036	0.0022
Draft [m]			
	0.775	0.5616	0.341

The experimental parameters for the three scales tests are listed in Table 6.4.

6.2.1.3.3 Heave plate with flaps. Several variations of the basic geometry have been investigated. Heave plates with different flaps are presented in Fig. 6.6 and their dimensions and IDs are given in Fig. 6.7.

Considering that the depth at full-scale is set as 10 m for geometries with flaps, the draft at model scale (1 : 20) will be 0.5 m. Thus, initially it is an objective of these tests and

Table 6.4 Test matrix for the different scales tests.

Prototype		Model Scale (1:20)			Model Scale (1:27.6)			Model Scale (1:45.45)		
Amplitude A	Period T [s]	Frequency ω [rad/s]	Amplitude A [m]	Period T [s]	Frequency ω [rad/s]	Amplitude A [m]	Period T [s]	Frequency ω [rad/s]	Amplitude A [m]	Period T $m>m$ [s]
1.00	17.89	1.57	0.05	4.00	1.81	0.04	3.46	2.37	0.02	2.65
1.00	13.42	2.09	0.05	3.00	2.42	0.04	2.60	3.16	0.02	1.99
1.00	11.18	2.51	0.05	2.50	2.90	0.04	2.16	3.79	0.02	1.66
1.00	8.94	3.14	0.05	2.00	3.63	0.04	1.73	4.74	0.02	1.33
1.00	5.81	4.83	0.05	1.30	5.58	0.04	1.13	7.29	0.02	0.86
2.00	17.89	1.57	0.10	4.00	1.81	0.07	3.46	2.37	0.04	2.65
2.00	13.42	2.09	0.10	3.00	2.42	0.07	2.60	3.16	0.04	1.99
2.00	11.18	2.51	0.10	2.50	2.90	0.07	2.16	3.79	0.04	1.66
2.00	8.94	3.14	0.10	2.00	3.63	0.07	1.73	4.74	0.04	1.33
2.00	8.05	3.59	0.10	1.80	4.03	0.07	1.56	5.26	0.04	1.19
2.00	5.81	4.83	0.10	1.30	5.58	0.07	1.13	7.29	0.04	0.86
2.80	17.89	1.57	0.14	4.00	1.81	0.10	3.46	2.37	0.06	2.65
2.80	13.42	2.09	0.14	3.00	2.42	0.10	2.60	3.16	0.06	1.99
2.80	11.18	2.51	0.14	2.50	2.90	0.10	2.16	3.79	0.06	1.66
2.80	8.94	3.14	0.14	2.00	3.63	0.10	1.73	4.74	0.06	1.33

calculations to find out which heave plate geometry is the most suitable to increase the added mass (C_a) of the structure and damping. More specifically, different geometries of the trailing edge of heave plate will be studied to try to increase the vorticity generation without reducing the added mass too much.

6.2.1.3.4 Unconventional design (Fractal heave plate). A novel heave plate based on fractal grid turbulence theory (Cardesa et al., 2012; Cardesa-Dueñas et al., 2011; Nedić et al., 2013) was designed by the candidate. Nedić et al. (2013) found that by increasing the number of fractal iterations, thus the perimeter, the drag coefficient increases by up to 7%. A fractal heave plate was then manufacture and tested experimentally at CEHIPAR ocean basin. The results were then compared with the solid disc. Figure 6.8 shows the new fractal heave plate which has been constructed with a porosity of 20%¹ and multiple holes scales, based in the Sierpinski polygon (Bandt and Hung, 2008; Dennis and Schlicker, 1995) and more details on its geometric characteristics can be found in Appendix F. The fractal plate has 5 different holes sizes in order to enhance the hydrodynamic characteristics of the Solid Plate. It is important to note that the full-scale cost of such kind of designs could be prohibitive compared to a conventional heave plate, but analysing it at model scale (1 : 20) can provide insight into the physics of the problem.

The test matrix used in this set of experiments was the same used for the plain heave plate (section 6.2.1.3.1) and was presented in Table 6.2.

¹Selection of this porosity was made in order to investigate whether the new heave plate design improve the hydrodynamic characteristics of the worse porous plate. Total porosity of the fractal heave plate including the fractal perimeter is 20%.



Fig. 6.6 Model of heave plates with flaps.

6.2.2 CFD calculations.

6.2.2.1 General

In order to investigate the numerical forced heave tests with several amplitudes and different submergences from the free surface have been carried out. The numerical results are compared with the experiments conducted in CEHINAV and CEHIPAR model basins, and with the experimental data by other authors. The aim is to control the natural period (which

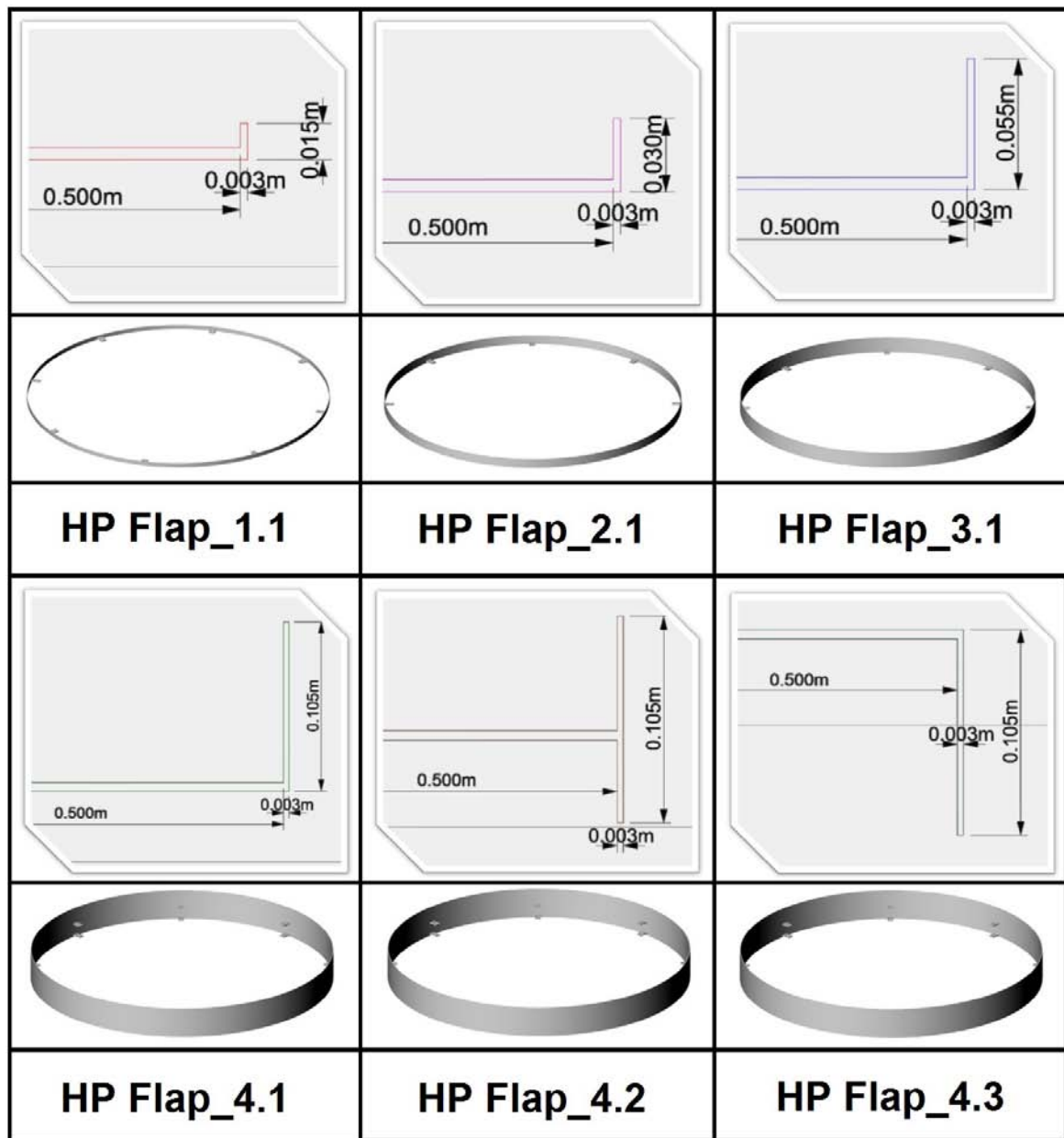


Fig. 6.7 Dimensions of the different flaps attached to the heave plate for which experimental data were available.

depends strongly on the added mass characteristics) and the response amplitude, which depends on the damping, so that the floater operates far from its heave natural period or when that is not the case, to moderate the motion response.

Figure 6.9 shows the simulation setup and boundary conditions used in all cases in this section. Dimensions chosen for the numerical tests are based on the model scale 1 : 20.

The no-flux and no-slip velocity boundary conditions are imposed along the oscillatory



(a) Model of the fractal heave plate.

(b) Experiments setup in CEHIPAR.

Fig. 6.8 Fractal heave plate with 20% of porosity.

body surface. The heave plates were forced to oscillate harmonically in a vertical direction in quiescent water.

In order to compare with experimental data (sections 6.2.1.3.1, 6.2.1.3.3 and [Tao and Dray \(2008\)](#)), different variations of the general geometry have been simulated. Such variations comprise the inclusion of a certain amount of porosity and flaps (Flap case 4.3, Fig. 6.6(e) and variations); it is worth mentioning that since the problem is modelled as axisymmetric, the porosity will be simulated as a ring with the same opening area of each perforation ratio. This implies for the perforation ratios of 5% – 10% – 20% the values of the internal and external radius of the ring change, and may depend of the opening radial position.

The dimensions and IDs of the numerical cases are given in Figure 6.10.

For the plates described above, the simulations were mainly organized in three configurations types:

- Type I: simulations with solid plate (Fig. 6.10a) at varying depths and oscillation amplitudes. The objective of this configuration is to check the effect of the immersed depth of the heave plate on the hydrodynamic coefficients.
- Type II: simulations with porous plates (Fig. 6.10b) to study the influence of the perforation ratio and porosity area on the hydrodynamics of the heave plates. It is expected that porosity will increase the damping properties of the plates, due to the

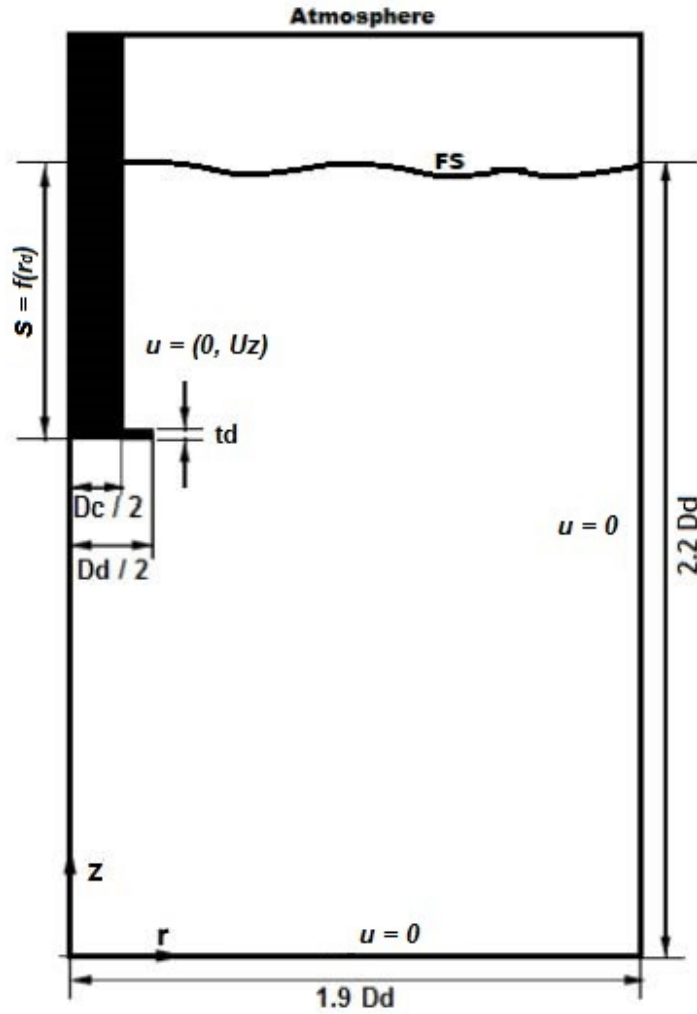


Fig. 6.9 Flow domain and boundary conditions.

onset of new vortices. Porosity ranging from 0% (solid) to 20% was used in order to compare with published experimental data.

- Type III: simulations with Plates with Flaps (Fig. 6.10c-g) to assess to which extent the hydrodynamic forces are affected by the presence of end plates (wingtips or flaps).

The parameters for the simulations of the three types are listed in Table 6.5.

It is relevant mentioning that the range of KC numbers selected (0.12 to 1.4) is typical of vertical oscillations of deep water offshore structures.

All the simulations were conducted with a frequency parameter β of $4 \cdot 10^5$, corresponding to the frequency of oscillation of the cylinder of $0.4Hz$. The reason to use one frequency of oscillation is that as the frequency increases, the value of C_a increases slightly (Li et al., 2013). As a matter of fact, the oscillation frequency has only a slight influence on the added

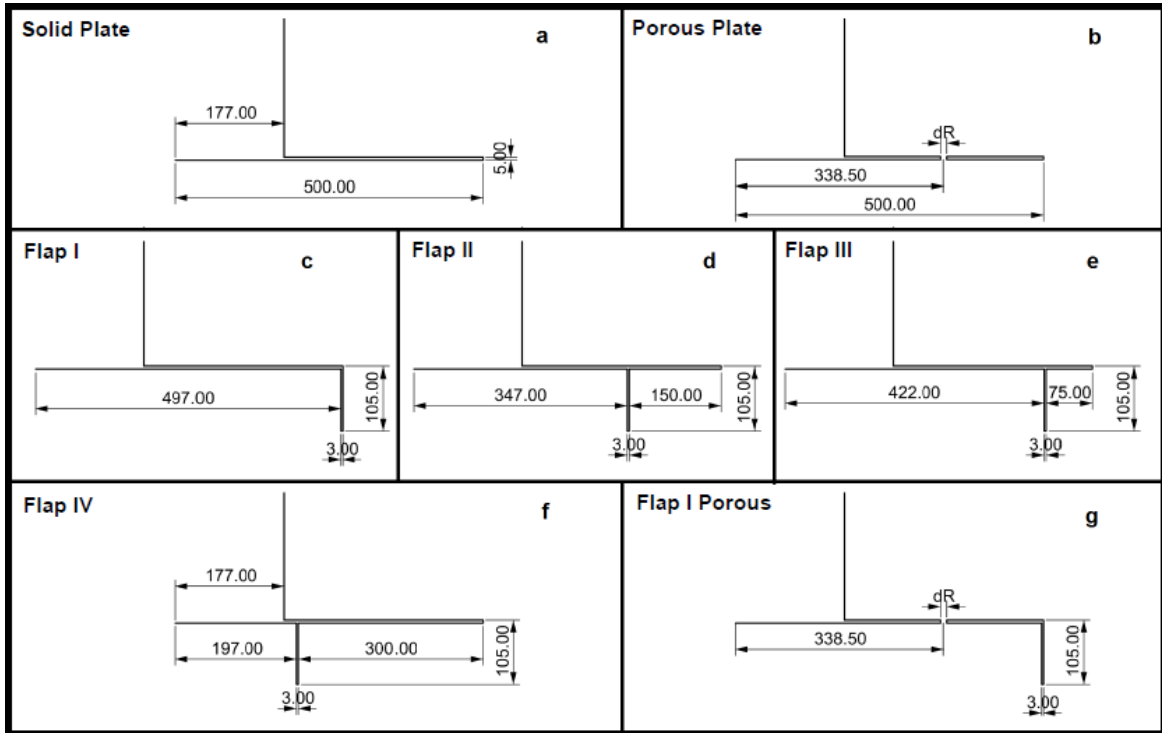


Fig. 6.10 Dimensions of the different heave plates (units in *mm*) considered in the CFD simulations.

Table 6.5 Simulation parameters for the heave plates moving closer to the free surface.

Test	Submergence [<i>m</i>] <i>s</i>	<i>A</i> [<i>mm</i>]	<i>KC</i>	β $\cdot 10^5$	R_e $\cdot 10^4$	Porosity [%] - ΔR - [<i>mm</i>]
Type I	0.1 – 0.77	20 – 230	0.12 – 1.4	3 – 5	4.8 – 56	0 - 0
Type II	0.77	50 – 140	0.31 – 0.88	4	12 – 35	5, 10, 20 - 16, 32, 65
Type III	0.77	50 – 140	0.31 – 0.88	4	12 – 35	10 - 32

mass coefficient of a plate, and the effects of the oscillating frequencies on the damping coefficient are small and can be neglected. This observation of the effect of the frequencies on C_a and C_b is consistent with that given by [Tao and Dray \(2008\)](#), [Vu et al. \(2008\)](#) and more recently by [An and Faltinsen \(2013\)](#).

6.2.2.2 Mesh Generation.

In the same way as in the previous chapter, section 5.1.3, the flow assumption is considered as axisymmetric, and the meshes for the simulation of the flow induced by the oscillating vertical disk are generated in a 2D region. A brief description of the mesh characteristics is provided for each of the configuration types presented in Figure 6.10.

- **Type I Configuration.** An image of the mesh for this configuration is presented in Figure 6.11. As we can be seen, the grid is fully orthogonal, with progressive variation of the elements sizes.

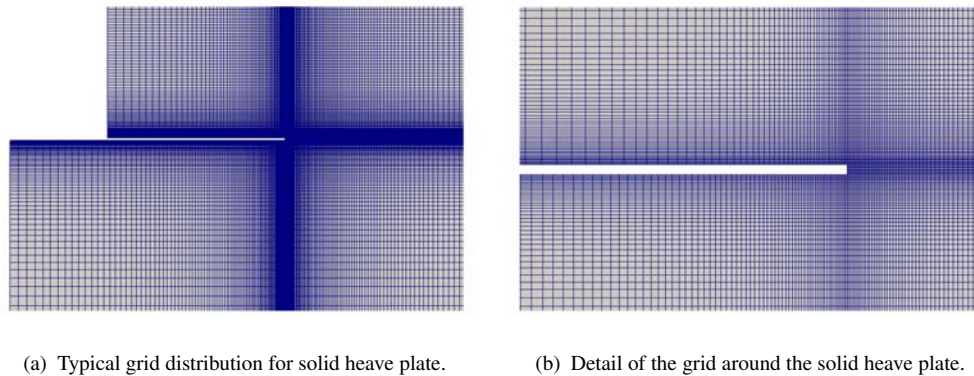


Fig. 6.11 Mesh generation for Type I configuration.

Here, the heave plate studied is a solid disc, and will serve as basis for comparison with the other configurations.

- **Type II Configuration.** Figure 6.12 shows the configuration mesh for the porosity case studied. Note that the hole region mesh is also refined.

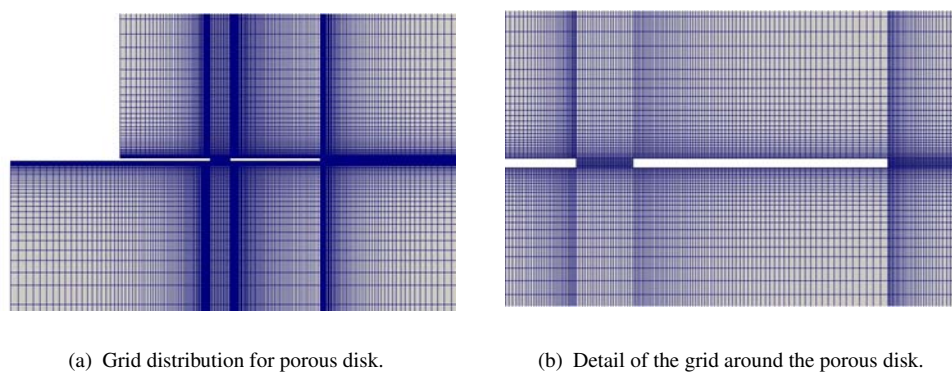


Fig. 6.12 Mesh generation for Type II configuration.

- **Type III Configuration.** Type III configuration comprises five different heave plates (see Fig. 6.10).

Figure 6.13 shows the meshes of the heave plate with Flap I, located just in the disc end.

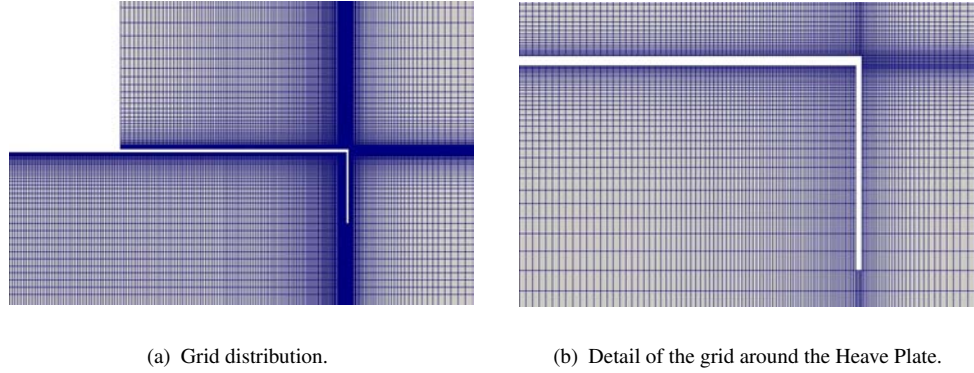


Fig. 6.13 Mesh generation for Type III configuration, Flap I.

Heave plate meshes with Flap II and III configuration are shown in Figures 6.14 and 6.15. The location of the flap is at 150 mm and 75 mm from the edge, respectively, as we can see in Fig. 6.10.

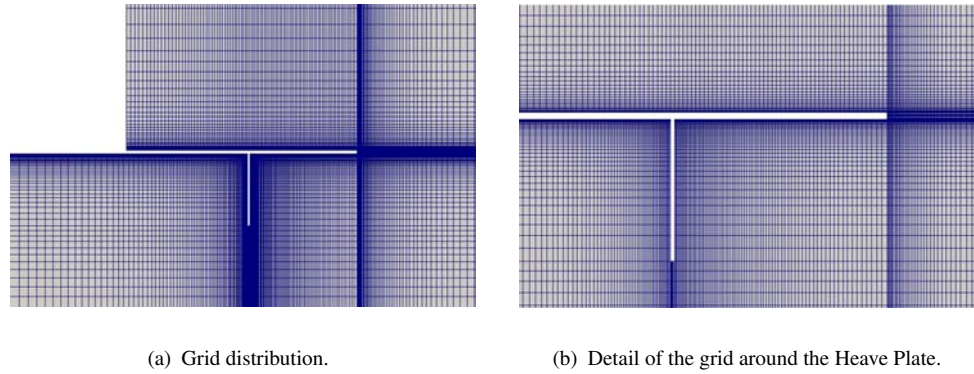


Fig. 6.14 Mesh generation for Type III configuration, Flap II.

Flap IV (Fig. 6.16) is located radially close to the central column radial position ($r/r_c = 1.13$), at a distance of 300 mm from the edge of the disc.

A variation of Type III configurations is shown in Fig. 6.17, in which the heave plate use the Flap I and 10% of porosity.

6.2.2.3 Convergence Analysis.

To assess the effects of the spatial and temporal resolutions on the calculated results and check numerical convergence, different meshes (Figs. 6.11 to 6.17) and different time-steps,

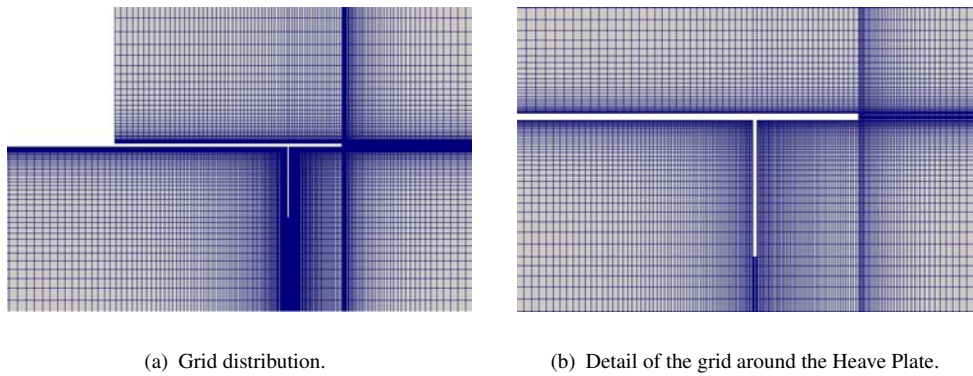


Fig. 6.15 Mesh generation for Type III configuration, Flap III.

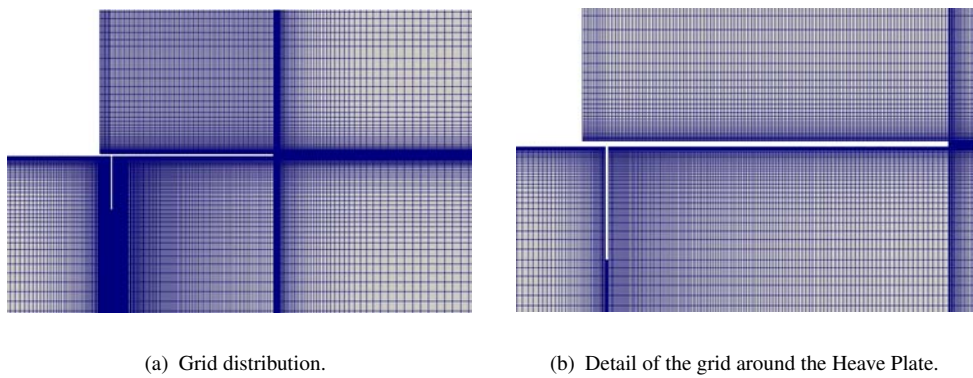


Fig. 6.16 Mesh generation for Type III configuration, Flap IV.

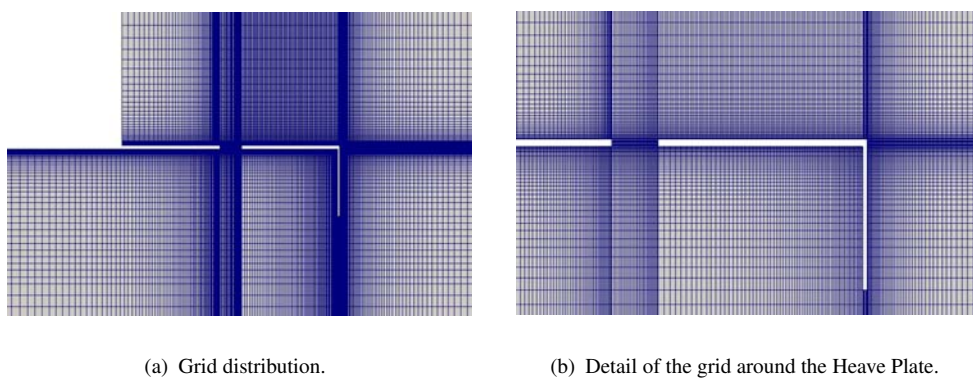


Fig. 6.17 Mesh generation for Type III configuration, Flap I and Porosity = 10% .

keeping the Courant Number (Eqn. 5.1) below 1.0, were investigated.

The details of the meshes are listed in Table 6.6. Y^+ value, computed as discussed in section 5.1.4.2.2, has been included, reading similar values as then.

Table 6.6 Test cases for the influence of the meshes.

	Mesh	Total number of cells
Poor mesh	100 x 250	25000
Coarser mesh	130 x 260	33300
Medium mesh	230 x 300	62400
Finer mesh	290 x 320	88900

The numerical results of force and drag coefficient, obtained from different meshes for $KC = 0.8796$, $\beta = 400000$ and $\Delta t = 1e^{-4}s$ are presented in Figure 6.18. It has been checked that $CFL < 1$ with this Δt for all cases analyzed.

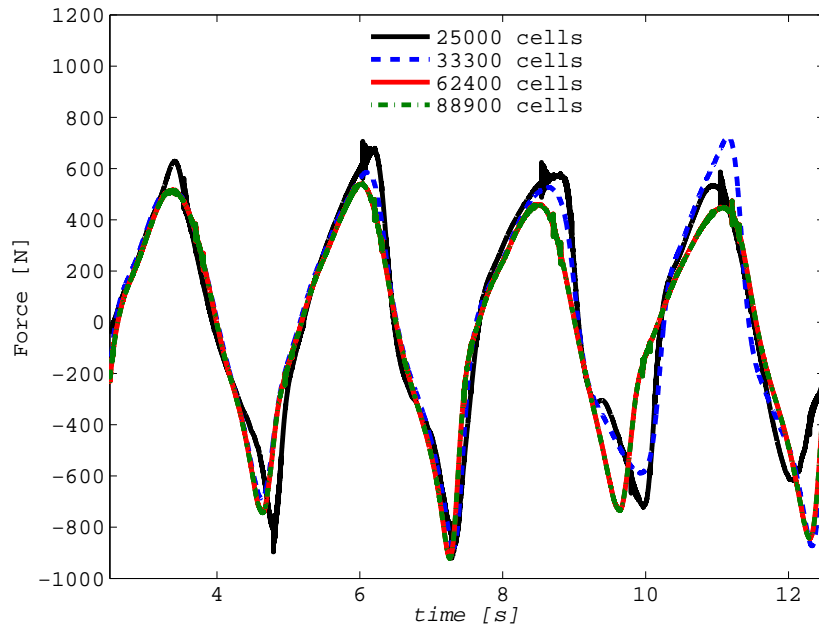
As can be seen in the Figure 6.18(a), the force amplitudes converge quickly. The finest mesh seems to present a smoother shape which is related with a force more concentrated in the frequency of the motion.

Figure 6.18(b) indicates that the medium resolution mesh provides a very similar value of the drag coefficient when compared to the one obtained with the finest mesh. Therefore, in order to minimized the computational effort, medium size mesh will be used.

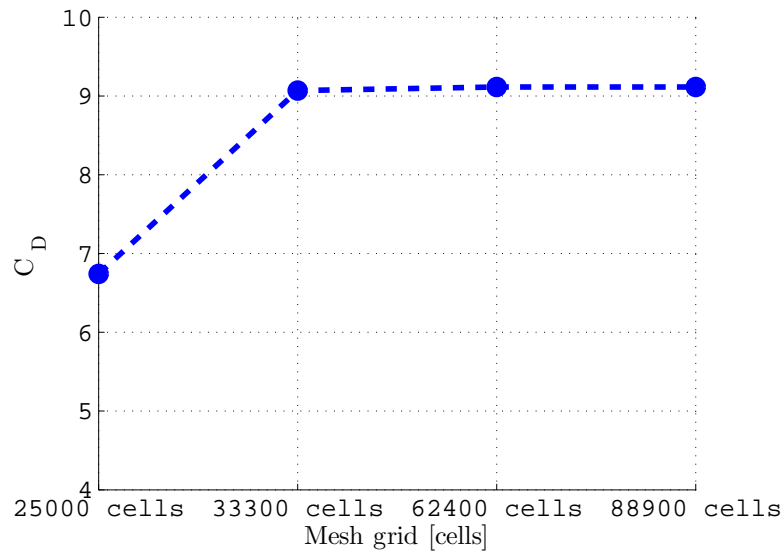
In order to determine a suitable time step, a number calculations for different time steps are carried out for the medium resolution mesh. Figure 6.19(a) shows a comparison between forces obtained for different time steps, while Figure 6.19(b) shows that the lowest time step considered may be required for the accurate calculation of the drag coefficient.

To take into account the near wall treatment as in Section 5.1.4.2.2 for the case when the heave plate is moving closer to the free surface, the meshes were generated in such a way that the cells are concentrated near the disk surfaces and stretched out gradually, with a minimum grid spacing of $0.0025 r_d$ around the sharp edges of the disc in radial and vertical directions, which leads a computational y^+ value, based on the cell size of approximately 3.7.

The simulations reported hereinafter were carried out with a mesh of 230×300 cells and a time-step of $1e^{-4} s$.

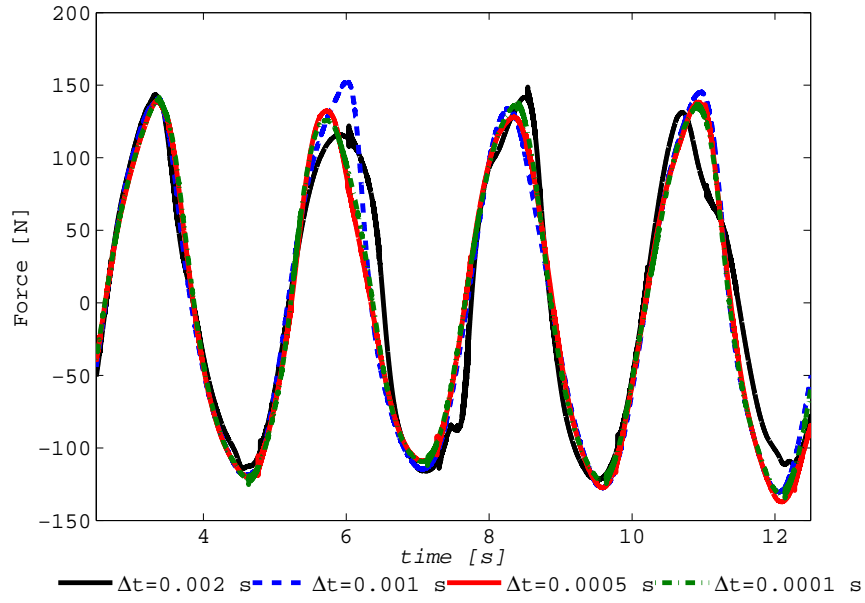


(a) Forces obtained for different meshes at $KC = 0.8796$ and $\Delta t = 1e^{-4} s$.

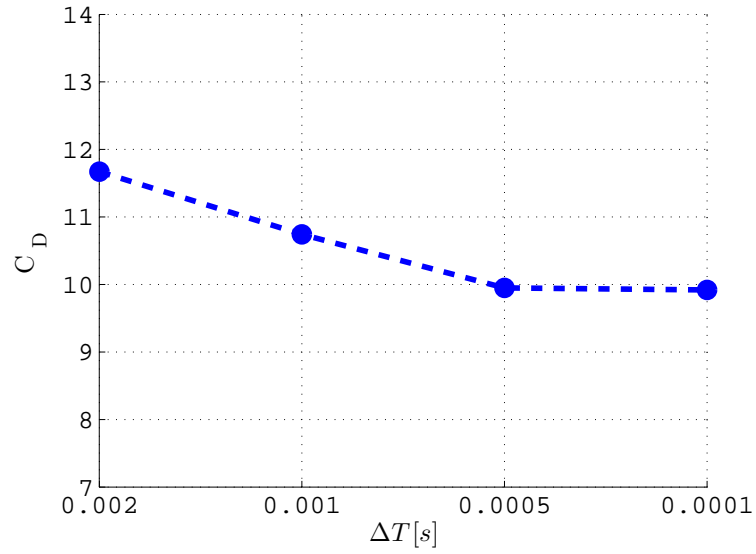


(b) Drag coefficient mesh convergence at $KC = 0.8796$ and $\Delta t = 1e^{-4} s$ using Eqn. (5.2).

Fig. 6.18 Convergence tests in mesh sizes.



(a) Forces obtained for different time step at $KC = 0.3142$ and 62400 cells.



(b) Drag coefficient time step convergence at $KC = 0.3142$ and 62400 cells using Eqn. (5.2).

Fig. 6.19 Convergence tests in Δt .

6.3 Results

6.3.1 General

Forced numerical oscillation analyses have been carried out numerically and compared with experiments. Heave added mass and damping coefficients have been obtained. The effects of the different parameters on these coefficients are summarized below.

In order to make non-dimensional the coefficients, theoretical added mass proposed by [Sarpkaya and Isaacson \(1981\)](#) has been modified to take into account the cylinder + disc configuration. For a configuration of a cylinder with a disk attached to its base, if the diameter of the disk is greater than that of the cylinder, there is only a part of the disk on the cylinder side producing added mass effect due to the presence of the cylinder (see Fig. 6.20). If we assume that the entrained fluid moves as an attached homogeneous mass, by neglecting the interference between the cylinder and disc, the added mass of a cylinder plus disc may be written as, ([Tao et al., 2007](#)):

$$M_1 a = \rho / 12 (2D_d^3 + 3\pi D_d^2 g - \pi^3 g^3 - 3\pi D_c^2 g), \quad (6.1)$$

where $g = 1/\pi \sqrt{D_d^2 - D_c^2}$, D_d and D_c are the heave plate and cylinder diameter, respectively. So, the theoretical added mass can be corrected by accounting for the cylindrical column volume.

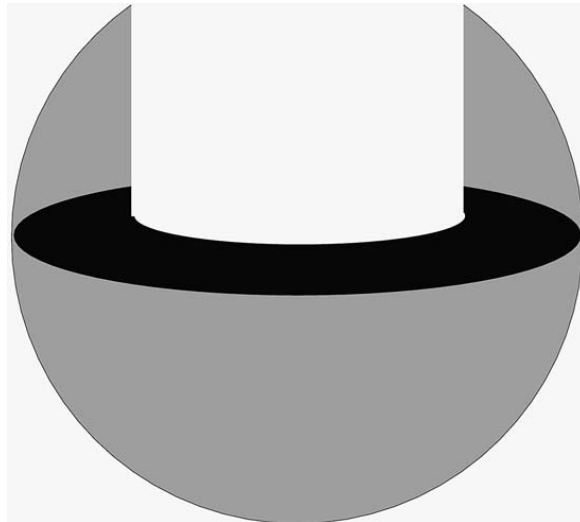


Fig. 6.20 Added mass of a disc attached to a cylinder. Source: [Tao and Cai \(2004\)](#).

6.3.2 Solid heave plate: influence of flow parameters KC , β and submergence of the heave plate s/r_d

6.3.2.1 General

It is noticed from the measured and calculated data that the added mass and damping coefficients have negligible dependence upon frequency of oscillation at different KC number as shown in Figs. 6.21 and 6.22, which is a consequence of small free-surface wave generation.

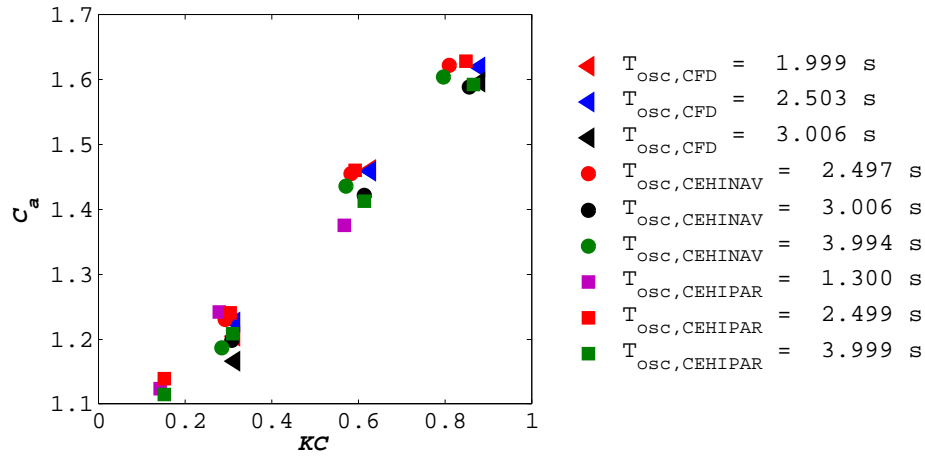


Fig. 6.21 Added mass with varying frequencies at $1.55r_d$ below mean free surface.

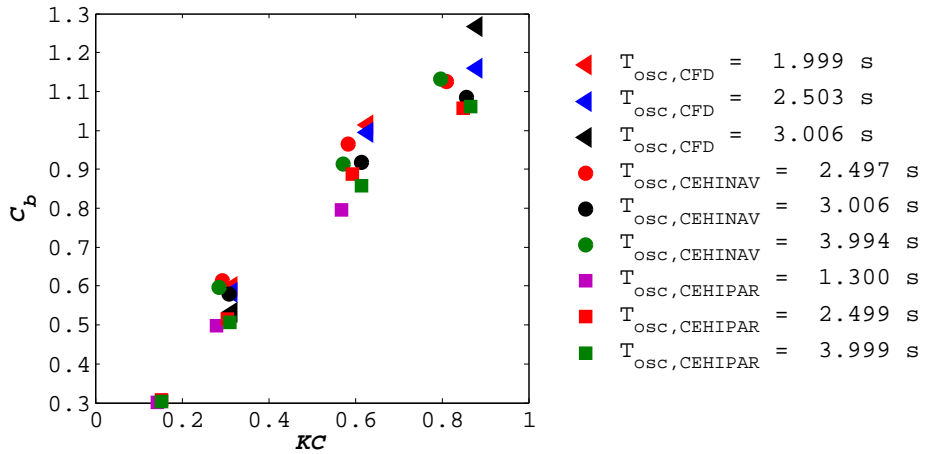


Fig. 6.22 Damping with varying frequencies at $1.55r_d$ below mean free surface.

It can also be seen in figures above, that there is generally satisfactory agreement between simulations and experiments with very slight difference at large KC .

The KC number (Eqn. 4.29) characterises the amplitude of heave motion relative to the diameter of the disc. Figures 6.23 and 6.24 show the numerical prediction of the influence of the KC number on the hydrodynamic characteristics of a solid heave plate oscillating harmonically in still water at different submergences at a heave period of 2.5 s.

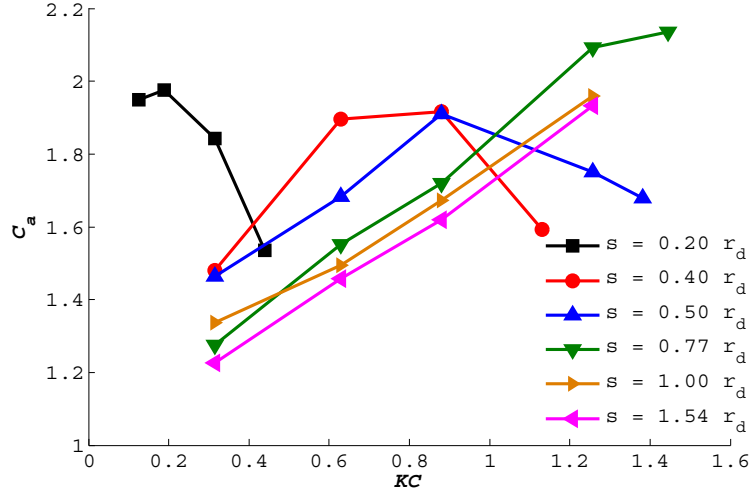


Fig. 6.23 Variation of added mass coefficient with KC for a solid heave plate oscillating at different submergences. $T = 2.5s$. Numerical results.

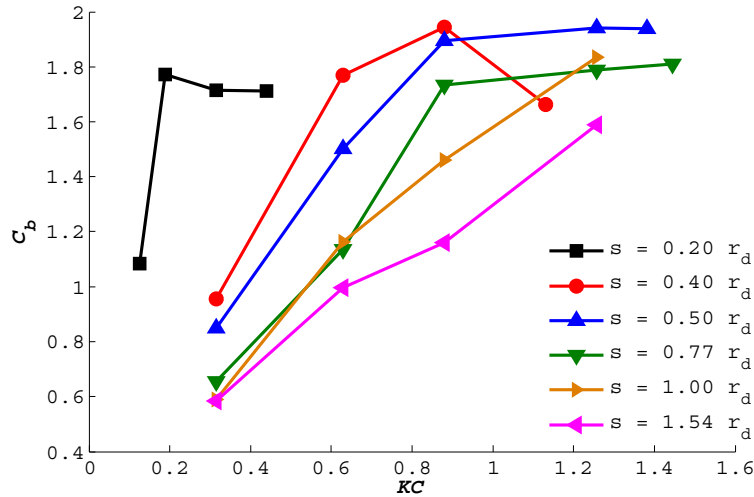


Fig. 6.24 Variation of damping coefficient with KC for a solid heave plate oscillating at different submergences. $T = 2.5s$. Numerical results.

As can be seen in Figs. 6.23 and 6.24, for large submergences ($h \geq r_d$) the added mass and damping coefficients increase with increasing KC number and a nearly linear relationship

between them is found. On the other hand, the coefficients have a change in their behavior when the heave plate oscillates closer to the free surface above a certain KC_{crit} number.

Figure 6.25 shows the comparison of the hydrodynamic coefficients against experimental data for different depths. Good agreement is found between the experimental data and the present results obtained for the added mass and damping coefficients.

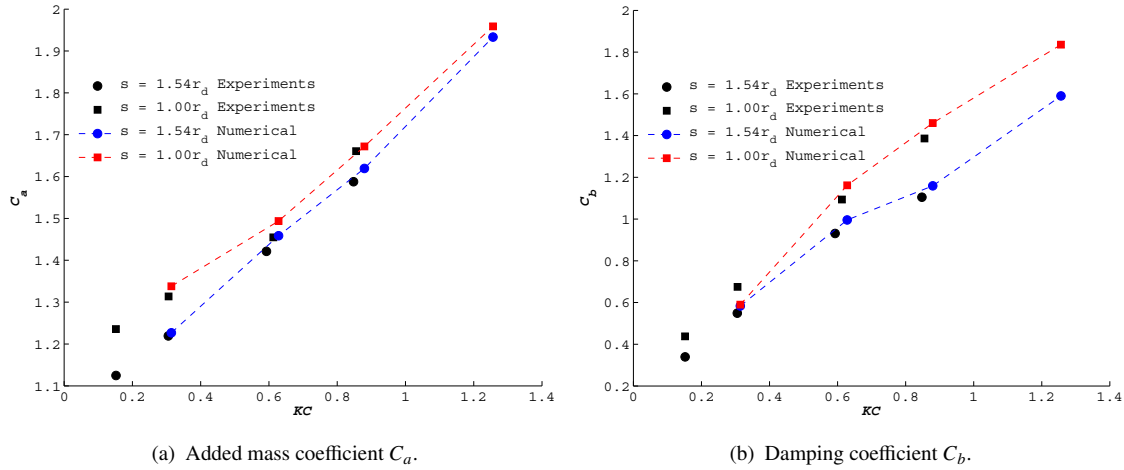


Fig. 6.25 Comparison of added mass and damping coefficients with experimental results. $T = 2.5s$.

It is interesting to compare these results with those obtained in chapter 5, section 5.2.4 for a single disc oscillating close to a free surface. Fig. 6.26 shows a comparison of the hydrodynamic coefficients between a ‘cylinder + disc’ and ‘only a disc’. The added mass coefficient presents similar values for large submergences, in contrast to the damping coefficient in which the cylinder + disc configuration leaves more damping. This behavior is attributed to the fact that the thickness-to-diameter ratio has significant influence on hydrodynamic damping (He et al., 2008; Tao and Thiagarajan, 2003b). A significant reduction in damping is observed as thickness-to-diameter ratio increases. There is a slight dependence of the added mass on the thickness-to-diameter ratio, but significantly less than that for the damping.

6.3.2.2 C_a and C_b fitting

Table 6.7 shows the values of slope and offset of curve fits for C_a and C_b . The slope shows a decrease trend as we move down the table to deeper submergences. The offset is also affected, varying from a value less than 2.0 to about 1.0. The slope and offset of the damping coefficient curve also show similar trends with increasing submergence.

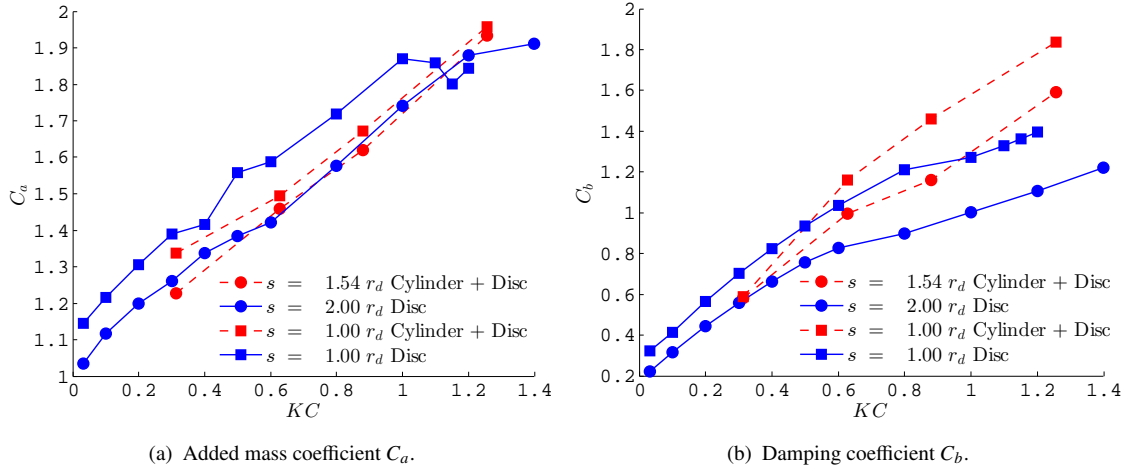


Fig. 6.26 Comparison of added mass and damping coefficients for an oscillating cylinder + disc and only a disc. Cylinder + disc, $t_d/D_d = 1/200$, $T = 2.5s$. Disc, $t_d/D_d = 1/100$, $T = 1.0s$.

Table 6.7 Slope and offset of curve fits for numerical C_a and C_b .

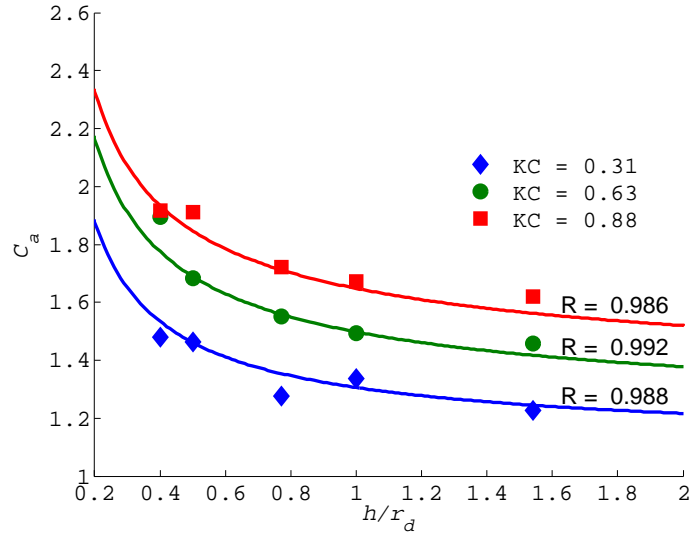
Submergence s	C_a		C_b	
	Slope ($\partial C_a / \partial KC$)	Offset	Slope ($\partial C_b / \partial KC$)	Offset
$0.2 r_d$	0.436	1.949	10.95	1.083
$0.4 r_d$	1.320	1.481	2.592	0.956
$0.5 r_d$	0.785	1.464	1.856	0.849
$0.77 r_d$	0.790	1.276	1.896	0.654
$1.0 r_d$	0.665	1.338	1.551	0.590
$1.54 r_d$	0.743	1.227	1.039	0.538

Plotting C_a and C_b vs. submergence in Figure 6.27 shows that the slope and offset change quite dramatically for very shallow submergence, but flatten out as we move further away from the free surface. In general for each KC the slope decreases continuously as the heave plate oscillates at higher submergences s/r_d from the free surface. By approximating the slope and offset using an Excel's tool for a power regression analysis, we found power formulae that express C_a and C_b in terms of s/r_d for each $KC \leq KC_{crit}$ value, equations (6.2) and (6.3).

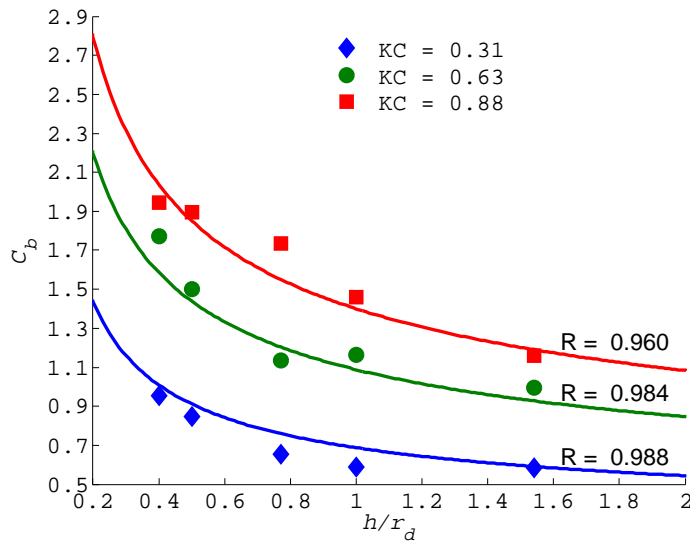
$$C_a = 0.60 \left(\frac{s}{r_d} \right)^{-0.25} KC + \frac{0.12}{\frac{s}{r_d}} + 1.0, \quad (6.2)$$

$$C_b = 1.25 \left(\frac{s}{r_d} \right)^{-0.40} KC + \frac{0.1}{\frac{s}{r_d}} + 0.2. \quad (6.3)$$

These expressions can be used to evaluate the added mass and damping closer to the free surface for $s/r_d \leq 2$ with correlation coefficient R greater than 0.96. Beyond this submergence, deep water condition is seen to be the best fit. This condition is the consequence of the fact that the added mass approaches its theoretical value expressed by $8/3\rho r_d^3$ for a disc (Korobkin, 2009) and by Eqn. 6.1 for a cylinder+disc (Tao et al., 2007), when $KC \rightarrow 0$.



(a) Added Mass Coefficient C_a using Eqn. (6.2).



(b) Damping Coefficient C_b using Eqn. (6.3).

Fig. 6.27 Variation in hydrodynamic coefficients with submergence ' s/r_d ' at varying KC numbers. $T = 2.5s$. Numerical results.

6.3.2.3 Comparison with other authors

Heave added mass and damping coefficients of solid plates with varying submergences have been experimentally examined by [Molin et al. \(2008\)](#).

Figure 6.28 shows the experimental and numerical added mass and damping dependence on KC number. The numerical results show a good agreement with the experimental data conducted by [Molin et al. \(2008\)](#) for large oscillation period, but there exists an important difference in added mass for lower oscillation periods. The weak dependence of C_a on KC for [Molin et al. \(2008\)](#) experiments is remarkable and challenges our own results and those of e.g. [Tao and Dray \(2008\)](#).

The differences are probably due to the different geometric characteristics used by the authors. Molin performed experiments with smaller (and thinner) disc (diameter 60 cm; thickness 1 mm) compared to our disc (diameter 100 cm; thickness 5 mm) and the disc used by [Tao and Dray \(2008\)](#) (diameter 40 cm; thickness 8 mm). Smaller damping values obtained by Tao are attributed to the greater thickness-diameter ratio (t_d/D_d), parameter that as was previously mentioned affect the damping coefficient.

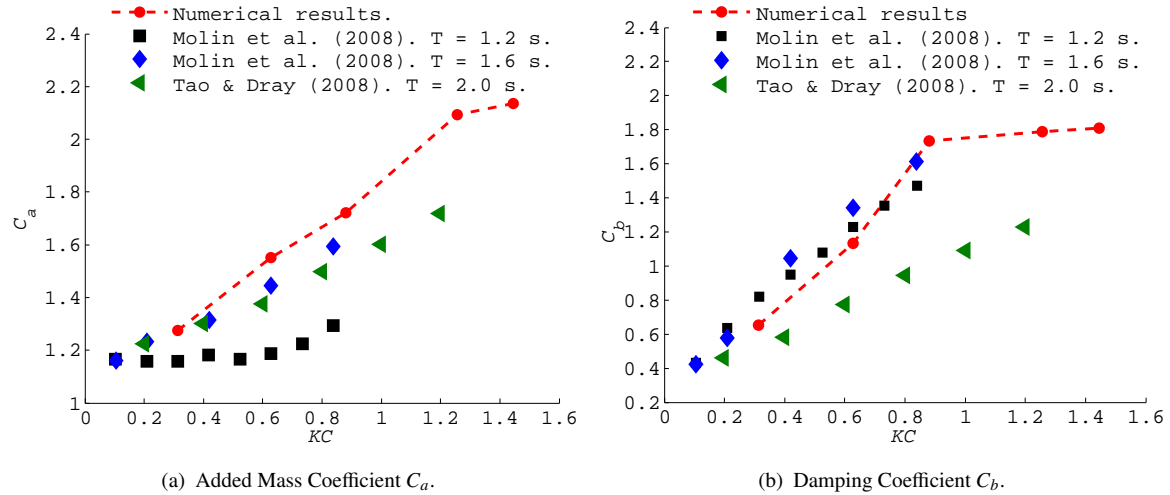


Fig. 6.28 Comparison of added mass and damping coefficients for solid heave plate. red line: Present work, $s/r_d = 0.77$ and $T = 2.5$ s. black squares: [Molin et al. \(2008\)](#), $s/r_d = 0.83$ and $T = 1.2$ s.

6.3.3 Sensitivity study of scale effects

Two set of experiments have been carried out in different facilities in order to verify the reliability of the measurements in the scale analysis. Frequency is made, for the graphs,

non-dimensional with the theoretical heave resonance frequency of the platform, whose value at model scale is:

$$w_r = \sqrt{\left(\frac{\rho g S_w}{M + M_{1a}}\right)}, \quad (6.4)$$

where S_w is the water-plane area. The corresponding prototype period ($2\pi/w_r$) is 17.9 s, which is above common operational first order excitations. The periods to be analyzed have been chosen below this value. It is remarkable that without the heave plate, the natural heave period would be 9 s, a value well within typical operational sea states, something that would surely penalize operations by increasing the platform downtime.

Figs. 6.29 and 6.30 show a hydrodynamic coefficient comparison three between different scales (see Fig. 6.5) of the semi-submersible model. As can be seen the results obtained experimentally from models of different scales are quite comparable. This is an encouraging result, considering that this data needs to be used for prototype design and it seems that assuming constant values for C_a and C_b is a reasonable extrapolation hypothesis.

6.3.4 Influence of the shape of the heave plate: flaps

This section discusses the influence of the plate edge geometry on the heave response. Several alternative heave plate edge shapes proposed in Fig. 6.7 have been tested. The presence of flaps has opposite effects in the heave added mass and damping coefficients, as shown in Figs. 6.31 and 6.32. They increase added mass when compared to the plain plate but significantly reduce damping too. This behaviour is due to the influence of the thickness-to-diameter ratio, causing a reduction in the damping coefficient as the t_d/D_d increases as was previously mentioned.

Numerical simulations on five plates with flaps (see Fig. 6.10 and Table 6.5) were also carried out and the results were compared with the solid plate, to examine the influence of variations on Flap 4.3 on the hydrodynamics. The added mass and damping coefficients of these plates obtained numerically, are shown in Figure 6.33. It can be seen that the plate with Flap I yields the greatest added mass but the lowest damping coefficient, while when the flap is moved to the center of the heave plate the values of C_a and C_b are quite similar to the hydrodynamic coefficients of the solid plate.

In the behaviour of the heave plate with Flap I and 10% of porosity, the added mass (Fig. 6.33(a)) decreases compared to the solid plate and plate with Flap I, due to the flow through the porosity. Figure 6.33(b) shows that damping coefficient C_b for the heave plate with ‘Flap I 10% Porosity’ is larger compared to the heave plate with Flap I, but does not improve the

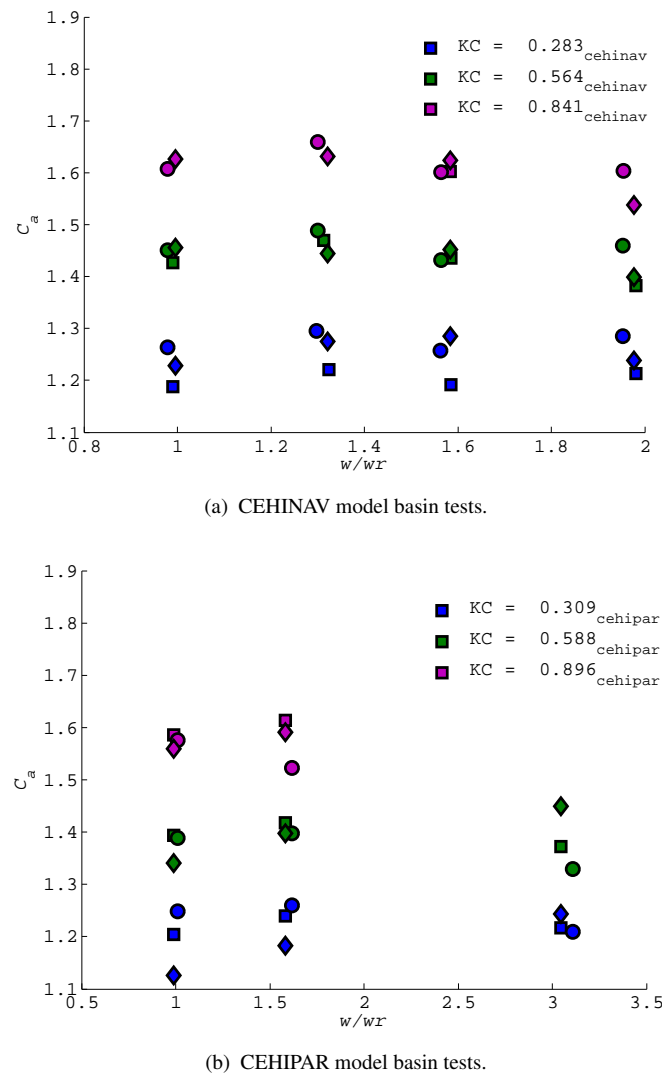
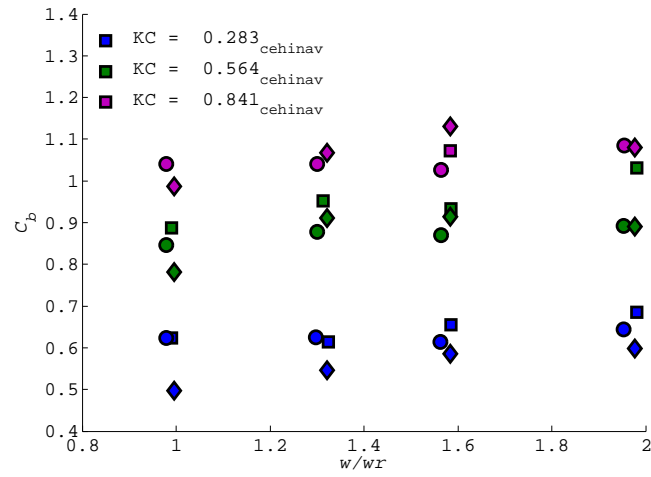


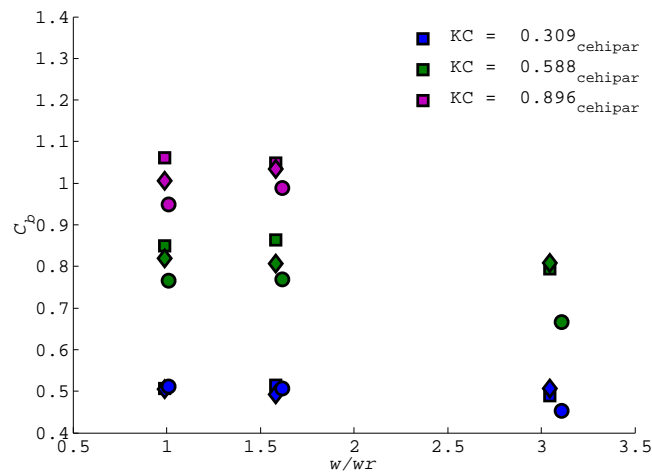
Fig. 6.29 Scale and frequency dependence tests of added mass coefficient. $s/r_d = 1.55r_d$. squares: Scale 1 : 20. circles: Scale 1 : 27.6. diamonds: Scale 1 : 45.45.

performance of the solid plate.

Fig. 6.34 shows a comparison of the hydrodynamic coefficient obtained experimentally and numerically, for the heave plate with flap 4.3 configuration. Good agreement between both results was found.



(a) CEHINAV model basin tests.



(b) CEHIPAR model basin tests.

Fig. 6.30 Scale and frequency dependence tests of damping coefficient. $s/r_d = 1.55r_d$. squares: Scale 1 : 20. circles: Scale 1 : 27.6. diamonds: Scale 1 : 45.45.

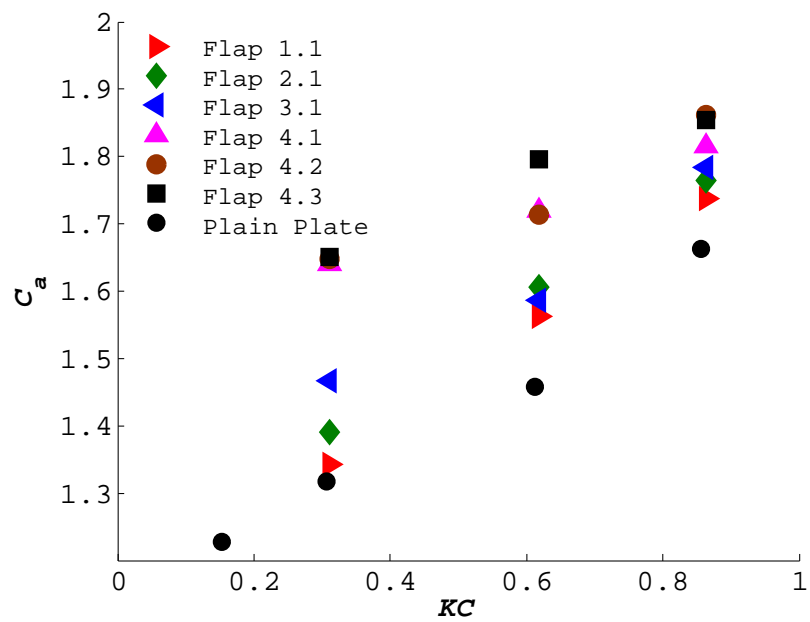


Fig. 6.31 Experimental added mass coefficients for heave plate with flaps (see Fig. 6.7 for flap type description).

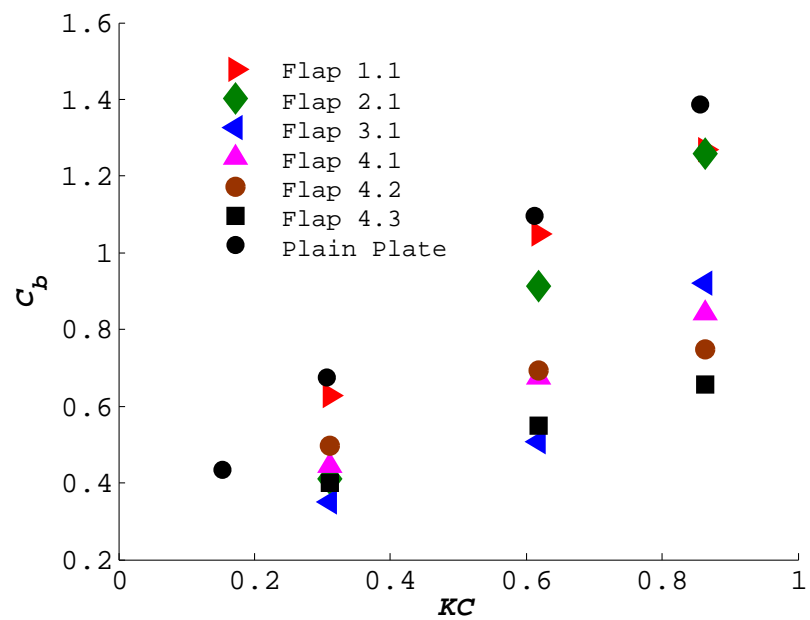
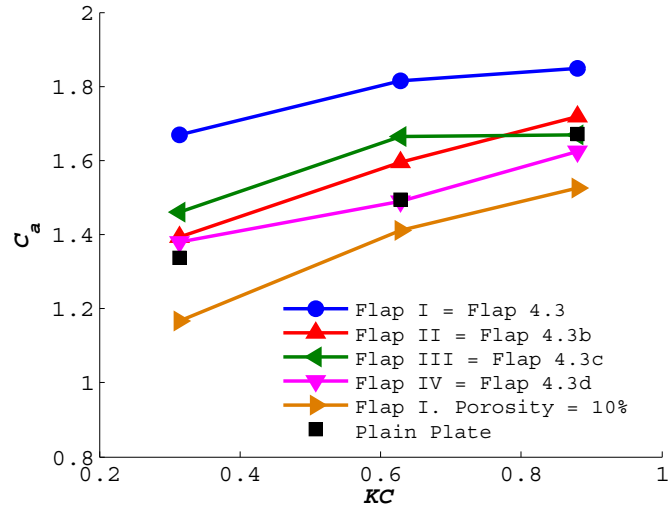
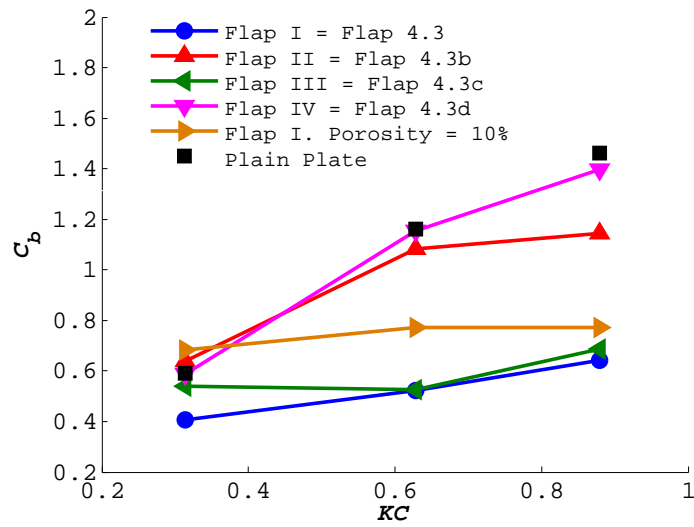
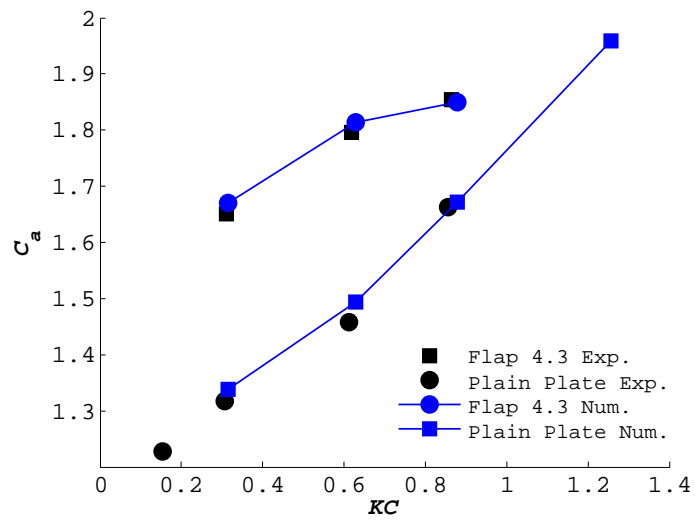
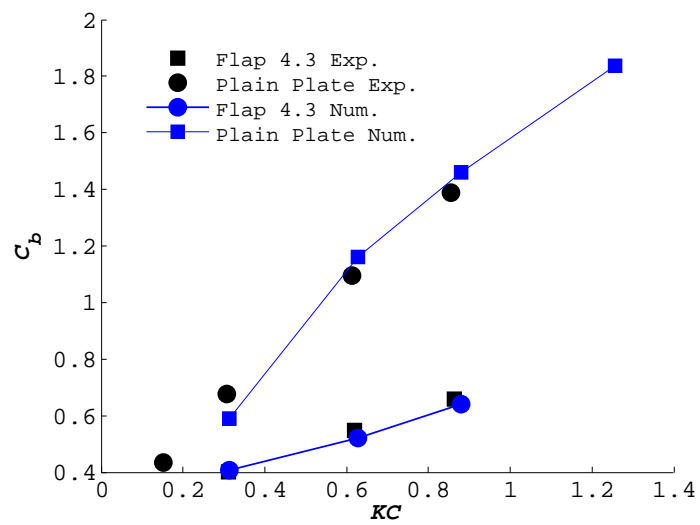


Fig. 6.32 Experimental damping coefficients for heave plate with flaps (see Fig. 6.7 for flap type description).

(a) Added Mass Coefficient C_a .(b) Damping Coefficient C_b .**Fig. 6.33** Added mass and damping coefficients for heave plate with flaps (Numerical results).



(a) Added Mass Coefficient C_a .



(b) Damping Coefficient C_b .

Fig. 6.34 Comparison of added mass and damping coefficients for heave plate with flaps.

6.3.5 Influence of the heave plate porosity

6.3.5.1 General

This section investigates the hydrodynamic characteristics of oscillatory porous discs using numerical modelling. The sensitivities of the added mass and damping coefficients to both motion amplitude and the disc porosity are examined.

The heave plates have perforated openings that fit the vertical risers and these openings play an important role in tuning the hydrodynamics of the heave plates. The present study concerns simulations on three plates with perforation ratios of 5%, 10% and 10%, respectively. The results are shown in Figs. 6.35 and 6.36, and the hydrodynamic coefficients of the solid plate are also given in those figures for comparison.

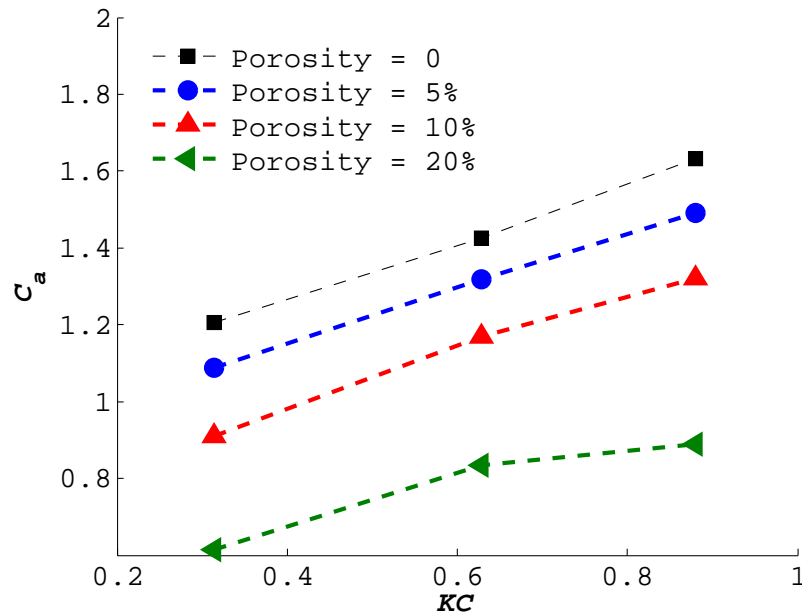


Fig. 6.35 Comparison of added mass coefficient for solid and porous plates (Numerical results).

$$T = 2.5s \text{ and } s = 1.55r_d.$$

Because the fluid can pass through the openings, it is reasonable that the added mass coefficient decreases with increasing perforation ratio. As can be seen in Figure 6.35, all discs simulated exhibit a linear increase in added mass coefficient with increasing KC values. The results show that the solid disc evidently produces the highest added mass, throughout the KC number range, followed by the 5%, 10% and 20% porous discs, respectively. This is a clear indication that added mass is significantly penalised by the porosity. Natural period (Eqn. (4.32)) will be reduced which may be problematic in case it comes closer to that of the extreme or operational waves.

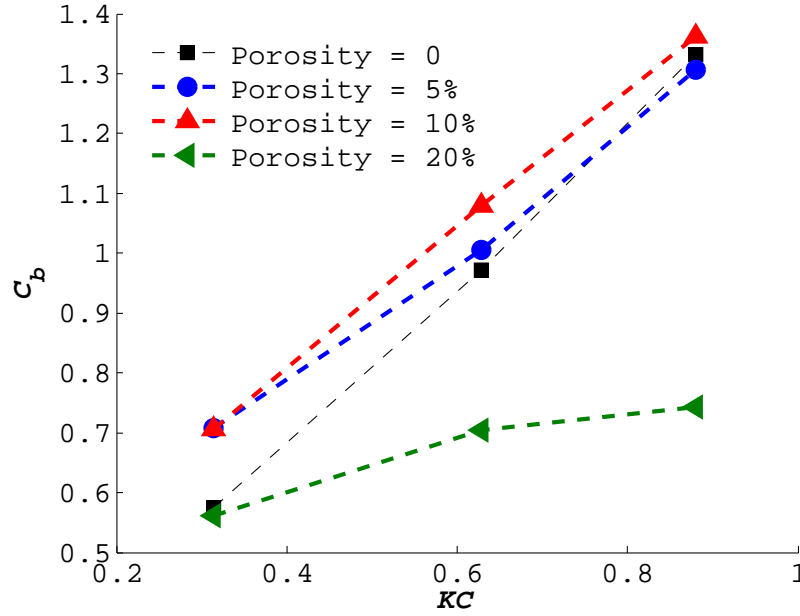


Fig. 6.36 Comparison of damping coefficient for solid and porous plates (Numerical results).
 $T = 2.5s$ and $s = 1.55r_d$.

Figure 6.36 shows that the discs with 10% of porosity yield the greatest damping. However, the damping coefficient of the heave plate with 5% of porosity are quite similar to the solid disc values as KC increases. Molin (2001) concluded that the heave damping can be increased by a factor 4 or 5 by making the heave plate porous with a porosity slightly below 20%. It should be noted that his calculation was based on potential flow assumption, and the analytical solution may yield appropriate values for the damping only if the effect of separation through the openings is dominant compared to the effect of separation and vortex shedding due to the disc edge. The increase in C_b due to porosity found in our simulations is far from his predictions.

Figure 6.36 shows that the disc with 20% porosity yields approximately the same value in damping compared to solid disc at $KC = 0.314$, but clearly under performs all the other discs when the KC increases, maybe due to increased of the opening area ratio, whereby the flow through the perforations reduces the pressure difference between the top and bottom sides of the plate and thus the circulation on generation of vorticity at the plate edges, resulting in a reduction in heave damping. Figure 6.36 also shows that the optimum porosity, in regards to C_b , appears to be between 5% and 10% at low KC numbers. As the KC number increases, such influence appears to diminish. The damping coefficient of these plates with different perforation ratios are nearly identical to each other at $KC > 1.0$, which is quite consistent with the results of Molin (2001) who reported that no extra damping can be gained by

making the plate porous when the KC number is larger than 1.0.

6.3.5.2 Comparison with other authors

A comparison in order to validate the way that the porous disc was modelled is presented in Figs. 6.39 and 6.40. The authors selected for comparison regarding porous plates are [Tao and Dray \(2008\)](#) and [An and Faltinsen \(2013\)](#). The comparison is cumbersome since porosity is numerically modelled assuming axisymmetric flow and incorporating it in the geometry as rings with equivalent surface. In actual experiments, [Tao and Dray \(2008\)](#) perforated a plate with regularly distributed holes amounting the targeted porosity ratio (see Fig. 6.37). [An and Faltinsen \(2013\)](#) used a similar technique but considered squared plates (Fig. 6.38), which makes the comparison interesting but even more questionable



Fig. 6.37 Solid and porous discs used by [Tao and Dray \(2008\)](#). Source: [Tao and Dray \(2008\)](#).

Figures 6.39 and 6.40 show that although the numerical simulations reproduced well the tendencies, the damping coefficient is over-predicted.

The differences may be due to different submergence ratios as well as the aforementioned difference in how the porosity is numerically and experimentally achieved.

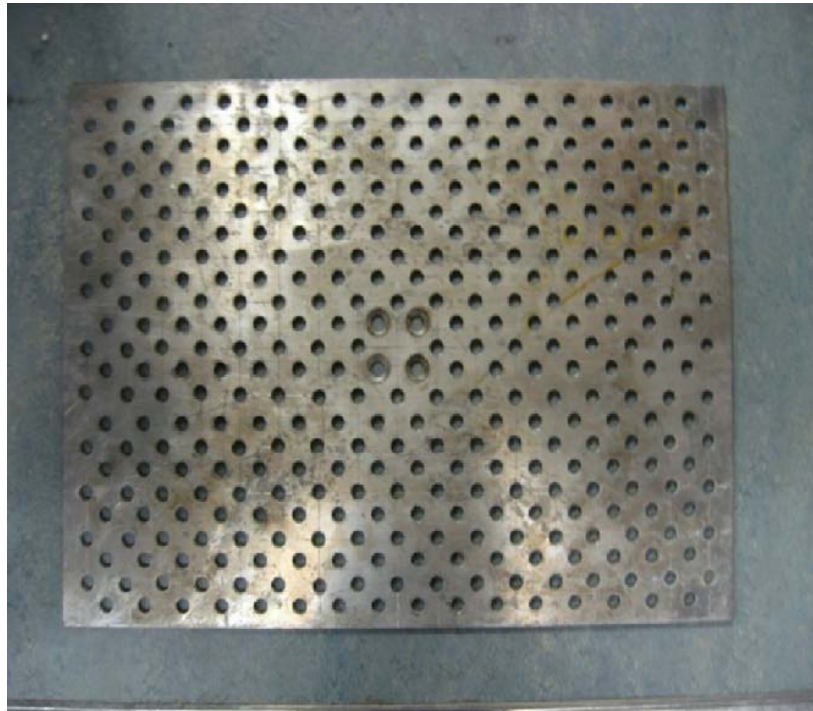


Fig. 6.38 Porous disc used by [An and Faltinsen \(2013\)](#). Source: [An and Faltinsen \(2013\)](#).

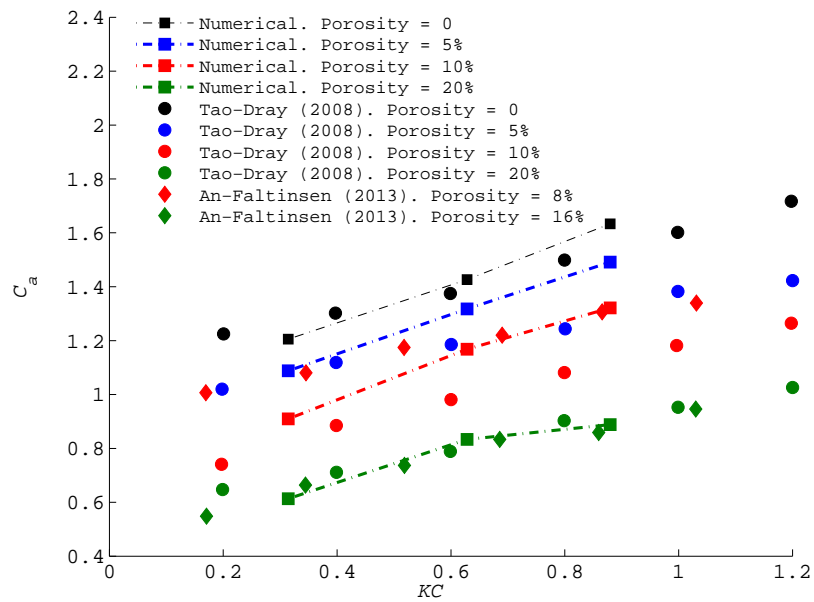


Fig. 6.39 Added mass comparison between numerical and experimental results of porous plates.
squares: Present work, $T = 2.5s$ and $s = 1.8r_d$. circles: [Tao and Dray \(2008\)](#), $T = 2.0s$ and $s = 3.0r_d$.
diamonds: [An and Faltinsen \(2013\)](#), $T = 2.5s$ and $s = 2.85r_d$.

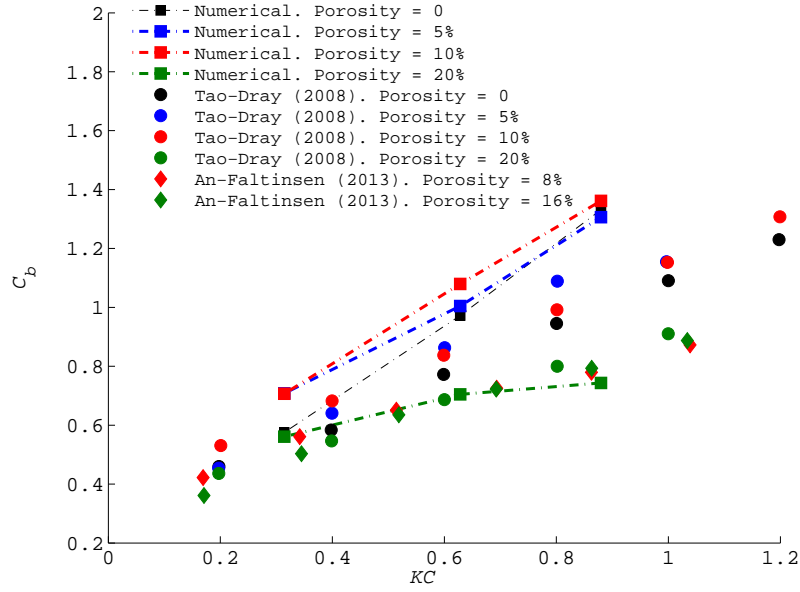


Fig. 6.40 Damping comparison between numerical and experimental results of porous plates. squares: Present work, $T = 2.5s$ and $s = 1.8r_d$. circles: **Tao and Dray (2008)**, $T = 2.0s$ and $s = 3.0r_d$. diamonds: **An and Faltinsen (2013)**, $T = 2.5s$ and $s = 2.85r_d$.

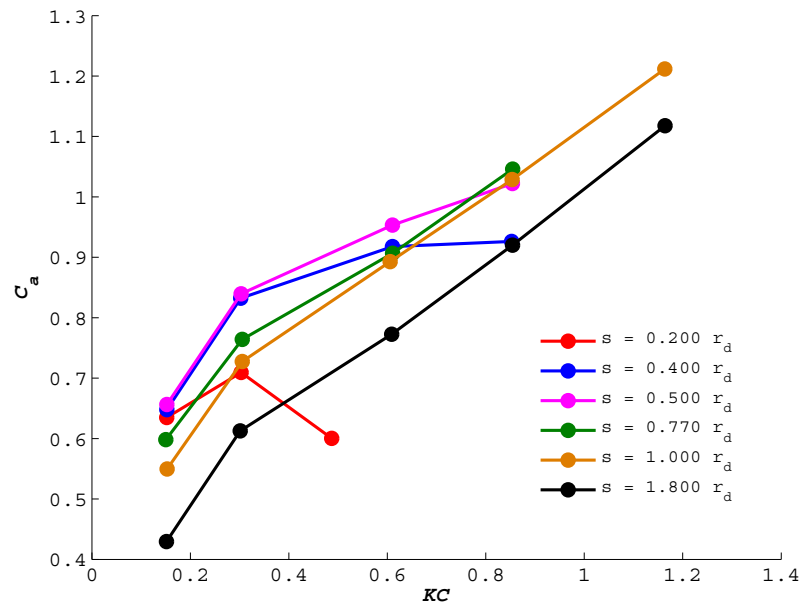
6.3.6 Fractal plate

6.3.6.1 General

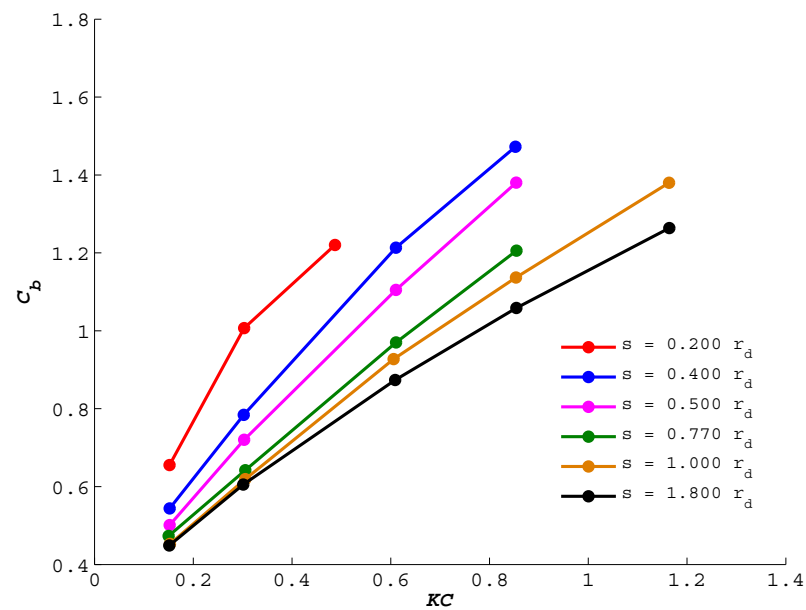
This section discussed the experimental results obtained for the novel fractal heave plate design introduced in section 6.2.1.3.4. No numerical results are yet available for present design.

Figure 6.41 gives the variation of the added mass and damping coefficients at different submergences with KC number. As can be seen in Fig. 6.41(a), when the plate is oscillating to depths greater than $0.5 r_d$ the submergence has little influenced of added mass showing similar results with a slight variation in slope, although there is a change in the behaviour of C_a for small submergences. Figure 6.41(b) shows that the C_b increases when the submergence decreases and there is a nearly linear relationship between C_b and KC .

Figure 6.42 shows the comparison of the hydrodynamic coefficients of Fractal Plate and Solid one for submergences $s = 1.0r_d$ and $s = 0.5r_d$. As can be seen, the fractal plate shows a similar trend in the behaviour of the coefficients with the solid plate, increasing the values of C_a and C_b with the KC number, but under performs the characteristics of the solid plate, maybe due to large porosity used.

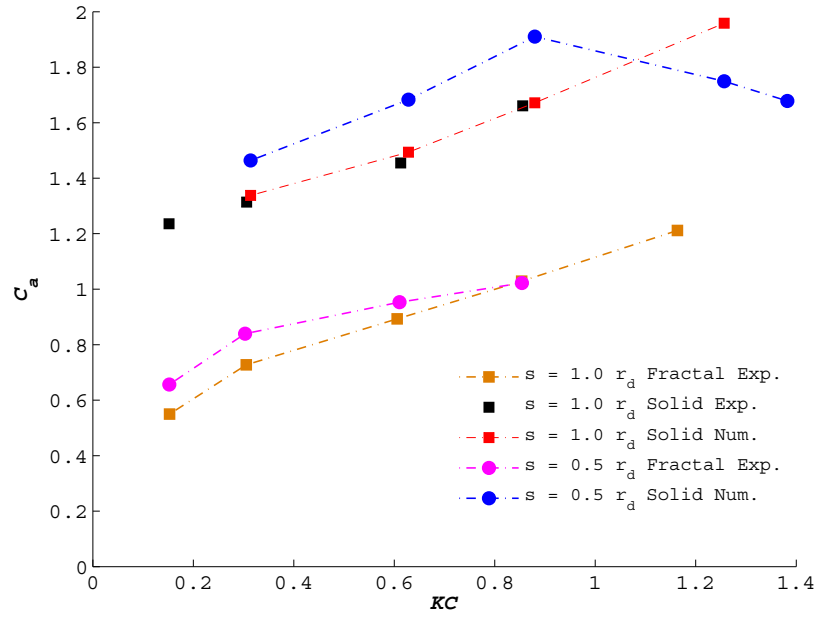
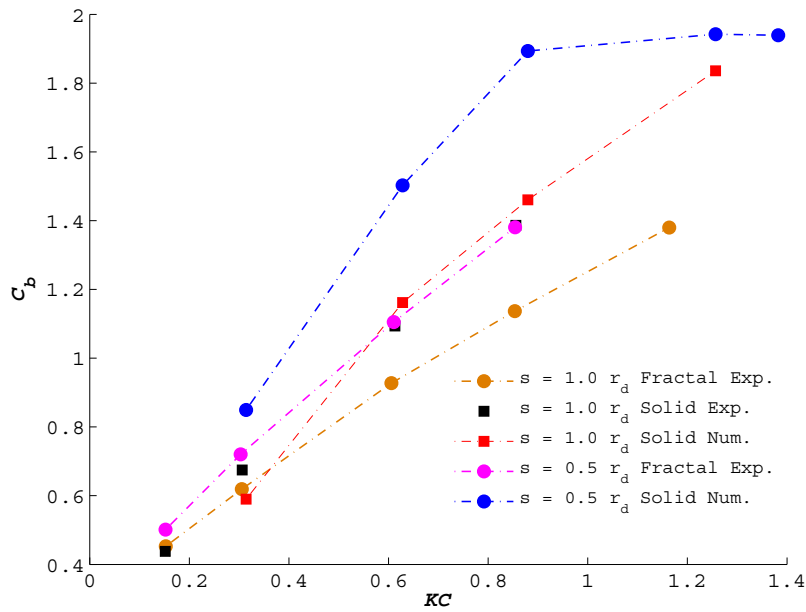


(a) Added Mass Coefficient C_a .



(b) Damping Coefficient C_b .

Fig. 6.41 Variation of hydrodynamic coefficients with KC for a fractal heave plate oscillating at different submergences.

(a) Added Mass Coefficient C_a .(b) Damping Coefficient C_b .**Fig. 6.42** Comparison of added mass and damping coefficients for solid plate and fractal plate.

6.3.6.2 Comparison between numerical and experimental results by other authors

Molin et al. (2008) also conducted a series of experiments with perforated plates. Figure 6.43 shows the comparison of the added mass and damping coefficients for two different submergences ratio. Strong differences are observed for the coefficients between fractal plate and experiments carried by Molin. It should be noticed that our results present the same behaviour that these found by Molin, and the discrepancies presumably are due to the different value of the diameter and thickness, and mostly due to the fact that the fractal plate has various holes sizes.

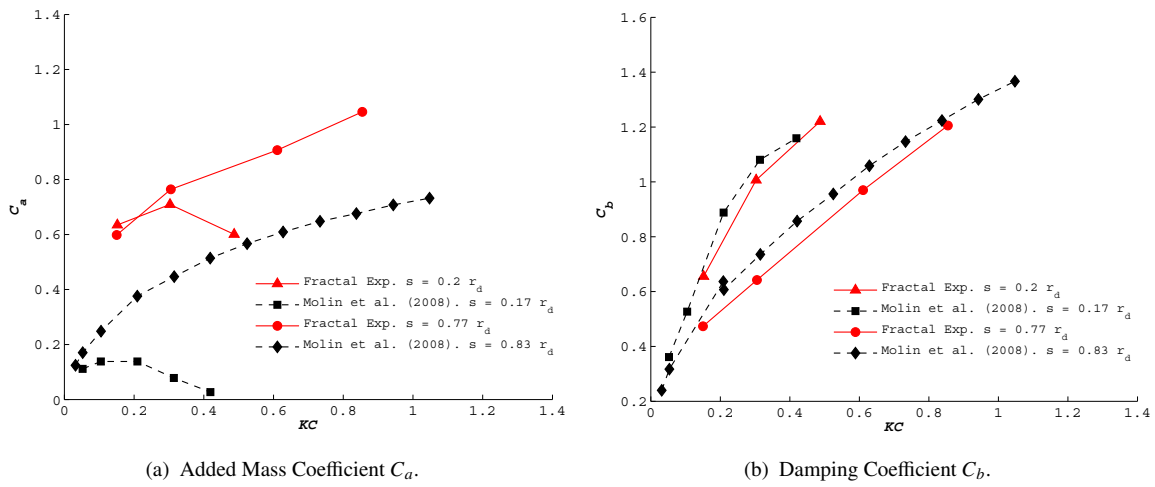


Fig. 6.43 Comparison of added mass and damping coefficients for 20% Porosity heave plate. red line: Present work, $T = 2.5s$. black line: Molin et al. (2008), $T = 1.6s$.

Recently, An and Faltinsen (2013) conducted, in a range of submergences, forced harmonic heave motions tests of horizontally perforated rectangular plates. Figure 6.44 shows the experimental heave added mass and damping coefficients versus KC number, obtained for the fractal plate (see Fig. 6.8) and compared with the results obtained by An and Faltinsen. Both set of data correspond to a submergence of approximately $s/r_d = 0.4$, where the presence of the free surface starts to influence the dynamics. Figure shows that our results and these obtained by An and Faltinsen (2013) have a disagreement in value, but present the same behaviour for different KC number. Note, that here, the fractal plate has 20% of porosity, while the rectangular disk (other characteristic for this difference) used by An and Faltinsen has 15.89% of porosity. Even with larger porosity the fractal plate displays larger added mass and damping performance.

Finally, in Fig. 6.45, the fractal plate is compared to Tao and Dray (2008) same porosity (20%) experimental results corresponding to deep water condition. It can be noticed that

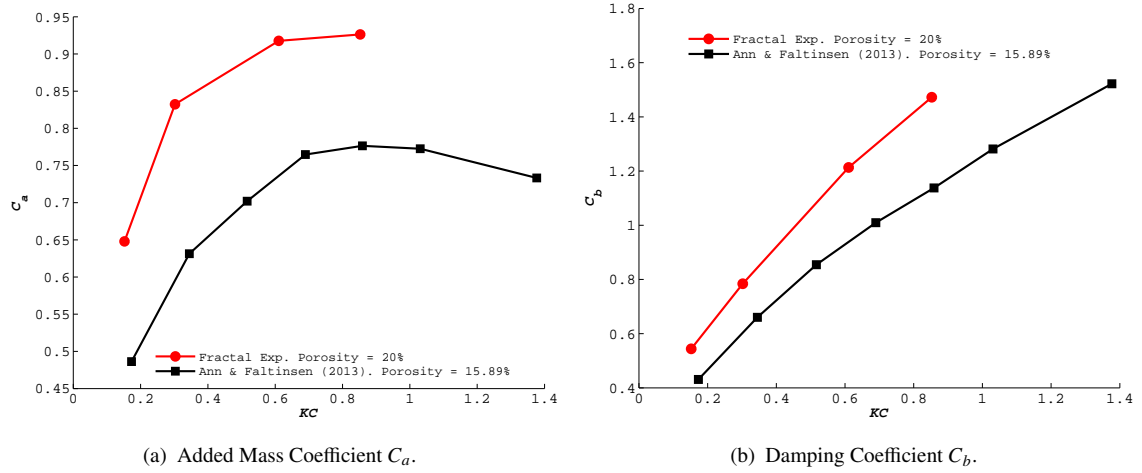


Fig. 6.44 Comparison of added mass and damping coefficients for porous heave plate. red line: Present work, $T = 2.5s$ and $s = 0.4r_d$. black line: [An and Faltinsen \(2013\)](#), $T = 2.0s$ and $s = 0.41r_d$.

while added mass is similar, the damping values are significantly larger for the fractal plate when compared with the evenly distributed porosity of [Tao and Dray \(2008\)](#) 20% porosity specimen. Results of [An and Faltinsen \(2013\)](#) for deep water case, which show a comparable result when compared between each other.

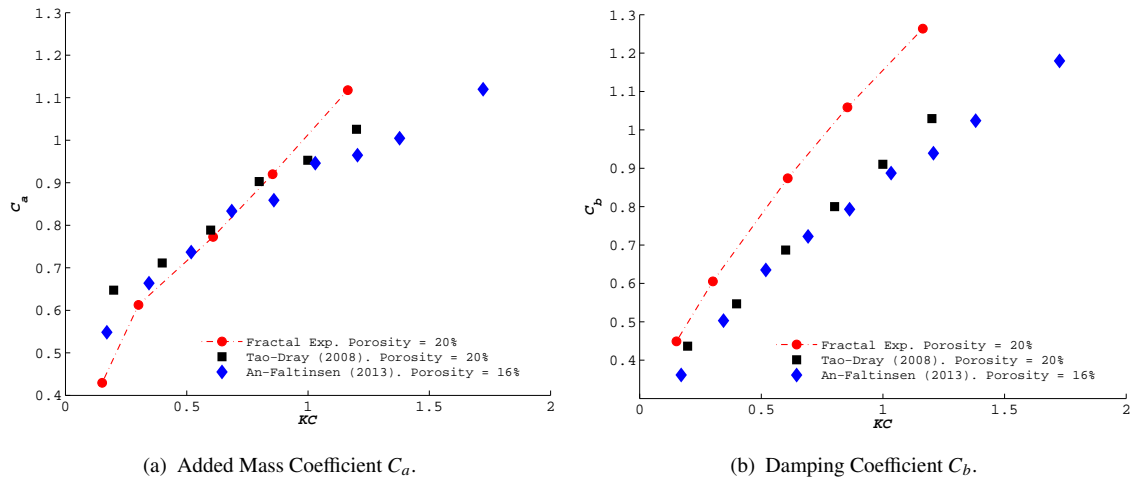


Fig. 6.45 Comparison of added mass and damping coefficients for porous heave plate. red line: Present work, $T = 2.5s$ and $s = 1.8r_d$. blue line: [An and Faltinsen \(2013\)](#), $T = 2.0s$ and $s = 2.85r_d$. black line: [Tao and Dray \(2008\)](#), $T = 2.0s$ and $s = 3.0r_d$.

Chapter 7

Conclusions

7.1 Conclusions

The main conclusions of the present work are summarize below:

1. Research on hydrodynamic forces on heave plates attached to oscillating bodies immersed in a fluid has been presented.
2. These heave plates are used as motion damping devices in semi-submersible floating platforms for offshore wind turbines.
3. The motion model considered is linear. This allows to describe the hydrodynamic forces independently for each frequency.
4. To compute that response forced heave (vertical axis) oscillations are applied at the body and the forces are measured and their first harmonic is computed.
5. Forces in phase with the motion are defined as the added mass and forces in counter-phase as the damping. The drag coefficient is defined on the basis of this damping.
6. The main parameter defining the flow is the Keulegan-Carpenter number KC . It is defined as the relation between the amplitude of heave motion and the diameter of the heave plate.
7. Solid and Porous heave plates as well heave plates with flaps have been modelled numerically.
8. Experiments have been conducted with a novel porous heave plate with a fractal pattern. Comparisons with data for porous plates by other authors are presented.

9. Numerical open source OpenFOAM code based on the Finite Volume Method (FVM) and Volume of Fluid (VOF) technique used to track the free surface (FS) motion was used to simulate the axisymmetric viscous flow problem.
10. For the heave plates oscillating closer to the free surface, the added mass and damping coefficients increase with the Keulegan-Carpenter number (KC) and with decreasing distance to free surface. The dependence of the hydrodynamic coefficients is strongly influenced for the free surface, and these coefficients of the solid heave plate were found to be in good agreement with the experiments.
11. The porosity of the heave plates reduces the added mass for the studied porosity at all KC numbers, but the porous heave plates are found to increase the damping coefficient with increasing amplitude of oscillation, achieving a maximum damping coefficient for the heave plate with 10% porosity in all KC range. When the KC number is small, the disk with 20% porosity yields approximately 16% increase in damping compared to the solid disk, but clearly under performs all the other disks when the KC increases, due to the large opening area ratio.
12. Numerical and experimental results for heave plates with flaps show that keeping the flap near to the end of the disc, increases the added mass when compared to the plain plate but significantly reduce damping too.
13. Simulations conducted on a circular solid disk oscillating at varying elevations from seabed suggest that as the structure moves closer to seabed the added mass and damping coefficients (C_a and C_b) increases continuously showing slight difference if the bottom is formed with a sandy bed as experiments published by [Wadhwa et al. \(2010\)](#). It can be caused by the cavity formed on the sandy bed when the disk moves close to the bottom. In the same way as for a heave plates oscillating near the free surface the coefficients increase with the Keulegan-Carpenter number (KC).
14. The vortex field generated by the oscillating disk appears to have more strength when the disk oscillates near the seabed, and this is reflected by the increase of the hydrodynamic coefficients for the same KC value. The vortex shedding patterns are altered by increasing KC and by proximity to the seabed.
15. Formulae in order to evaluate the hydrodynamic coefficients closer to free surface and near the seabed were derived, allowing the calculation of the added mass and damping with good agreement for distance ratios $h \leq 2.0 r_d$.

16. Numerical simulations also suggest that the coefficients present similar results for larger submergences or elevation of the disk, and the existence of a critical KC value, below which the variation of added mass and damping coefficient can be considered linear with KC . The slopes of the linear curve fits were found to increase monotonically with decreasing distance to free surface or the elevation from seabed.
17. An alternative way to obtain the damping coefficient looking at the dissipation mechanisms has been devised. In the present paper, its analysis has been restricted to the enstrophy contribution to dissipation.
18. The relationship between the damping coefficient obtained from the dissipation terms ($\dot{\mathcal{E}}_\omega$ and $\dot{\mathcal{E}}_{FS}$) and the classical damping coefficient has been discussed. From the present analysis, it seems that the enstrophy and free surface (disc oscillating close to a free surface) contribution to dissipation may be the lead actor in this type of flows.

7.2 Future work

Some topics requiring further research follow:

1. Research is ongoing on examining the vortex core strength, diameter, and pairing mechanisms including shedding angles. This should hopefully shed light on the underlying causes for the change in force coefficients.
2. Another research question is addressing the impact of these flow features on the added mass forces, which normally are considered to be un-influenced by viscosity or vorticity. Examination of streamlines and iso-baric lines should shed some light on this aspect.
3. The extension to three dimensional flows within the general framework of the solution method would be an important advance of this problem. This enables tackling more complex problems ensuring solution to other significant aspects like the three-dimensional vortex effects.
4. Look in more detail at the need of the turbulence modeling.
5. Detailed analysis of Fractal Plate results.
6. Investigate the high frequency components of the enstrophy integrals.
7. Evaluate the contribution of $\dot{\mathcal{E}}_{FS}$ for discs oscillating close to a free surface.

8. Investigate hydrodynamic coefficients for KC numbers above critical KC .
9. It has been found that the ratios between the numerical results and the theoretical values do not tend to one for low KC values, something for which an explanation is missing, thus deserving further research work.

Chapter 8

Thesis Publications

8.1 Refereed papers

- C. Garrido-Mendoza, K.P. Thiagarajan, A. Souto-Iglesias, B. Bouscasse and A. Colagrossi. Computation of flow features and hydrodynamic coefficients around heave plates oscillating near a seabed. *Submitted for publication*.
- Jesús Gómez-Goñi, Carlos A. Garrido-Mendoza, José Luis Cercós, and Leo González. Two phase analysis of sloshing in a rectangular container with Volume of Fluid (VOF) methods. *Ocean Engineering*, Vol. 73, 208 - 212, 2013.

8.2 Conference papers

- L. Gonzalez, A. Rodriguez, C. Garrido-Mendoza, J. Suarez, and F. Huera-Huarte. CFD simulations on the vortex-induced vibrations of a flexible cylinder with wake interference. In ASME, editor, *34th International Conference on Ocean, Offshore and Arctic Engineering (OMAE)*. OMAE2015-41128, 2015.
- C. López-Pavón, C. Garrido-Mendoza, and A. Souto-Iglesias. Hydrodynamic forces and pressure loads on heave plates for semi-submersible floating offshore wind turbines: a case study. In ASME, editor, *33rd International Conference on Ocean, Offshore and Arctic Engineering (OMAE)*. OMAE2014-24163, 2014.
- C. Garrido-Mendoza, K.P. Thiagarajan, A. Souto-Iglesias, B. Bouscasse and A. Colagrossi. Numerical investigation of the flow features around heave plates oscillating close to a free surface or seabed. In ASME, editor, *33rd International Conference on Ocean, Offshore and Arctic Engineering (OMAE)*. OMAE2014-23818, 2014.

- C. Garrido-Mendoza, A. Souto-Iglesias, and K. Thiagarajan. Numerical simulation of hydrodynamics of a circular disk oscillating near a seabed. In ASME, editor, *32nd International Conference on Ocean, Offshore and Arctic Engineering (OMAE)*. OMAE2013-11072, 2013.

References

- An, S. and Faltinsen, O. M. (2013). An experimental and numerical study of heave added mass and damping of horizontally submerged and perforated rectangular plates. *Journal of Fluids and Structures*, 39(0):87 – 101.
- Aubault, A., Cermelli, C., and Roddier, D. (2007). Parametric optimization of a semi-submersible platform with heave plates. In *ASME 2007 26th International Conference on Offshore Mechanics and Arctic Engineering*, pages 471–478. American Society of Mechanical Engineers.
- Bandt, C. and Hung, N. V. (2008). Fractal n-gons and their Mandelbrot sets. *Nonlinearity*, 21(11):2653–2670.
- Batchelor, G. K. (1967). *Introduction to Fluid Dynamics*. Cambridge University Press, New York.
- Bearman, P. W., Downie, M. J., Graham, J. M. R., and Obasaju, E. D. (1985). Forces on cylinders in viscous oscillatory flow at low keulegan-carpenter numbers. *Journal of Fluid Mechanics*, 154:337–356.
- Bernardinis de, B., Graham, J. M. R., and Parker, K. H. (1981). Oscillatory flow around disks and through orifices. *Journal of Fluid Mechanics*, 102:279–299.
- Brennen, C. (1982). A review of added mass and fluid inertial forces.
- Bulian, G., Botia-Vera, E., and Souto-Iglesias, A. (2014). Experimental sloshing pressure impacts in ensemble domain: Transient and stationary statistical characteristics. *Physics of Fluids (1994-present)*, 26(3):–.
- Cardesa, J., Nickels, T., and Dawson, J. (2012). 2d piv measurements in the near field of grid turbulence using stitched fields from multiple cameras. *Experiments in fluids*, 52(6):1611–1627.

-
- Cardesa-Dueñas, J., Nickels, T., and Dawson, J. (2011). Experimental study of homogenisation in grid turbulence. In *Journal of Physics: Conference Series*, volume 318, page 032041. IOP Publishing.
- Cermelli, C., Morrison, D., Martin, H. C. S., and Guinn, M. (2003). Progression of ultra-deep subsea deployment systems. *OTC15147 - Offshore Technology Conference Houston, Texas, U.S.A.*, (OTC15147).
- Chung, J. A. F. (1977). Forces on submerged cylinders oscillating near a free surface. *Journal of Hydronautics*, 11(3):100–106.
- Colagrossi, A., Souto-Iglesias, A., Antuono, M., and Marrone, S. (2013). Smoothed-particle-hydrodynamics modeling of dissipation mechanisms in gravity waves. *Phys. Rev. E*, 87:023302.
- Dennis, K. and Schlicker, S. (1995). Sierpinski N-Gons. *Pi Mu Epsilon Journal*, 10(2):81–89.
- DNV-RP-H103 (April 2010). Modelling and analysis of marine operations. Hovik, Norway.
- EWEA (2015). The European offshore wind industry - key trends and statistics 2014. Report, EWEA.
- Faltinsen, O. M. (1990). *Sea loads on ships and offshore structures / O.M. Faltinsen*. Cambridge University Press.
- Ferziger, J. H. and Peric, M. (1999). *Computational Methods for Fluid Dynamics*. Springer, 2nd edition.
- Garrido-Mendoza, C., Souto-Iglesias, A., and Thiagarajan, K. (2013). Numerical simulation of hydrodynamics of a circular disk oscillating near a seabed. In ASME, editor, *32nd International Conference on Ocean, Offshore and Arctic Engineering (OMAE)*. OMAE2013-11072.
- Garrido-Mendoza, C. A., Thiagarajan, K., Bouscasse, B., Colagrossi, A., and Souto-Iglesias, A. (2014). Numerical Investigation of the Flow Features around Heave Plates Oscillating Close to a Free Surface or Seabed. In ASME, editor, *33rd International Conference on Ocean, Offshore and Arctic Engineering (OMAE)*.
- Global Wind Energy Council (2013). Global Wind Report: Annual Market Update 2013. Report, Global Wind Energy Council. http://www.gwec.net/wp-content/uploads/2014/04/GWEC-Global-Wind-Report_9-April-2014.pdf.

- Gomez-Goni, J., Garrido-Mendoza, C. A., Cercos-Pita, J., and Gonzalez, L. (2013). Two phase analysis of sloshing in a rectangular container with volume of fluid (vof) methods. *Ocean Engineering*, 73(0):208 – 212.
- Graham, J. (1980). The forces on sharp-edged cylinders in oscillatory flow at low Keulegan-Carpenter numbers. *Journal of Fluid Mechanics*, 97:331–346.
- Greenhow, M. and Lin, W.-M. (1983). Nonlinear-free surface effects: Experiments and theory. Technical report, DTIC Document.
- Greenhow, M. and Yanbao, L. (1987). Added masses for circular cylinders near or penetrating fluid boundaries—review, extension and application to water-entry,-exit and slamming. *Ocean engineering*, 14(4):325–348.
- Hanson, T., Skaare, B., Yttervik, R., Nielsen, F., and Havmoller, O. (2011). Comparison of measured and simulated responses at the first full scale floating wind turbine hywind. Technical report, EWEA OFFSHORE.
- Haslum, H. A. and Faltinsen, O. M. (1999). Alternative shape of spar platforms for use in hostile areas. *Offshore Technology Conference*.
- He, H., Troesch, A., and Perlin, M. (2008). Hydrodynamics of damping plates at small kc numbers. In Kreuzer, E., editor, *IUTAM Symposium on Fluid-Structure Interaction in Ocean Engineering*, volume 8 of *Iutam Bookseries*, pages 93–104. Springer Netherlands.
- Herbert, G. J., Iniyan, S., Sreevalsan, E., and Rajapandian, S. (2007). A review of wind energy technologies. *Renewable and Sustainable Energy Reviews*, 11(6):1117 – 1145.
- Heronemus, W. E. (1972). Power from offshore winds. *8th Annual Conference and Exposition on Applications of Marine Technology*.
- Hirt, C. W. and Nichols, B. D. (1981). Volume of fluid (VOF) method for the dynamics of free boundaries. *Journal of Computational Physics*, 39(1):201 – 225.
- Huse, E. and Utnes, T. (1994). Springing Damping Of Tension Leg Platforms. In *26th Annual Proceedings of Offshore Technology Conference*, number 7446, pages 259–267. The Offshore Technology Conference.
- Hvroje, J. (1996). *Error Analysis and Estimation for the nite Volume Method with Application to Fluid Flows*. Ph.d. thesis, Imperial College, University of London.

-
- IDAE (2011). Plan de energías renovables (PER) 2011 – 2020. Special report. http://www.idae.es/uploads/documentos/documentos_11227_PER_2011-2020_def_93c624ab.pdf.
- Intergovernmental Panel on Climate Change (2012). Renewable Energy Sources and Climate Change Mitigation. Special report. http://www.ipcc.ch/pdf/special-reports/srren/SRREN_Full_Report.pdf.
- IREC (2014). Annual Report 2013. Annual report. http://content.irec.cat/annual_report_2013/files/assets/common/downloads/publication.pdf.
- Jones, A. and Westwood, A. (2005). Recent progress in offshore renewable energy technology development. *Power engineering society general meeting*, 2:2017–2022.
- Keulegan, G. H. and Carpenter, L. H. (1958). Forces on cylinders and plates in an oscillating fluid. *Journal of Research of the National Bureau of Standards*, 60(5):423–440.
- Korobkin, A. (2009). Added Masses of Three-Dimensional Bodies in Infinite Fluid. In *Added Masses of Ship Structures*, volume 88 of *Fluid Mechanics and Its Applications*, pages 81–102. Springer Netherlands.
- Lake, M., He, H., Troesch, A. W., Perlin, M., and Thiagarajan, K. P. (2000). Hydrodynamic Coefficient Estimation for TLP and Spar Structures. *Journal of Offshore Mechanics and Arctic Engineering*, 122(2):118–124.
- Lamb, H. (1945). *Hydrodynamics*. Dover Books on Physics. Dover publications.
- Larsson, L. and Baba, E. (1996). Ship resistance and flow computations. *Advances in marine Hydrodynamics*, pages 1–75.
- LeVeque, R. J. (2002). *Finite volume methods for hyperbolic problems*, volume 31. Cambridge university press.
- Li, J., Liu, S., Zhao, M., and Teng, B. (2013). Experimental investigation of the hydrodynamic characteristics of heave plates using forced oscillation. *Ocean Engineering*, 66(0):82 – 91.
- LLC., M. I. C. (2012). Floating offshore wind foundations: Industry consortia and projects in the united states, europe and japan. Technical report, Maine International Consulting LLC.

- Lopez-Pavon, C. and Souto-Iglesias, A. (2015). Hydrodynamic Coefficients and Pressure loads on Heave Plates for Semi-Submersible Floating Offshore Wind Turbines: a Comparative Analysis Using Large Scale Models. *Renewable Energy (in press)*.
- Lopez-Pavon, C., Watai, R. A., Ruggeri, F., Simos, A. N., and Souto-Iglesias, A. (2013). Influence of wave induced second-order forces in semi-submersible FOWT mooring design. In *ASME 32nd International Conference on Ocean, Offshore and Arctic Engineering, OMAE2013*.
- Marsh, G. (2014). Greater role for composites in wind energy. *Reinforced Plastics*, 58(1):20 – 24.
- Molin, B. (2001). On the Added Mass and Damping of Periodic Arrays of Fully or Partially Porous Disks. *Journal of Fluids and Structures*, 15(2):275 – 290.
- Molin, B. (2011). Hydrodynamic modeling of perforated structures. *Applied Ocean Research*, 33(1):1 – 11.
- Molin, B., Guérin, P., Martigny, D., and Weber, P. (1999). Etude théorique et expérimentale des efforts hydrodynamiques sur une embase plane à l’approche du fond marin. *Actes 7èmes Journées de l’Hydrodynamique*, pages 291–304.
- Molin, B. and Korobkin, A. (2001). Water entry of a perforated wedge. In *Proceedings of the 16th International Workshop on Water Waves and Floating Bodies*.
- Molin, B. and Nielsen, F. (2004). Heave added mass and damping of a perforated disk below the free surface. In *Proceedings of the 19th International Workshop on Water Waves and Floating Bodies*.
- Molin, B., Remy, F., and Ripol, T. (2008). Experimental study of the heave added mass and damping of solid and perforated disks close to the free surface. In *International Congress of International Maritime Association of the Mediterranean*, Varna, Bulgarie.
- Morrison, D. and Cermelli, C. (2003). Deployment of subsea equipment in ultradeep water. *ASME Conference Proceedings*, 2003(36819):341–349.
- Musial, W., Butterfield, S., and Boone, A. (2004). Feasibility of floating platform systems for wind turbines. In *23rd ASME Wind Energy Symposium, Reno, NV*.
- Nallayarasu, S. and Bairathi, K. (2014). Hydrodynamic response of spar hulls with heave damping plate using simplified approach. *Ships and Offshore Structures*.

-
- Nedić, J., Ganapathisubramani, B., and Vassilicos, J. (2013). Drag and near wake characteristics of flat plates normal to the flow with fractal edge geometries. *Fluid Dynamics Research*, 45(6):061406.
- Nicholls-Lee, R., Micklethwaite, W., Walker, R., and Argall, R. (2014). Novel, Practical and Effective: a Feasibility Study for a Low Motion, Floating Wind Turbine Platform. In Asme, editor, *33rd International Conference on Ocean, Offshore and Arctic Engineering (OMAE)*.
- Nielsen, F., Hanson, T., and Skaare, B. (2006). Integrated dynamic analysis of floating offshore wind turbines. In *Proceedings of the 25th International Conference on Offshore Mechanics and Arctic Engineering (OMAE)*. ASME.
- OpenCFD, L. (2013). *OpenFOAM - User Guide*. <http://foam.sourceforge.net/docs/Guides-a4/UserGuide.pdf>, version 2.2.1 edition.
- OpenCFD Ltd. (2013). *OpenFOAM - Programmer's Guide*. <http://foam.sourceforge.net/docs/Guides-a4/ProgrammersGuide.pdf>, version 2.2.1 edition.
- PANER (2010). Plan de acción nacional de energías renovables de españa 2011 – 2020. Special report. http://www.minetur.gob.es/energia/desarrollo/EnergiaRenovable/Documents/20100630_PANER_Espanaversion_final.pdf.
- Philip, N. T., Nallayarasu, S., and Bhattacharyya, S. (2012). Damping characteristics of heave plates attached to spar hull. In *ASME 2012 31st International Conference on Ocean, Offshore and Arctic Engineering*, pages 249–260. American Society of Mechanical Engineers.
- Pistani, F. and Thiagarajan, K. (2006). Assessment of dynamic factors for subsea deployment from crane vessels. *Technical Report No. R2D3-UWA-05-561*.
- Prislin, I., Blevins, R., and Halkyard, J. (1998). Viscous damping and added-mass of solid square plates. In *Proceedings of the 17th International Conference on Offshore Mechanics and Arctic Engineering (OMAE)*. ASME.
- Real decreto ley 1/2012 (2012). Boletín Oficial del Estado BOE. Special report. <http://www.boe.es/boe/dias/2012/01/28/pdfs/BOE-A-2012-1310.pdf>.
- REE (2014). The Spanish Electricity System. Preliminary report. http://www.ree.es/sites/default/files/downloadable/preliminary_report_2014.pdf.

- Roddier, D., Cermelli, C., Aubault, A., and Weinstein, A. (2010). Windfloat: A floating foundation for offshore wind turbines. *Journal of Renewable and Sustainable Energy*, 2(3):–.
- Roddier, D., Cermelli, C., and Weinstein, A. (2009). Windfloat: A floating foundation for offshore wind turbines—part i: Design basis and qualification process. In *Proceedings of the 28th International Conference on Ocean, Offshore and Arctic Engineering (OMAE)*, volume Volume 4: Ocean Engineering; Ocean Renewable Energy; Ocean Space Utilization, Parts A and B, pages 845–853. ASME: OMAE2009-79229.
- Roveri, F., Oliveira, M. D., and Moretti, M. (1996). Installation of a production manifold in 2000 ft water depth offshore brazil. *OTC8237 - Offshore Technology Conference Houston, Texas, U.S.A.*, (OTC8237).
- Salim, S. M. and Cheah, S. C. (2009). Wall y + Strategy for Dealing with Wall-bounded Turbulent Flows. In *Proceedings of the International MultiConference of Engineers and Computer Scientists*, volume Vol. II. IMECS.
- Sarpkaya, T. and Isaacson, M. (1981). *Mechanics of wave forces on offshore structures*. New York: van Nostrand Reinhold.
- Sudhakar, S. and Nallayarasu, S. (2011). Influence of heave plate on hydrodynamic response of SPAR. In *ASME 30th International Conference on Ocean, Offshore and Arctic Engineering, OMAE2011*.
- Sumer, B. and Fredsøe, J. (1997). *Hydrodynamics around cylindrical structures*. World Scientific Publ.
- Tao, L. and Cai, S. (2004). Heave motion suppression of a spar with a heave plate. *Ocean Engineering*, 31(5–6):669 – 692.
- Tao, L., Cheng, L., and Thiagarajan, K. (1999). Numerical estimation of hydrodynamic heave damping of a vertical cylinder with appendages. In *Proceedings of the Ninth International Offshore and Polar Engineering Conference*, volume Vol III, 490-495.
- Tao, L. and Dray, D. (2008). Hydrodynamic performance of solid and porous heave plates. *Ocean Engineering*, 35(10):1006 – 1014.
- Tao, L., Molin, B., Scola, Y.-M., and Thiagarajan, K. (2007). Spacing effects on hydrodynamics of heave plates on offshore structures. *Journal of Fluids and Structures*, 23(8):1119 – 1136.

-
- Tao, L. and Thiagarajan, K. (2000). The influence of edge sharpness on the heave damping forces experienced by a tlp column. In *Tenth International Offshore and Polar Engineering conference*, volume Volume 1, pages 277–282. ISOPE.
- Tao, L. and Thiagarajan, K. (2003a). Low KC flow regimes of oscillating sharp edges I. Vortex shedding observation. *Applied Ocean Research*, 25(1):21 – 35.
- Tao, L. and Thiagarajan, K. (2003b). Low KC flow regimes of oscillating sharp edges. II. Hydrodynamic forces. *Applied Ocean Research*, 25(2):53 – 62.
- Tao, L., Thiagarajan, K., and Cheng, L. (2000). On the parametric dependence of springing damping of tlp and spar columns. *Applied Ocean Research*, 22(5):281 – 294.
- Thiagarajan, K. (1993). *Hydrodynamics of oscillating cylinder and disks at low Keulegan-Carpenter numbers*. Ph.d. thesis, Department of Naval Architecture and Marine Engineering, The University of Michigan.
- Thiagarajan, K. P. and Troesch, A. W. (1998). Effects of appendages and small currents on the hydrodynamic heave damping of tlp columns. *Journal of Offshore Mechanics and Arctic Engineering*, 120(1):37–42.
- Thurston, K. W., Swanson, R. C., and Kopp, F. (2011). Statistical characterization of slack-ing and snap loading during offshore lifting and lowering in a wave environment. *ASME Conference Proceedings*, 2011(44335):269–277.
- Ubbink, O. (1997). *Numerical Prediction of Two Fluid Systems with Sharp Interfaces*. Ph.d. thesis, Imperial College, University of London.
- Utnes, T., Eidsvik, K. J., and Moe, G. (1995). Dynamic separation over bluff bodies predictions based upon reynolds equations. *Journal of Hydraulic Research*, 33(2):219–242.
- Versteeg, H. and Malalasekera, W. (1995). *An introduction to Computational FluidDynamics, the Finite Volume Method*. Harlow: Longman Scientific and Technical.
- Vinje, T. (2001). Fluid flow through perforated structures. Technical report, MarinConsult Report.
- Viselli, A. M., Goupee, A. J., and Dagher, H. J. (2014). Model Test of a 1:8 Scale Floating Wind Turbine Offshore in the Gulf of Maine. In Asme, editor, *33rd International Conference on Ocean, Offshore and Arctic Engineering (OMAE)*.

- Vu, K. H., Chenu, B., and Thiagarajan, K. P. (2008). Hydrodynamic damping due to porous plates. In *Proc. World Scientific and Engineering Academy and Society, Greece*.
- Wadhwa, H., Krishnamoorthy, B., and Thiagarajan, K. P. (2010). Variation of Heave Added Mass and Damping Near Seabed. In *ASME 29th International Conference on Offshore Mechanics and Arctic Engineering, OMAE*.
- Wadhwa, H. and Thiagarajan, K. P. (2009). Experimental Assessment of Hydrodynamic Coefficients of Disks Oscillating Near a Free Surface. In *ASME 28th International Conference on Offshore Mechanics and Arctic Engineering, OMAE*.

Appendices

Appendix A

Energy Eqn. with control Volume.

Considering a generic control volume $V_c(t)$, the transport theorem for a generic fluid quantity f reads:

$$\frac{D}{Dt} \int_{V_c(t)} (\rho f) dV = \int_{V_c(t)} \rho \frac{Df}{Dt} dV + \int_{\partial V_c(t)} (\mathbf{v}^b - \mathbf{u}) \cdot \mathbf{n} (\rho f) dS \quad (\text{A.1})$$

Substituting $f = (\mathbf{u}^2/2 - G)$ in Eqn. (A.1) yields:

$$\frac{D}{Dt} \int_{V_c(t)} (\mathbf{u}^2/2 - G) \rho dV = \int_{V_c(t)} \rho \frac{D(\mathbf{u}^2/2 - G)}{Dt} dV + \int_{\partial V_c(t)} \rho (\mathbf{u}^2/2 - G) (\mathbf{v}^b - \mathbf{u}) \cdot \mathbf{n} dS \quad (\text{A.2})$$

Using Eqn. (4.9) it can be rewritten as:

$$\dot{\mathcal{E}}_M = \int_{\partial V_c(t)} \mathbb{T} \mathbf{u} \cdot \mathbf{n} dS - \int_{V_c(t)} \mathbb{T} : \mathbb{D} dV + \int_{\partial V_c(t)} \rho (\mathbf{u}^2/2 + gz) (\mathbf{v}^b - \mathbf{u}) \cdot \mathbf{n} dS \quad (\text{A.3})$$

The surface of the control volume ∂V_c can be divided as $\partial V_c = \partial \Omega_F \cup \partial \Omega_B \cup \partial \Omega_C \cup \partial \Omega_G$ where $\partial \Omega_F$ is the free surface, $\partial \Omega_B$ the surface of the moving solid body, $\partial \Omega_G$ the seabed and $\partial \Omega_C$ a control surface which closes the domain (Fig. 4.2). Therefore, the first right hand

side term from Eqn. (A.3) can be decoupled as:

$$\begin{aligned}
 \int_{\partial V_c(t)} \mathbb{T} \mathbf{u} \cdot \mathbf{n} dS &= \int_{\partial \Omega_F(t)} (\mathbb{T} \mathbf{n}) \cdot \mathbf{u} dS + \int_{\partial \Omega_G(t)} (\mathbb{T} \mathbf{n}) \cdot \mathbf{u} dS + \\
 &\quad \int_{\partial \Omega_B(t)} (\mathbb{T} \mathbf{n}) \cdot \mathbf{u} dS + \int_{\partial \Omega_C(t)} (\mathbb{T} \mathbf{n}) \cdot \mathbf{u} dS + \\
 &= P_{body/fluid} + \int_{\partial \Omega_C(t)} (\mathbb{T} \mathbf{n}) \cdot \mathbf{u} dS .
 \end{aligned} \tag{A.4}$$

The first two surface integrals are null since the stress is zero on $\partial \Omega_F$ and velocity is zero in the seabed. The last term of Eqn. (A.3) becomes:

$$\begin{aligned}
 \int_{\partial \Omega_{V_c(t)}} \rho (\mathbf{u}^2/2 + gz) (\mathbf{v}^b - \mathbf{u}) \cdot \mathbf{n} dS &= \int_{\partial \Omega_B(t)} \rho (\mathbf{u}^2/2 + gz) (\mathbf{v}^B - \mathbf{u}) \cdot \mathbf{n} dS + \\
 &\quad \int_{\partial \Omega_G(t)} \rho (\mathbf{u}^2/2 + gz) (\mathbf{v}^G - \mathbf{u}) \cdot \mathbf{n} dS + \\
 &\quad \int_{\partial \Omega_F(t)} \rho (\mathbf{u}^2/2 + gz) (\mathbf{v}^F - \mathbf{u}) \cdot \mathbf{n} dS + \\
 &\quad \int_{\partial \Omega_C(t)} \rho (\mathbf{u}^2/2 + gz) (\mathbf{v}^C - \mathbf{u}) \cdot \mathbf{n} dS ,
 \end{aligned} \tag{A.5}$$

where the three first integrals of the right-hand side are null since $\mathbf{v} = \mathbf{u}$, and eqn. (A.3) thus becomes:

$$\dot{\mathcal{E}}_M = P_{body/fluid} + \int_{V_c(t)} \mathbb{T} : \mathbb{D} dV + \int_{\partial \Omega_C(t)} [\rho (\mathbf{v}^C - \mathbf{u}) (\mathbf{u}^2/2 + gz) + \mathbb{T} \mathbf{u}] \cdot \mathbf{n} dS . \tag{A.6}$$

The second term on the right hand side is the fluid dissipated power $\dot{\mathcal{E}}_D$, which can be decomposed as in section B using Eqn. (B.1):

$$\dot{\mathcal{E}}_D = \dot{\mathcal{E}}_{wall} + \dot{\mathcal{E}}_{FS} + \dot{\mathcal{E}}_{\omega} - 2\mu \int_{\partial \Omega_C(t)} (\nabla \mathbf{u} \mathbf{u}) \cdot \mathbf{n} dS . \tag{A.7}$$

Using the constitutive equation (4.3), Eqn. (A.6) can be reshaped as:

$$\begin{aligned} \dot{\mathcal{E}}_M = & P_{body/fluid}^{Pressure} + P_{body/fluid}^{Viscous} + P_{Control}^{Pressure} + P_{Control}^{Viscous} + \\ & \int_{\partial\Omega_C(t)} \rho(\mathbf{u}^2/2 + gz)(\mathbf{v}^C - \mathbf{u}) \cdot \mathbf{n} dS + \\ & \dot{\mathcal{E}}_\omega + \dot{\mathcal{E}}_{FS}, \end{aligned} \quad (\text{A.8})$$

where the power terms $P_{control}$ are defined as:

$$P_{Control}^{Pressure} := - \int_{\partial\Omega_C(t)} p \mathbf{n} \cdot \mathbf{u} dS, \quad P_{Control}^{Viscous} := -\mu \int_{\partial\Omega_C(t)} (\boldsymbol{\omega} \times \mathbf{n}) \cdot \mathbf{u} dS \quad (\text{A.9})$$

Appendix B

Decomposition of the dissipation term.

Adding and subtracting enstrophy, Eqn. (4.15) can be written as:

$$\dot{\mathcal{E}}_D = -2\mu \int_{\Omega} \mathbb{D} : \mathbb{D} dV = -2\mu \int_{\partial\Omega} (\nabla \mathbf{u} \mathbf{u}) \cdot \mathbf{n} dS - \mu \int_{\Omega} \omega^2 dV. \quad (\text{B.1})$$

Defining

$$\begin{aligned} \dot{\mathcal{E}}_{\omega} &:= -\mu \int_{\Omega} \omega^2 dV, \\ \dot{\mathcal{E}}_{FS} &:= -2\mu \int_{\partial\Omega_F} (\nabla \mathbf{u} \mathbf{u}) \cdot \mathbf{n} dS, \\ \dot{\mathcal{E}}_{wall} &:= -2\mu \int_{\partial\Omega_B} (\nabla \mathbf{u} \mathbf{u}_B) \cdot \mathbf{n} dS, \end{aligned} \quad (\text{B.2})$$

the viscous dissipation power can be decomposed as:

$$\dot{\mathcal{E}}_D := \dot{\mathcal{E}}_{wall} + \dot{\mathcal{E}}_{FS} + \dot{\mathcal{E}}_{\omega}. \quad (\text{B.3})$$

Rearranging Eqn. (B.3) and Eqn. (4.16) we get:

$$\dot{\mathcal{E}}_M = (P_{ext} + \dot{\mathcal{E}}_{wall}) + \dot{\mathcal{E}}_{FS} + \dot{\mathcal{E}}_{\omega}. \quad (\text{B.4})$$

The sum $(P_{ext} + \dot{\mathcal{E}}_{wall})$ can be rewritten as:

$$P_{ext} + \dot{\mathcal{E}}_{wall} = \int_{\partial\Omega_B} \mathbb{T} \mathbf{n} \cdot \mathbf{u}_B dS - 2\mu \int_{\partial\Omega_B} (\nabla \mathbf{u} \mathbf{u}_B) \cdot \mathbf{n} dS, \quad (\text{B.5})$$

and using the constitutive Eqn. (4.3) we get:

$$P_{ext} + \dot{\mathcal{E}}_{wall} = \int_{\partial\Omega_B} -p \mathbf{u}_B \cdot \mathbf{n} dS - \mu \int_{\partial\Omega_B} (\omega \times \mathbf{u}_B) \cdot \mathbf{n} dS. \quad (\text{B.6})$$

Defining

$$P_{body/fluid}^{Pressure} := - \int_{\partial\Omega_B} p \mathbf{u}_B \cdot \mathbf{n} dS, \quad P_{body/fluid}^{Viscous} := -\mu \int_{\partial\Omega_B} (\boldsymbol{\omega} \times \mathbf{n}) \cdot \mathbf{u}_B dS \quad (\text{B.7})$$

the Eqn. (B.4) can be finally expressed as:

$$\dot{\mathcal{E}}_M = P_{body/fluid}^{Pressure} + P_{body/fluid}^{Viscous} + \dot{\mathcal{E}}_{FS} + \dot{\mathcal{E}}_{\omega}. \quad (\text{B.8})$$

B.1 Enstrophy volume integral in OpenFOAM

```

/*-----*\
License
  This file is based on the OpenFOAM provided one enstrophy.C
  Copyright (C) 2015 Carlos Ariel Garrido-Mendoza <carlos_garridomendoza@yahoo.es>

  This file is free software: you can redistribute it and/or modify it
  under the terms of the GNU General Public License as published by
  the Free Software Foundation, either version 3 of the License, or
  (at your option) any later version.

  This file is distributed in the hope that it will be useful, but WITHOUT
  ANY WARRANTY; without even the implied warranty of MERCHANTABILITY or
  FITNESS FOR A PARTICULAR PURPOSE. See the GNU General Public License
  for more details.

  You should have received a copy of the GNU General Public License
  along with this file. If not, see <http://www.gnu.org/licenses/>.

Application
  Enstrophy Integral

Description
  Calculates and writes the Enstrophy of the velocity field U.

  The -noWrite option just outputs the max/min values without writing the
  field.

\*-----*/

#include "calc.H"
#include "fvc.H"

// * * * * *

void Foam::calc(const argList& args, const Time& runTime, const fvMesh& mesh)
{
    bool writeResults = !args.optionFound("noWrite");

    IOobject Uheader
    (
        "U",
        runTime.timeName(),
        mesh,
        IOobject::MUST_READ
    );

    if (Uheader.headerOk())
    {
        Info<< "    Reading U" << endl;
        volVectorField U(Uheader, mesh);

        Info<< "    Calculating enstrophy" << endl;
        volScalarField Int_enstrophy
        (

```

```

        IOobject
        (
            "Int_enstrophy",
            runTime.timeName(),
            mesh,
            IOobject::NO_READ
        ),
        mesh,
        dimensionedScalar("0", dimless, 0),
        zeroGradientFvPatchScalarField::typeName
    );
    Int_enstrophy.dimensionedInternalField() = sum(magSqr(fvc::curl(U))*mesh.V());
    Int_enstrophy.correctBoundaryConditions();

    Info<< "enstrophy(U) Volume Integral : "
        << max(Int_enstrophy).value() << " "
        << min(Int_enstrophy).value() << endl;

    if (writeResults)
    {
        Int_enstrophy.write();
    }
    else
    {
        Info<< "      No U" << endl;
    }

    Info<< "\nEnd\n" << endl;
}

// *****

```

B.2 Free surface dissipation surface integral in OpenFOAM

```

/*-----*\
License
  This file is based in the OpenFOAM provided one enstrophy.C
  Copyright (C) 2015 Carlos Ariel Garrido-Mendoza <carlos_garridomendoza@yahoo.es>

  This file is free software: you can redistribute it and/or modify it
  under the terms of the GNU General Public License as published by
  the Free Software Foundation, either version 3 of the License, or
  (at your option) any later version.

  This file is distributed in the hope that it will be useful, but WITHOUT
  ANY WARRANTY; without even the implied warranty of MERCHANTABILITY or
  FITNESS FOR A PARTICULAR PURPOSE. See the GNU General Public License
  for more details.

  You should have received a copy of the GNU General Public License
  along with this file. If not, see <http://www.gnu.org/licenses/>.

Application
  Free Surface dissipation Integral

Description
  Calculates and writes the dissipation of the Free Surface.

  The -noWrite option just outputs the max/min values without writing the
  field.

\*-----*/

#include "calc.H"
#include "fvc.H"

// * * * * *

void Foam::calc(const argList& args, const Time& runTime, const fvMesh& mesh)
{
    bool writeResults = !args.optionFound("noWrite");

    IOobject Uheader
    (
        "U",
        runTime.timeName(),
        mesh,
        IOobject::MUST_READ
    );

    /*IOobject alpha
    (
        "alpha.water",
        runTime.timeName(),
        mesh,
        IOobject::MUST_READ
    );*/

```

```

volScalarField alpha
(
    IOobject
    (
        "alpha1",
        runTime.timeName(),
        mesh,
        IOobject::MUST_READ
    ),
    mesh
);

if (Uheader.headerOk())
{
    Info<< "      Reading U" << endl;
    volVectorField U(Uheader, mesh);
    //const labelList& cells = mesh_.cellZones()

    Info<< "      Calculating FS dissipation" << endl;
    volScalarField myalpha
    (
        IOobject
        (
            "myalpha",
            runTime.timeName(),
            mesh,
            IOobject::NO_READ
        ),
        mesh,
        dimensionedScalar("0", dimless, 0.0),
        zeroGradientFvPatchScalarField::typeName
    );
    volScalarField FS
    (
        IOobject
        (
            "Int_FS",
            runTime.timeName(),
            mesh,
            IOobject::NO_READ
        ),
        mesh,
        dimensionedScalar("0", dimensionSet(0, 1, -2, 0, 0, 0, 0), 0.0),
        zeroGradientFvPatchScalarField::typeName
    );

    forAll(alpha, cellI)
    {
        if (alpha[cellI] >= 0.1 && alpha[cellI] <= 0.9)
        {
            myalpha[cellI] = 1.0;
        }
    }
}

```


Appendix C. *Decomposition of the dissipation term.* **B.2 Free surface dissipation integral**

```
FS.dimensionedInternalField() = sum(myalpha * (fvc::grad(U) & U) & fvc::reconstruct(mesh
.magSf()));
FS.correctBoundaryConditions();

if (writeResults)
{
    FS.write();
}

Info<< "free surface dissipation Surface Integral : "
<< FS[0] << endl;
}
else
{
    Info<< "    No U" << endl;
}

Info<< "\nEnd\n" << endl;
}

// ***** //
```


Appendix C

Useful Relations.

$$(\boldsymbol{a} \times \boldsymbol{b}) \cdot \boldsymbol{c} = \boldsymbol{a} \cdot (\boldsymbol{b} \times \boldsymbol{c}) \quad (\text{C.1})$$

$$\mathbb{D} := \frac{1}{2}(\nabla \boldsymbol{u} + \nabla^T \boldsymbol{u}) \quad (\text{C.2})$$

$$\mathbb{W} := \frac{1}{2}(\nabla \boldsymbol{u} - \nabla^T \boldsymbol{u})$$

$$\nabla \boldsymbol{u} = \mathbb{D} + \mathbb{W} \quad (\text{C.3})$$

$$\mathbb{W} \boldsymbol{a} = \boldsymbol{\omega} \times \boldsymbol{a}$$

$$\boldsymbol{A} \boldsymbol{u} \cdot \boldsymbol{v} = \boldsymbol{u} \cdot \boldsymbol{A}^T \boldsymbol{v} \quad (\text{C.4})$$

Appendix D

Pressure-Velocity Coupling Algorithm.

PIMPLE algorithm combines the *SIMPLE* algorithm then uses pressure implicit with splitting the operators (*PISO*) algorithm to rectify the second pressure correction and correct both velocities and pressure explicitly (Ferziger and Peric, 1999; Versteeg and Malalasekera, 1995).

The pressure-velocity dependency is solved by Rhie-Chow interpolation in the following scheme:

1. Set the boundary conditions.
2. Solve the discretized momentum equation to compute an intermediate velocity field.
3. Calculate $H(U)$.
4. Compute the mass fluxes at the cells faces.
5. Solve the pressure equation.
6. Correct the mass fluxes at the cell faces.
7. Correct the velocities on the basis of the new pressure field.
8. Update the boundary conditions.
9. Repeat from 3 for the prescribed number of times.
10. Repeat from second step until convergence is achieved.
11. Increase the time step and repeat from first step.

This assumes the coefficients in $H(U)$ in terms of previous time steps. The correction for this creates the “PIMPLE” algorithm which is simply a repetition of the *PISO* until convergence is achieved. The issue by this approximation is not further pursued in this thesis but details are given in the PhD thesis of [Hvoroje \(1996\)](#).

The *PIMPLE* algorithm is implemented in OpenFOAM as follows:

- Define the equation for U .

```
fvVectorMatrixUEqn
(
    fvm::ddt(rho,U)
    + fvm::div(rhoPhi,U)
    + turbulence->divDevRhoRef(f(rho,U)
);
```

- Solve the momentum predictor.

```
solve
(
    UEqn == fvc::reconstruct
    (
        (
            fvc::interpolate(interface.sigmaK())*fvc::snGrad(alpha1)
            - ghf*fvc::snGrad(rho)
            - fvc::snGrad(p_rgh)
        )*mesh.magSf()
    )
);
```

- Calculate the a_p coefficient and calculate U .

```
volScalarFieldrAU("rAU",1.0/UEqn.A());
volVectorFieldHbyA("HbyA",U);
HbyA = rAU * UEqn.H();
```

- Calculate the flux.

```

surfaceScalarField phiHbyA
(
    "phiHbyA",
    (fvc :: interpolate(HbyA)&mesh.Sf())
    + fvc :: ddtPhiCorr(rAU, rho, U, phiAbs)

    adjustPhi(phiHbyA, U, p_rgh);

```

- Define and solve the pressure equation and repeat for the prescribed number of non-orthogonal corrector steps.

```

fvScalarMatrix p_rghEqn
(
    fvm :: laplacian(rAUf, p_rgh) == fvc :: div(phiHbyA)
);

p_rghEqn.setReference(pRefCell, getRefCellValue(p_rgh, pRefCell));
p_rghEqn.solve(mesh.solver(p_rgh.select(pimple.finalInnerIter())));

```

- Correct the flux.

```

if(pimple.finalNonOrthogonalIter())
    phi = phiHbyA - p_rghEqn.flux();

```

- Correct the velocities on the basis of the new pressure field.

```

U = HbyA + rAU * fvc :: reconstruct((phi - p_rghEqn.flux())/rAUf);
U.correctBoundaryConditions();
fvOptions.correct(U);

```

- Calculate continuity errors.

```

#include "continuityErrs.H"

```

- Repeat from the calculation of a_p for the prescribed number of *PIMPLE* corrector steps.

Appendix E

Volume of Fluid Method.

OpenFOAM uses the Volume of Fluid method (VOF) (Hirt and Nichols, 1981) to track the movement of the free surface (the air-water interface). This method determines the fraction of each fluid that exists in each cell of the computation mesh (known as the volume fraction). The equation for the volume fraction is:

$$\frac{\partial \alpha}{\partial t} + \nabla \cdot \alpha U = 0, \quad (\text{E.1})$$

where U is the velocity field composed of u , v and α is the volume fraction of water. α will vary between 0 and 1. If a cell is completely full of water, $\alpha = 1$, if it is full of air then $\alpha = 0$. The volume fraction (also known as the phase fraction) α is used to determine the density of the mixture inside each cell of the mesh, (the density that is used to solve the Navier-Stokes equations). The density of the mixture is determined by:

$$\rho = \alpha \rho_w + (1 - \alpha) \rho_a, \quad (\text{E.2})$$

where ρ_w is the density of water and ρ_a is the density of the air.

Appendix F

Fractal Plate Characteristics.

The Fractal Plate was mechanized on a circular plate of 500mm radius and 5mm thick. This design has a perforation ratio of 20%.



Fig. F.1 Fractal plate used in experiments.

The main characteristics of the Fractal Plate as described below:

- Circular holes. The Fractal Plate has 1744 holes constructed starting from an octoflake. This 8-flake is replaced by a flake of smaller n -gons, such that the scaled polygons are placed at the vertices, and sometimes in the center (see Figure F.2). This process is repeated recursively to result in the fractal.

The circular holes comprise a 18% of total porosity and have different diameter depending of the fractal iteration as shown in Table F.1. A general view of the holes distribution is shown in Figure F.3.

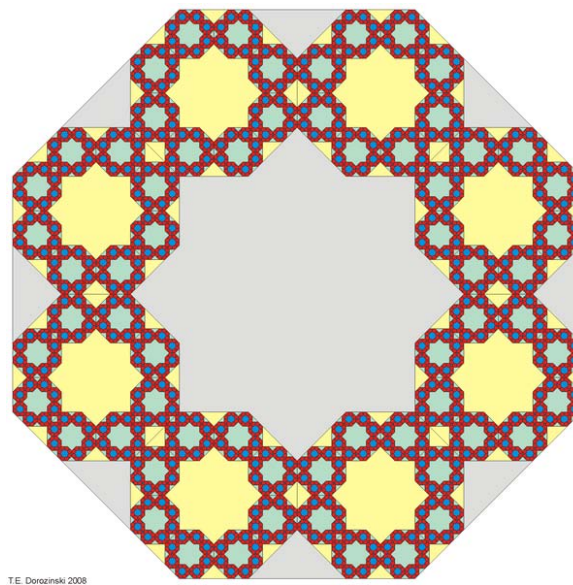


Fig. F.2 The third iteration of the octoflake or 8-flake.

Table F.1 Size of holes used in the Fractal Plate.

Circular holes	
Number of holes	Diameter [mm]
16	48
64	26
128	15
512	8
1024	4

- Plate edge. The edge is also based on a fractal geometry, starting from a dodecagon inscribed in a circle of 500 mm radius and corresponds to 2% of total porosity. On each side of the polygon the fractal pattern is repeated as shown in Figure F.4.

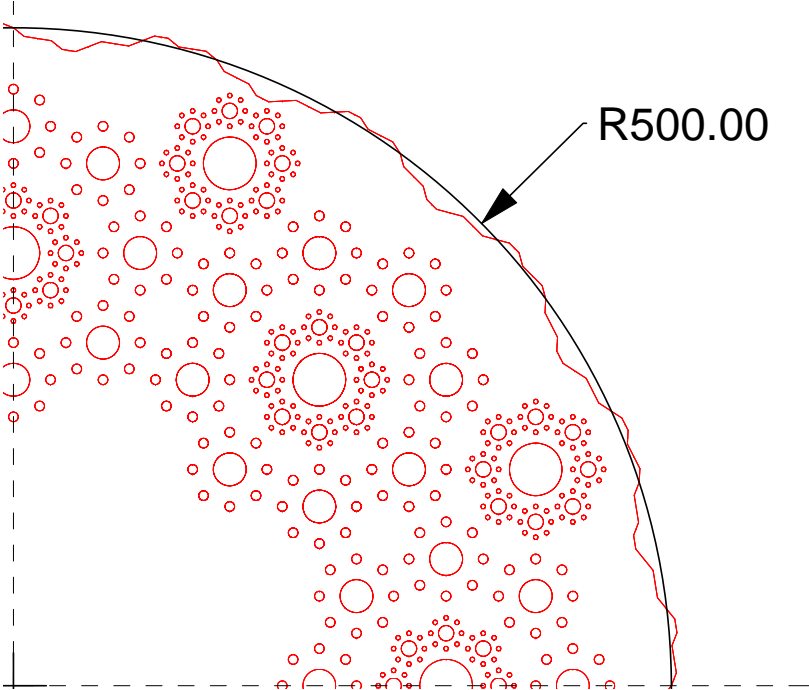


Fig. F.3 Holes distribution on the disk.

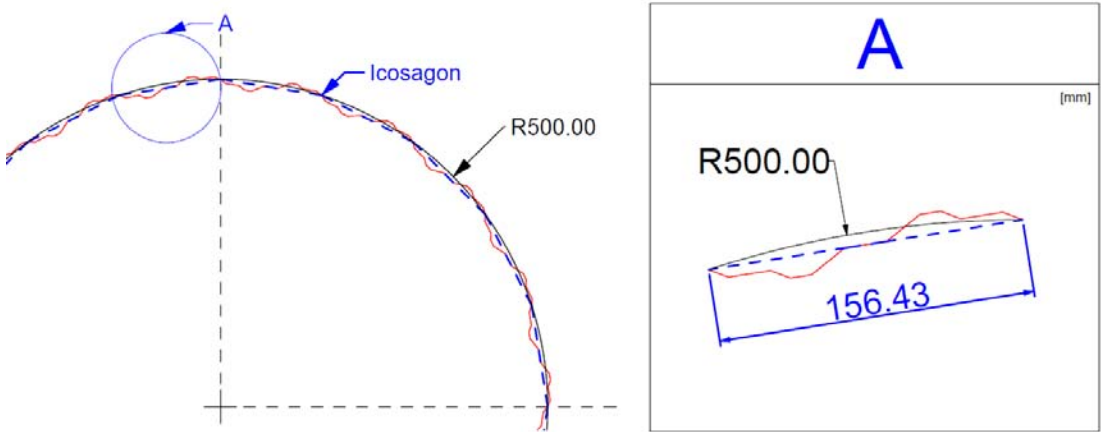


Fig. F.4 Illustration of the fractal perimeter.